Haptic Teleoperation Based Rehabilitation Systems for Task-Oriented Therapy

by

Ran TAO

A thesis submitted in partial fulfilment of the requirements for the degree of

MASTER OF SCIENCE

in

CONTROL SYSTEMS

DEPARTMENT OF ELECTRICAL AND COMPUTER ENGINEERING

UNIVERSITY OF ALBERTA

Abstract

This thesis focuses on the analysis and implementation of haptic teleoperation systems for home-based remote rehabilitation therapies. The main objective is to link the hand of a hospital-based therapist to the hand of a home-based disabled patient haptically, in order to simulate conventional in-hospital therapies.

A new telerehabilitation paradigm involving telerobotic systems is proposed. The proposed "Learn-and-replay" paradigm for task-oriented therapy consists of two phases: a therapist-in-loop phase where the therapist interacts with the patient through the haptic telerobotic interface to perform one or more repetitions of a cooperative therapy task, and a therapist-out-of-loop phase where the therapist's cooperative role in the task is played by the patient-side robot in future repetitions. Various technical aspects of this paradigm are explored in this thesis, including the therapist's arm impedance estimation and emulation through impedance control. One degree-of-freedom and a two degree-of-freedom advanced cooperative manipulation tasks are tested for proof of concept.

Traditionally, human arm passivity is assumed for teleoperation system stability analysis. Recent research has shown that such an assumption can be inaccurate or too conservative. Especially, human arm can demonstrate active behaviour during telerehabilitation scenarios. A series-shunt approach is proposed to take into account some a priori information about the activity or excessive passivity of the human operator in order to derive more exact stability criteria. Both theoretical derivation and experimental validation are carried out in this work.

Acknowledgements

First of all I would like to thank Dr. Tavakoli for your continuous support and patient guidance. You are both a teacher and a friend to me. Your work attitude and how you treat people have set examples for me for the rest of my life. Thank you for providing me with the opportunity to get both theoretical and practical training during my Master's program. It was also a pleasure to go to the Haptic Symposium conference in Houston with you.

Next I would like to thank all the colleagues in the Telerobotic and Biorobotic Systems Lab for both academic discussions and your friendship. Especially, I would like to thank the lab alumni Dr. Ali Jazayeri for the useful discussions in the passivity/activity work and Matthew Dyck for the help with learning how to use the rehabilitation robot. Thank you Farokh Atashzar and Mahya Shahbazi for the helpful discussions with regard to the learn-and-replay work.

I would also like to thank my parents for their unconditional love and support for whatever goals I pursue, wherever I am.

Contents

List of Figures

List of Tables

Acronyms

ADLs	Activities of daily living
CNS	Central nervous system
DFR	Direct force reflection
DNP	Disc-like non-passive
DOF	Degree of freedom
EOP	Excess of passivity
INP	Input non-passive
ISP	Input strictly passive
LAR	Learn and replay
LFD	Learning from demonstration
LTI	Linear time-invariant
ONP	Output non-passive
OSP	Output strictly passive
PEB	Position error based
RHP	Right half plane
RT	Robotic therapy
SOP	Shortage of passivity
TDE	Time-delay estimation
TIL	Therapist-in-loop
TOOL	Therapist-out-of-loop

Chapter 1

Introduction

1.1 Motivation

The demand for rehabilitation therapy for post-stroke patients has been increasing due to the aging population. Currently, about 50,000 cases of stroke are reported in Canada each year. Over half of the stroke victims survive – currently a total of 300,000 people in Canada – and require rehabilitation. While 10% of stroke sufferers recover completely, the rest are left with permanent or long-lasting disability which, in addition to the ensuing economic effects, adversely impacts their quality of life. Each patient requires many lengthy hands-on therapy sessions with rehabilitation therapists, which are labour-intensive activities and place a significant burden on the healthcare system. This demand has motivated the incorporation of robotic systems into rehabilitation programs as robots are able to perform controlled and reproducible motions and are not subject to fatigue [1].

While in-home robot-assisted rehabilitation has the potential of increasing access to and lowering the cost of therapy, it faces the challenge of maintaining patient's motivation to participate in rehabilitation exercises regularly on his/her own [2]. Thus, the notion of home-based rehabilitation based on teleoperation ("telerehabilitation") is introduced in this thesis. Traditionally, a bilateral teleoperation system system consists of a human operator interacting with a master robot and remotely controlling a slave robot to perform a task in a remote environment [3]. In the proposed telerehabilitation case, the remote environment will also be a human. In other words, the therapist and the patient interact with the two ends of a teleoperation system. Telerehabilitation also enables rehabilitation services to be delivered over long distance to remote areas with limited access to rehabilitation services, which is highly relevant to Canada's situation.

This thesis develops a new approach to task-oriented telerehabilitation therapy aimed at partially automating the rehabilitation process by time-sharing a therapist. Human arm *mechanical impedance* measurement and robot *impedance* control will be used to achieve this goal. It also investigates the stability analysis tools of teleoperation systems with two or more human operators.

1.2 Organization of the Thesis

Chapter 2 presents background information to help the readers understand the context in which this research is carried out. A brief history of teleoperation systems is first presented, followed by an overview of the use of robotics in rehabilitation therapy. Finally, we introduce the emerging field of telerehabilitation where teleoperated robotic interfaces are used for remote rehabilitation therapy.

Chapter 3 proposes a "Learn and Replay" (LAR) telerehabilitation paradigm which is a potential solution to the therapist time-sharing concept mentioned in the literature but has never been implemented concretely. Different technical issues are investigated in this chapter for the implementation of the LAR paradigm for a 1 degree-of-freedom (DOF) screwdriving task, including teleoperation system modeling, human impedance measurement during execution of a task through teleoperation, and the impedance control of an industrial robotic arm for the autonomous completion of the screwdriving task. Experimental results showing the complete LAR system performance for the 1-DOF task are shown in this chapter. It is important to remember that the mechanical impedance is the dynamic relationship between force and motion, which can be represented by physical concepts such as inertia, viscosity and stiffness.

Chapter 4 is a step forward from Chapter 3. A 2-DOF peg-in-the-hole insertion task is considered in this chapter under the LAR paradigm. Technical issues specific to the 2-DOF task are presented in this chapter and the experimental results showing the successful implementation of the LAR paradigm are shown as well. Chapter 3 and Chapter 4 together provide two examples as proof of concept for the proposed LAR paradigm.

Chapter 5 proposes a series-shunt stability analysis approach to take into account the degree (or lack thereof) of passivity of one or multiple terminations (denoting human operators and remote environments) present in a multilateral haptic system. A priori information is used to classify the termination under consideration into one of several categories and then the series-shunt decomposition approach is applied to derive a new set of stability criteria that are more accurate and appropriate for systems such as telerehabilitation systems that involve active or excessively passive terminations.

The approach is applied to a bilateral and a trilateral teleoperation system as case studies and the resulting criteria are verified with experiments.

Finally, Chapter 6 summarizes the research work and suggests future directions of research.

1.3   Publications

Chapter 3 has been submitted to the 2015 IEEE International Conference on Robotics and Automation, Seattle, WA, USA. Chapter 5 was published in the 2014 IEEE Haptic Symposium, Houston, TX, USA [4].

1.4   Contributions of the Thesis

This thesis makes several novel contributions in areas of telerehabilitation, human arm impedance measurement, learning from demonstration (LFD) and multilateral haptic system stability analysis:

1. PROPOSAL OF A NOVEL TELEREHABILITATION PARADIGM. The LAR paradigm proposed in Chapter 3 and 4 is a novel telerehabilitation paradigm aiming at providing a solution to the therapist time-sharing concept, which was brought up in [5] without providing any concrete technical solution. The sequential process involving therapist-in-loop (TIL) and therapist-out-of-loop (TOOL) phases provides an original framework for partial automation of the telerehabilitation process and reducing rehabilitation costs for the health care system.

2. HUMAN ARM IMPEDANCE MEASUREMENT DURING UNPERTURBED TELEOPERATION TASK EXECUTION. The human arm impedance measurement technique presented in Chapter 3 and Chapter 4 is different from previous human arm impedance measurement techniques in that it does not restrict the subject's posture or requires large data size[6], nor does it require external force disturbances [7]. Another novelty in this regard is our use of the mechanical energy absorption/generation information during teleoperation task execution as a perturbation onset detection criterion in order to use task-intrinsic force signals as excitation inputs for arm impedance identification.

3. IMPEDANCE LFD IN TELEOPERATION. The LAR paradigm is a realization of the LFD concept as the robot is taught with demonstrations to behave in a certain manner. To our knowledge, this work is the first application of LFD concept in telerehabilitation field, which can

be very beneficial in that therapists are not required to configure or code the robot differently each time the task changes. Different from previous LFD realizations for teaching the robot a desired impedance [8], our work is done via the medium of teleoperation and impedance distortions introduced by teleoperation are also accounted for.

4. ACTIVITY OR STRICT PASSIVITY OF MORE THAN ONE TERMINATION AND UP TO ALL TERMINATIONS. The series-shunt approach proposed in Chapter 5 can be applied to n-port networks to allow, for the first time to our knowledge, up to n terminations to be active or strictly passive. In the telerehabilitation case for example, the therapist's role in assistive therapy can be modeled by an active termination, while his/her role in resistive therapy can be modeled by a strictly passive termination. Previous works only provided frameworks either for one of the termination to be active/strictly passive [9], [10], or did not allow terminations to be active at all [11], [12]. Another difference from [11] is that, while previous work requires the use of wave variables and scattering parameters, our approach yields results *directly* in the immitance (i.e. impedance or admittance) domain, which is more suitable for mechanical systems.

Chapter 2

Background

This chapter provides background information in teleoperation, therapeutic robotics and the emerging telerehabilitation field to better illustrate the context of our research. In Section 2.1, an overview of the teleoperation technology and its wide-range applications is given. In Section 2.2, we present the current state of robotic assistance in the area of rehabilitation. Finally, in Section 2.3 we look at how the new field of telerehabilitation can integrate teleoperation into rehabilitation and thus offer exciting new possibilities for patients.

2.1 Teleoperation Systems

2.1.1 A Brief History of Teleoperation and its Applications

Although the concept of extending the human arm reach has been around for centuries, the first mechanism resembling modern teleoperation systems was developed by Goertz at Argonne National Laboratory in 1945 [13]. The system was purely mechanical and was designed to enable safe handling of hazardous materials from the outside of a hot cell. The first electric master-slave teleoperation system was developed in 1954 [14], in which the master and slave devices were separated mechanically. In the 1960s, with growing teleoperation applications in space exploration, the effect of delay caught researchers' attention [15]. Supervisory control was developed to address the issue, where the exchange of information between the master robot and the slave robot is minimized by giving more autonomy to the slave robot. Moving into the 1980s, more advanced control theoretical methods were applied to analyze teleoperation system stability and performance, such as the network theory [16], scattering theory and passivity based control [17]. With the advent of the Internet

as the most common medium for data exchange, new technical challenges appeared such as varying time delay [18], discrete-time data sampling [19], and information loss [20]

Ever since the invention of the teleoperation system, it has found applications in more and more fields. Today, its applications are found primarily in but not limited to the following fields:

1. SPACE EXPLORATION. Teleoperation systems are used extensively in space programs. The first computer controlled teleoperation robot ROTEX was sent to space in 1993 on board the space shuttle Columbia [21]. The robot was able to be controlled both from within the spacecraft by astronauts and by NASA ground control in Houston via teleoperation.

2. RADIOACTIVE MATERIAL HANDLING. Teleoperation was initially developed for hazardous material handling and it is still widely used for this purpose. For example, a Stäübli RX 170 industrial manipulator was used for a maintenance operation via teleoperation in a nuclear spent fuel reprocessing plant in La Hague, France [22].

3. UNMANNED UNDERWATER VEHICLE OPERATION. The harsh underwater environment provides another natural field for teleoperation applications. For example, a teleoperation grasping system was developed for underwater construction purposes with the help of augmented reality technology [23].

4. TELESURGERY. The application of teleoperation technology to robot-assisted surgery is a relatively new field. The da Vinci Surgical System by Intuitive Surgical Inc. is one of the most well-known teleoperation systems in clinical use [24]. In 2001, a robot-assisted minimally invasive surgery was completed using a ZEUS surgical robot via teleoperation by a surgeon based in New York, USA, on a patient in Strasbourg, France [25].

Our ultimate goal is to extend the application of teleoperation to in-home rehabilitation.

2.1.2   Control Architectures for Bilateral Teleoperation

In general, a teleoperation system consists of a human operator, a remote environment, a master robot, a slave robot, and a communication & control system, as shown in Fig. 2.1. Mechanical energy is exchanged between the human operator and the master robot, and between the slave robot and the environment. Information is exchanged between the "Communication Channel & Robot Control" block and the master/slave robots; the control architectures discussed in the following paragraph applies to this block.

FIGURE 2.1: Schematic of a bilateral teleoperation system

Haptic feedback in teleoperation can be achieved with two-channel (2CH) or four-channel (4CH) control architectures [26]. A position-error-based (PEB) architecture sends the positions of each robot as the reference position to the other robot and the reflected force is calculated based on the difference in positions between the master and the slave robots. No interaction force measurement is required in the PEB architecture. In direct force reflection (DFR) architecture, while the slave robot follows the master robot's position, contact force between the slave and the environment is measured with a force sensor and sent back to the master robot. The master robot then determines its joint torques based on this slave/environment force measurement. Both PEB and DFR architectures are 2CH architectures as only two channels are needed for communication (two position channels in the PEB case, and one channel for position and another channel for force in the DFR case). By combining and extending the PEB and the DFR architectures, we can have a 4CH system, in which the robot joint torques are calculated based on both the positions and the force readings sent from the other robot.

In our application, although the PEB architecture is a cheaper solution to introducing haptic feedback in teleoperation in comparison with the DFR architecture, it does not provide enough transparency due to the heavy mechanics of the industrial manipulator used as the slave robot. In other words, a force that is not big enough will not be able to introduce enough displacement on the slave robot, which translates to practically no haptic feedback on the master robot if the PEB architecture is used. Therefore we have chosen to implement the DFR architecture for our LAR implementation such that the interaction forces acting on the slave robot can be faithfully fed back to the master robot.

2.2 Therapeutic Robotics

2.2.1 Brief History of Rehabilitation Robotics

Robotic prosthesis and orthotics was the primary focus in the early development of the field of rehabilitation robotics from 1950s to early 1990s. The emphasis was placed on using the robots to

help patients complete activities of daily living (ADLs) [27]. For example, robotic devices were developed to be mounted to a wheelchair or a desk to assist users with reaching for objects.

In late 1980s, researchers started to consider using robots as a *therapy* tool to address the cause of motor dysfunction by providing physical or cognitive therapy exercises. In 1988, a robotic system to flex and extend the knee for movement rehabilitation was developed [28]. Later, robotic free-reaching movement therapy was introduced for the upper-limb with an industrial Universal Machine Intelligence RTX robot [29]. A button was positioned by the robot in various locations and the patient was asked to reach out and touch it. Since then several rehabilitation robots were developed for upper-limb therapy, including the MIME [30], MIT-MANUS [1] and ARM Guide robots [31]. In the 2000s, following a modular design concept rehabilitation robots were further developed for therapy involving other parts of the body including gait training [32], ankle movement training [33], wrist training [34], and hand/finger training [35].

The motivation behind incorporating robots into rehabilitation therapy, which is traditionally administered and delivered entirely in a "hand-over-hand" manner (in its literal sense in the case of upper-limb post-stroke therapy) by therapists, is the fast growing demand for therapy from a growing ageing population. Integration of robotics into rehabilitation therapy is considered to be able to improve the efficiency of the therapy, as robots can help alleviate the pressure and physical work that therapists have to put into rehabilitation therapy [1].

2.2.2   Effect of Robotic Therapy on Motor Function Recovery

Ever since the emergence of rehabilitation robots, researchers have been investigating the effect that robotic therapy (RT) can have on the motor function recovery process. However, the exact impact of RT on motor recovery is still unclear. Studies on the MIT-Manus system were first conducted on stroke patients' arm motor function recovery after stroke. Results showed that patients had reduced shoulder and elbow motor impairment compared to those who did not receive RT and the difference was still statistically present at a 3-year follow-up [36], indicating that supplemental RT can enhance motor function recovery. Other studies involving the MIME system also compared the therapy outcome between patients who received RT and patients who received conventional therapy with similar intensity. Results showed that robot involvement improved motor function recovery in terms of the Fugl-Meyer score, gains in muscle strength, and reach extent compared to conventional rehabilitation therapy [37], suggesting that RT can be comparable to or even more effective than conventional rehabilitation therapy. However, there are also studies that showed that patient' improved motor function does not necessarily translate into better performance in ADLs,

which is arguably the most important goal for rehabilitation therapy [38]. Studies done in [39] raised the challenge of distinguishing the contribution from movement practice and from application of robotic forces towards the observed improved motor function recovery. This question is important because if movement practice turns out to be the dominant stimulus for motor function recovery, there is no need to involve actuated robots in the rehabilitation therapy.

Although currently there is no consensus on the impact of RT on motor function recovery process, the need for rehabilitation robots is still there, as RT has proven useful in providing help to therapists, especially for physically demanding therapies [40]. Robots can also be used to increase training intensity for patients as they can continue to provide therapy services outside of the therapists' available hours. Rehabilitation robots can thus increase the productivity of therapists and consequently help in reducing health care costs and increasing therapy availability. Another advantage of the rehabilitation robotics is that once combined with teleoperation, rehabilitation therapy accessibility can be further increased. This will be the topic of Section 2.3.

2.3   Telerehabilitation Robotics

Telerehabilitation refers to delivering rehabilitation therapy to a patient from a remote location with the help of rehabilitation robots.

Current telerehabilitation technologies can be grouped into unilateral and bilateral teleoperation systems [41]. In the unilateral systems, only the patient interacts with a robot and the therapist can provide instructions to the patient via the Internet (in the form of instant messageing, voice/video conferencing, etc.). Data from the patient side is sent to the therapist via the Internet as well. Examples of such systems include the JavaTherapy system [31] and the Rutgers Master II system [42]. In bilateral teleoperation systems, the patient and the therapist interact with each other haptically (through the slave and the master, respectively) either directly [5] or indirectly through a virtual environment [43]. In [43], the patient and the therapist were able to engage in haptic interaction by cooperatively manipulating an object in a virtual environment. In [5], wrist-worn haptic devices were used by the therapist and the patient to haptically interact via bilateral teleoperation and perform rehabilitation therapy. The same paper discussed the concept of time-sharing a therapist, where the therapist would deliver therapy to multiple patients by the master robot while the slave robot would learn the therapist's behaviour and carry it out automatically when the therapist shifts his attention to another patient. However, no proposal was made with regard to how to teach the slave robot the proper interactions it has to have with the patient.

This thesis is interested in home-based rehabilitation based on haptic teleoperation. In this context, a hospital-based therapist is haptically linked and telepresented to a home-based disabled patient in order to effectively simulate traditional in-hospital therapies, e.g., those in which a therapist physically helps and cooperates with a patient in performing therapy tasks, over a distance. Stability of such systems has been investigated in [44] and [45].

Although the field of telerehabilitation is still in an early stage of development, it holds the key to providing solutions to the following needs in rehabilitation:

1. DELIVERING REHABILITATION THERAPY TO REMOTE AREAS. Telerehabilitation can be used to deliver rehabilitation therapy to patients living in remote areas or to patients who have limited access to transportation. This is particularly appealing to Canada, which has a vast geography and very low population density.

2. INCREASING PATIENT MOTIVATION AFTER DISCHARGE FROM HOSPITAL. Upon discharge from the hospital, patients often suffer from a lack of motivation to continue therapy exercises, which hinders their recovery [46]. By involving therapists in the after-discharge recovery phase through teleoperation, patients will kept motivated at a reduced cost and improved convenience compared to face-to-face therapy.

3. REMOTE MONITORING OF THE PATIENT RECOVERY PROGRESS. Telerehabilitation will enable therapists to monitor the patient recovery after their discharge from the hospital, as robotic devices can be used to provide clinically relevant information. Robots can be used to record position and force information of the patient during therapy sessions and such data can be analyzed with information technology for patient recovery assessment. For example, [6] is a first step towards establishing correlation between patient arm impedance and motor function recovery.

Chapter 3

Learn-and-Replay Telerehabilitation Paradigm: 1-DOF Task

3.1 Introduction

The demand for rehabilitation therapy for post-stroke patients has been increasing due to the ageing population. Each patient requires many lengthy hands-on therapy sessions with rehabilitation therapists, which are labour-intensive activities and place a significant burden on the healthcare system. This demand has motivated the incorporation of robotic systems into rehabilitation programs as robots are able to perform controlled and reproducible motions and are not subject to fatigue. This helps to relieve the therapists from repetitive hands-on therapy exercises. One key question we ask in this chapter is given the limited computer programming know-how available in clinical settings, can certain desired robot behaviours be learned after qualitatively demonstrating the task to the rehabilitation robot by the therapist in order to free the therapist from repetitive actions?

Previous research suggests that the human displays task-dependent impedance via the incorporation of inverse dynamic models and impedance control while interacting with the environment [47]. The central nervous system (CNS) learns the optimal impedance for a specific interaction and while the interaction can be intrinsically unstable, stability is achieved via regulating the mechanical impedance in the human arm [48]. Previously, human impedance regulation skills have been transferred to robots by using the electromyography (EMG) signals to estimate the human arm impedance during teleoperation [49]. Probabilistic approaches such as learning from demonstration

(LFD) using a gaussian mixture model [8] have also been employed to capture the impedance pattern of two humans in haptic interaction during a hardware assembly task. The impedance pattern was then reproduced by a robot for autonomous robot-human collaboration.

In the context of bilateral telerobotic rehabilitation, the idea explored in this chapter is to make the slave (patient-side rehabilitation) robot learn the endpoint impedance (the dynamic relationship between the force applied and motion) displayed by the therapist during a task and then emulate the therapist behaviour specific for the task. In the current chapter and the following chapter (Chapter 4), we will refer to the patient-side robot the "slave" robot and the therapist-side robot as the "master" robot. Note that this nomination is different from the conventional nomination for teleoperation systems as we have human operators on both sides of the teleoperation system. Our appellation of "master" or "slave" is therefore an arbitrary choice.

In this chapter, we propose a novel paradigm called learn and replay (LAR) to realize direct bilateral telerehabilitation that encompasses two distinct phases to achieve time-sharing of a therapist. During the first phase, the therapist interacts directly with a patient through bilateral teleoperation (Fig. 3.1(a)) to complete a cooperative task. This stage is called the therapist-in-loop (TIL) phase. In the meantime, the therapist's task-specific impedance is measured through the master robot. During the next stage, the therapist is no longer in the rehabilitation loop, thus giving rise to the therapist-out-of-loop (TOOL) phase (Fig. 3.1(b)). In the TOOL phase the therapist's measured arm impedance is displayed by the slave robot via an impedance control loop to the patient so that the cooperative rehabilitation task can be carried on in the absence of the therapist. In this way, the proposed LAR paradigm allows for teaching a rehabilitation robot at patient's home new desired therapy oriented behaviours by *demonstrating* the task rather than explicitly *programming* it through machine commands. This is useful in clinical settings where the therapist has knowledge of the task to achieve but not the ability to accordingly reprogram/reconfigure the robot. Ultimately, this LAR paradigm also facilitates time-sharing the same therapist across multiple home-based patients engaged in task-oriented therapy. The therapist can engage the next patient in TIL phase while the previous patient starts TOOL phase exercises. The different therapist arm impedances related to different patients and different therapy tasks will be identified and emulated by different slave robots. Finally, the LAR paradigm is also particularly useful for sophisticated impedance-based rehabilitation tasks (in addition to simple trajectory following tasks).

This chapter is organized as follows: First, we give a description of the master-slave teleoperation system including its control architecture as well as a representative cooperative task for therapy in Section 3.2. In Section 3.3, we introduce the method used for human arm impedance measurement in the TIL phase without interrupting the normal flow of the therapy task. In Section 3.4, we present
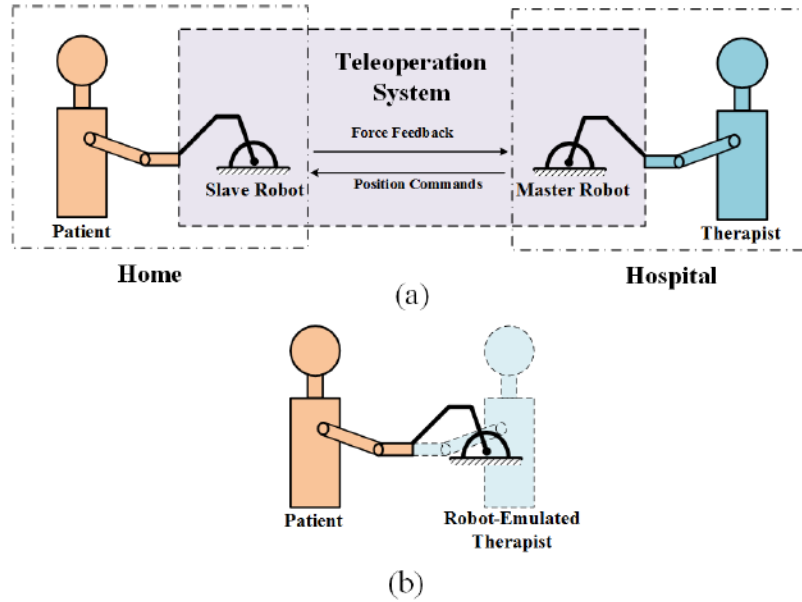
FIGURE 3.1: Illustration of the proposed LAR paradigm with (a) TIL phase, where the hospital-based therapist interacts with the home based patient via a teleoperation system, and (b) TOOL phase where the therapist's behaviour is emulated by the patient-side robot

the impedance control implementation for the slave robot during the TOOL phase. In Section 3.5, we present the results for the therapist arm impedance estimation at the master side during the TIL phase and the patient-robot impedance-based interaction at the slave side during the TOOL phase. Finally, Section 3.6 presents concluding remarks.

3.2   Telerehabilitation System and Therapy Task

In this section, we first describe the task to be done cooperatively by a patient and a therapist. Next, we present a teleoperation system appropriate for performing the therapy task in the telerehabilitation mode. Then, we present the kinematics and dynamics of the master and slave robots of the telerehabilitation system and describe the teleoperation controller used in the system. Finally, we derive the teleoperation system's hybrid matrix to be used in a following section in order to account for the impedance distortion caused by the teleoperation system dynamics.

3.2.1   Therapy Task

Consider a task in which a screw is driven by the patient into a surface held in position by the therapist as shown in Fig. 3.2(a). For this screwdriving task to be done in the proposed telerehabilitation
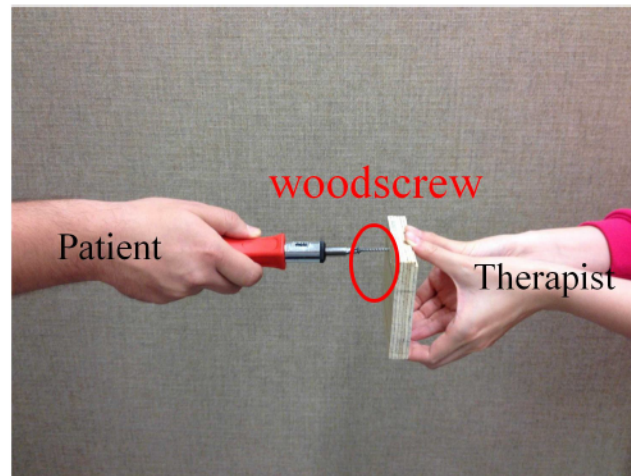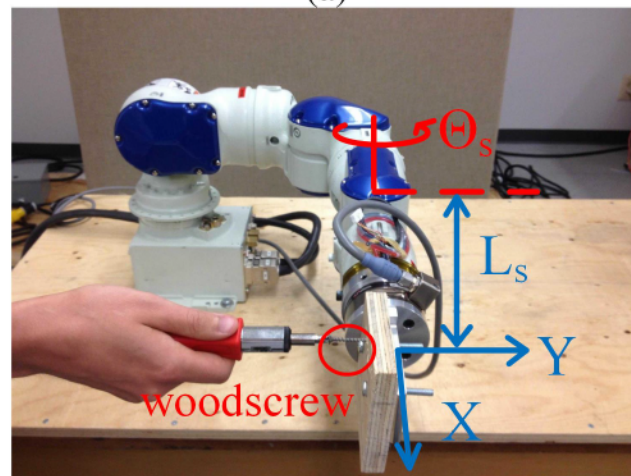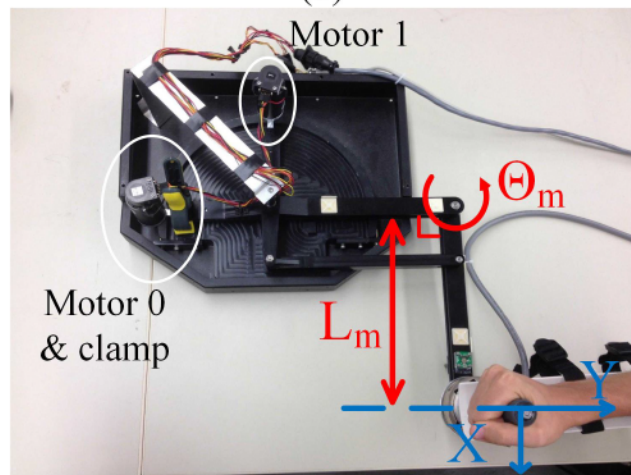
FIGURE 3.2: (a) Direction manipulation: the screwdriving task without using any robots. (b) Configuration of the slave (patient-side) Yaskawa Motoman SIA5F robot. (c) Configuration of the master (therapist side-side) rehabilitation robot.

context, the patient will be tasked to drive the woodscrew into the wooden plate attached to the end-effector of a slave robot (7-DOF SIA5F robot from Yaskawa Motoman, Miamisburg, Ohio, USA, as shown in Fig. 3.2(b)) that is teleoperated by the therapist from a master user interface (2-DOF planar rehabilitation robot from Quanser, Inc., Markham, Ontario, Canada, as shown in Fig. 3.2(c)). Thus, in the TIL phase, while the patient uses a screwdriver to drive the screw into the wooden plate fixed to the slave robot, the therapist firmly holds the master haptic device in position. For the realization of this teleoperation system, readers can get more information in Appendix B, Appendix C and Appendix F.

3.2.2   Telerehabilitation System

Although both the master and slave are multi-DOF robots, they have been configured to accommodate the aforementioned task, which naturally involves only a 1-DOF motion in the Cartesian space. Consider motor 1 of the master robot and the sixth joint of the slave robot corresponding to the joint angles θ_m and θ_s in Fig. 3.2, respectively. The slave position θ_s is made to follow the master position θ_m while interaction forces at the slave side are reflected back to the master side. The second joint of the master robot is passively (physically) clamped in its home position with the corresponding motor (Motor 2) turned off, while the other 6 joints of the slave robot are actively held in position via high-gain PID position control. In Fig. 3.2, both robots are at their home positions ($\theta_m = \theta_s = 0$). Cartesian frames are attached to the end-effectors of the master and the slave as shown in Fig. 3.2. Note that for small θ_m and θ_s, the motions of the two robots can be approximated to be along a Cartesian axis. The task is therefore in the Y direction. Through teleoperation, the therapist tries to resist the pushing forces of the patient applied in the Y direction by displaying a stiff impedance to the master robot in that direction, so that the patient can complete the screwdriving task.

3.2.3   Master and Slave Robots Kinematics

Given that the screwdriving task takes place in the Cartesian space while the robots are controlled in the joint space, there is a need to consider the robots' kinematics for robot control purposes. The link lengths for the master and slave robot are L_m and L_s, respectively, measuring from the rotating axes to the centre of the handle for the master robot (Fig. 3.2(c)) and to the screw location on the wooden plate for the slave robot (Fig. 3.2(b)). The kinematic position and velocity mappings
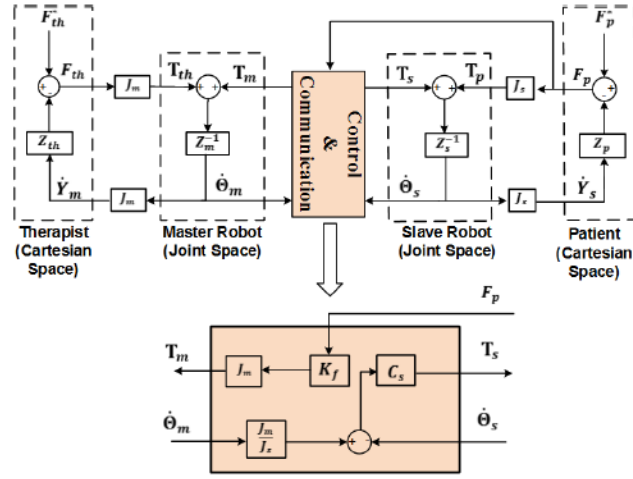
FIGURE 3.3: Schematic of the DFR teleoperation architecture.

between the joint space and the Cartesian space are

$$y_{m,s} = L_{m,s} \cdot sin(\theta_{m,s}) \tag{3.1}$$

$$\dot{y}_{m,s} = L_{m,s} \cdot cos(\theta_{m,s}) \cdot \dot{\theta}_{m,s} = J_{m,s} \cdot \dot{\theta}_{m,s} \tag{3.2}$$

where the subscripts m, s denote the master or the slave, respectively.

Denoting the torques applied by the motors on the robot joints by τ_m and τ_s, the relationship between joint torques and Cartesian end-effector forces in the Y direction is also related through the Jacobian:

$$\tau_{m,s} = J_{m,s} \cdot f_{m,s} \tag{3.3}$$

When external Cartesian forces are applied to the robots by the therapist (denoted by f_{th}) or by the patient (denoted by f_p) in the Y direction, they can be converted to torques applied to the robot joints (τ_{th}) and (τ_p) in the same manner. Such external forces along the Y direction are measured by two ATI Gamma NET force/torque transducers (Apex, NC, USA) attached to the end-effectors of the two robots at 1 kHz sampling rate. The communication channel is implemented using the Winsock application programming interface over the Ethernet using the UDP protocol at 1 kHz sampling rate – the same rate as the one used in the robot control loops (for reading encoders and issuing torque commands) of both robots.

3.2.4 Telerehabilitation System Controller

Direct force reflection (DFR) architecture is used for control of the bilateral telerehabilitation system. In the DFR architecture, the slave robot follows the position of the master robot while the master robot displays to the human operator the interaction forces measured by a force sensor at the slave robot's end-effector. For details of this teleoperation control method, readers can refer to [26]. A detailed schematic of the bilateral teleoperation system is presented in Fig. 3.3 where T_s is the output of a joint-level position controller and T_m is the torque to be reflected by the master robot to the human in contact with it (therapist). Note that the time domain variables are capitalized here to refer to their frequency domain equivalences.

In Fig. 3.3, (3.2) and (3.3) convert joint velocities into Cartesian velocities and Cartesian forces into joint torques. Also, as mentioned before, F_{th} and F_p are the Cartesian forces applied to the master and slave robots by the therapist and patient, respectively. Z_m and Z_s are the impedance transfer functions of the master and the slave robots in the joint domain relating joint velocities to joint torques. The master robot can be modeled as an inertia, $Z_m = M_m s$, as it is a haptic device used by the therapist. The slave robot is modeled as an inertia and a damper because it has significant damping and friction needing to be modeled: $Z_s = M_s s + B_s$. Z_{th} and Z_p refer to the arm impedances in the Cartesian domain of the therapist and the patient, respectively. C_s is the PD position controller for the slave robot, $C_s = K_{vs} + K_{ps}/s$. K_f is the force reflection gain to the master robot.

For our analysis, we first make the simplification that $cos(\theta_m) \simeq 1$ and $cos(\theta_s) \simeq 1$ based on the assumption that θ_m and θ_s are small angles within 10°. This assumption will indeed be verified in Section 3.5 and is guaranteed by the nature of the task used for case studies in this chapter. This assumption only introduces a worst error of 3% in (3.2) and (3.3), which we deem to be insignificant.

With this assumption, the simplified system dynamics derived from Fig. 3.3 in frequency domain are

$$(F_{th} + F_p \cdot K_f) \cdot L_m^2 = Z_m \cdot \dot{Y}_m \tag{3.4}$$

$$F_p \cdot L_s + \frac{C_s}{L_s} \cdot \dot{F}_m = \frac{C_s + Z_s}{L_s} \cdot \dot{Y}_s \tag{3.5}$$

Equations (3.4) and (3.5) can be manipulated into the 2-port network hybrid matrix representation as

$$\begin{bmatrix} F_{th} \\ -\dot{Y}_s \end{bmatrix} = \begin{bmatrix} h_{11} & h_{12} \\ h_{21} & h_{22} \end{bmatrix} \begin{bmatrix} \dot{Y}_m \\ F_p \end{bmatrix} \tag{3.6}$$

with $h_{11} = \frac{Z_m}{L_m^2}$, $h_{12} = -K_f$, $h_{21} = -\frac{C_s}{C_s+Z_s}$ and $h_{22} = -\frac{L_s^2}{C_s+Z_s}$.

3.3 Identification of Human Arm Impedance

In this section, we first have an overview of the human arm impedance techniques employed in the literature. Then, based on the nature of the task and the requirement to not disrupt the normal flow of teleoperation during the TIL phase, we present the human arm impedance strategy that this work utilizes.

3.3.1 Human Arm Impedance Identification in the Literature

The mechanical impedance of the human arm is often measured via system identification methods. Either position or force perturbations are applied by a robot to the hand and the resulting force and motion response is analyzed to fit typically to a second-order impedance model. For example, in [50], a planar robot was used to impose step position disturbances to the human hand, enabling the calculation of the endpoint stiffness of the arm in the Cartesian plane. Later, dynamic components, i.e. damping and inertia were added to the impedance model [51], [52]

In rehabilitation, the mechanical arm impedance can potentially serve as a quantifiable index to measure patient recovery. In [6], both position and force perturbations have been applied to the arm to identify a second-order impedance model. When force perturbations are applied, the subject is required to maintain a certain posture. While this approach maximizes the model precision and consistency, it is geared toward assessing patient recovery and not therapists. It will be impractical for the TIL phase of our proposed LAR telerehabilitation paradigm, as to restrain the therapist to a certain posture during the entire session of therapy does not facilitate therapy.

The endpoint impedance of the human arm can be measured in a real-world task by applying short, impulsive force perturbations to the arm during execution of the task [7]. During a welding task, force perturbations with 3N amplitude and 100 ms duration were exerted on the hand holding the weld gun. Segments of data immediately following the onset of perturbations with 200 ms of duration were used to identify a second-order impedance model. While this approach used very brief force perturbations in order to minimize the impact on task execution, such a scheme will be inconvenient if used in our TIL phase as the motions introduced on the therapist's arm following such disturbances may confuse the patient on the other side of the teleoperation and hamper the execution of the cooperative task.

3.3.2   The Proposed Human Arm Impedance Strategy

The strategy used in our project is similar to the approach used in [7] with the difference that no extra force perturbations are added. Essentially, the very pushing forces imported by the patient that occur naturally during the screwdriving task are regarded as force disturbances, and a relatively short duration of data is used to identify a second-order passive impedance model for the human arm. We define a "zero position" corresponding to $\theta_m = 0°$ and display it to the therapist via a computer monitor. We do so because it is desirable that the therapist tries to return to the zero position after each perturbation, not only because of the small-angle assumption made in Section 3.2.4, but also because such behaviour is consistent with what happens in the regular screwdriving task where the person holding the wooden plate would try to maintain it in a fixed position.

A challenge we face is that, unlike [7], we do not have an a priori force perturbation sequence and therefore determining the onset of force perturbations is a challenge. As a workaround, let us first analyze the energy

$$E_{absorbed} = \int_0^T -f_{th}(t)\dot{y}_m(t)\,\mathrm{d}t \tag{3.7}$$

absorbed by the therapist's arm during a typical task over timespan T (for our 1-DOF system). As shown in Fig. 3.4(a), each rising edge of the absorbed energy corresponds to a pushing force onset. The initial negative energy corresponds to the adjustment movements of the therapist as he grabs onto the handle attached to the master robot's end-effector shown in Fig. 3.2(c). During the task, the therapist's arm absorbs more energy than what it gives out when the arm returns to the zero position, showing that the arm is passive for this task. The energy absorption provides us with a good criterion to determine the onset of force perturbations, as it clearly distinguishes when the arm is moving voluntarily (during adjustments of the arm position, for example) from when the arm is moving involuntarily (when the arm is knocked away by the force perturbation). Therefore the onset of a force perturbation is determined by the moment when $\dot{E}_{absorbed}$ in (3.7) becomes positive (i.e. when energy absorption by the arm begins). A typical perturbation onset determination result is shown in Fig. 3.4(b). As can be seen, it would be difficult to determine the perturbation from the force signal alone as it shows no clear distinction between voluntary movement and involuntary movement.

After the perturbation onset is determined to be at time t_p for each perturbation, we will try to determine the following impedance model with respect to force and position data in the time window $[t_p, t_w]$:

$$M\ddot{y}(t) + B\dot{y}(t) + Ky(t) = -f(t),\ t \in [t_p,\ t_w] \tag{3.8}$$
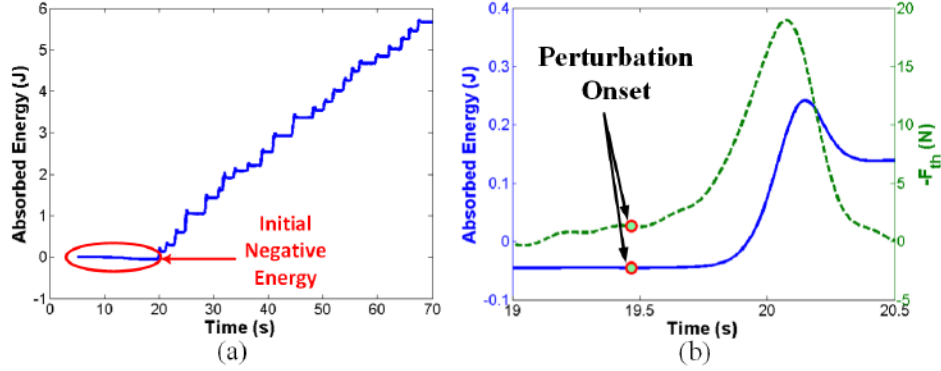
FIGURE 3.4: The energy absorbed by the therapist's arm (a) during the entire session of a typical screwdriving task and (b) within one perturbation (in solid line), superimposed on the force (in dotted line) applied on the therapist's arm by the master robot. The identified onset of the perturbation is indicated by a green circle on both curves.

where $y(t) = y_{th}(t) - y_{th}(t_p)$, $f(t) = f_{th}(t) - f_{th}(t_p)$ and t_w is a selected time window end. Note that we subtract the force and position/velocity/acceleration readings at time t_p in order to consider only the force and position/velocity/acceleration *changes* arising from the disturbance. With (3.8) the frequency domain arm impedance transfer function Z (between velocity input and force output) is written as

$$Z = M \cdot s + B + \frac{K}{s} \qquad (3.9)$$

Linear least-squares regression is used to identify the impedance model in (3.8). The force and position signals from the entire TIL session are filtered with a Savitzky-Golay filter of order 6 and window size of 101 data samples for smoothing and then filtered with a Butterworth low-pass filter of order 5 and cut-off frequency at 5 Hz. 5 Hz was chosen because spectrum analysis on the measured signals indicated that frequency content above 5 Hz was negligible for our experiments. Other signal processing parameters were chosen so that the identification method provided the best results in identifying the known impedance parameters of a mass-spring system. Velocity and acceleration signals are obtained with central differencing of the filtered position data.

Determination of t_w in (3.8) depends on the desired duration of the data window T_w as $t_w = t_p + T_w$. In [7], T_w was chosen to be 200 ms as a compromise between the need to use as little data as possible (to accommodate the 100~150 ms window in which the human cannot react voluntarily to the abrupt motion and therefore the arm impedance does not change [53]) and the model identification calculation that requires sufficient data points. In that work, 200 ms was found to provide all positive impedance values (positive M, B, K in (3.8)) for over 90% of the perturbations. In our case, due to the uncertain nature of the patient-applied (rather than robot-generated) perturbation, we determine
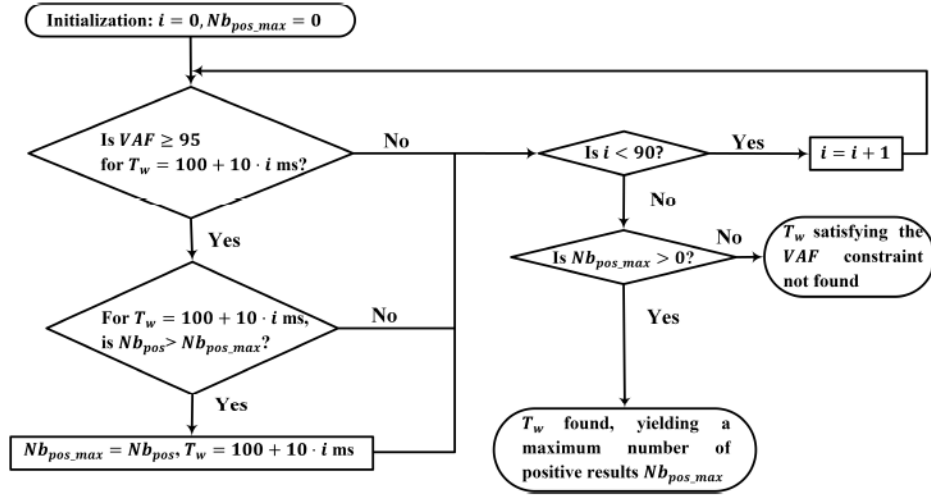
FIGURE 3.5: Flowchart showing the algorithm for choosing T_w

a time window length while taking into consideration the goodness of model fit that we measure using the variance accounted for (VAF) test statistic for each perturbation from t_p to $t_p + T_w$, with T_w incrementing from 100 ms to 1000 ms at steps of 10 ms:

$$VAF = 100 \times \left(1 - \frac{var\left(f_{th}(t) - \hat{f}_{th}(t)\right)}{var(f_{th}(t))} \right), \ t \in [t_p, \ t_w] \tag{3.10}$$

Here $\hat{f}_{th}(t)$ is the force applied to the master robot by the therapist's arm as predicted by the identified arm impedance model for a given position trajectory. f_{th} is the actual force applied to the master robot by the therapist.

In this work, the strategy used to determine T_w is formulated as follows: for one TIL session, find the minimum $T_w \in [100 \ ms, 1000 \ ms]$ such that the number of all positive-valued identified impedances, Nb_{pos} is maximized subject to the constraint that the average VAF value for the all-positive impedance identification results should be above 95. The algorithm is summarized in the flowchart in Fig. 3.5.

The rationale behind our strategy of T_w determination lies in the three observations from Fig. 3.6 which shows the impedance identification results as a function of the time window length for a typical TIL session of the screwdriving task. Fig. 3.6(a) shows that Nb_{pos} tends to increase (eventually to include all 20 perturbations) when data length T_w increases. Remember that we want to obtain all-positive impedance identification results because of the human arm passivity observed in Fig. 3.4. Fig. 3.6(b) shows that VAF tends to decrease as T_w increases beyond a certain threshold, as voluntary reactions may kick in if longer data lengths are considered. Thus it is necessary to incorporate VAF as a constraint in order to guarantee the good fit of the identified model. The upper

bound of T_w is chosen to be 1s because it is the time that the next perturbation may be applied. Finally, Fig. 3.6(c)-(e) show that the average M, B, K for all-positive impedance identification results tend to stabilize when Nb_{pos} reaches its maximum. Together with the consideration of minimizing the effect of voluntary reactions we decided to use the minimal T_w that enables the maximum Nb_{pos} while guaranteeing a high enough level of VAF. For this particular TIL session considered, the algorithm yields $T_w = 530\ ms$, with which all 20 perturbations give all-positive impedance models. In Fig. 3.6(f), the validation result for one perturbation (origin of the time axis represents the determined onset) is shown over the determined span of $T_w = 530\ ms$ with $VAF = 95$.

3.4   Impedance Control of Yaskawa Motoman SIA5F robot

In this section, we first discuss the impedance controller implemented on the slave robot during the TOOL phase, once we have the desired impedance parameter M_d, B_d and K_d. Then we discuss the derivation of the desired impedance to be implemented in the TOOL phase.

3.4.1   Impedance Controller Design

Impedance control of a robot can be achieved with model-based approaches or model-free approaches. Model-based approaches such as the one introduced in [54] require the exact knowledge of robot dynamics including joint friction. In our application with an industrial robot, while most dynamic terms can be calculated or estimated, the joint friction is hard to obtain. Unlike the master haptic device which is designed to have low friction, there is considerable friction in the slave robot joint that concerns us. The simple yet widely used coulomb + viscous friction model performed poorly because first, the linear model cannot capture the highly nonlinear friction in reality. The model's dependency on velocity also makes static friction compensation ineffective, and in our system the stiction is very large (in the order of 9 N.m in the joint space). Elaborate nonlinear models such as the LuGre model [55] can capture various non-linear phenomena such as the Stribeck curve, stiction and presliding displacement, but it is difficult to identify its parameters. In [56] a simpler approach is presented to determine a LuGre model, but the approach remains largely empirical and requires very refined encoder resolution (especially for measuring the presliding state). In addition, the dynamic nature of the LuGre model makes it a potential source of numerical instability in real-time friction compensation implementations.
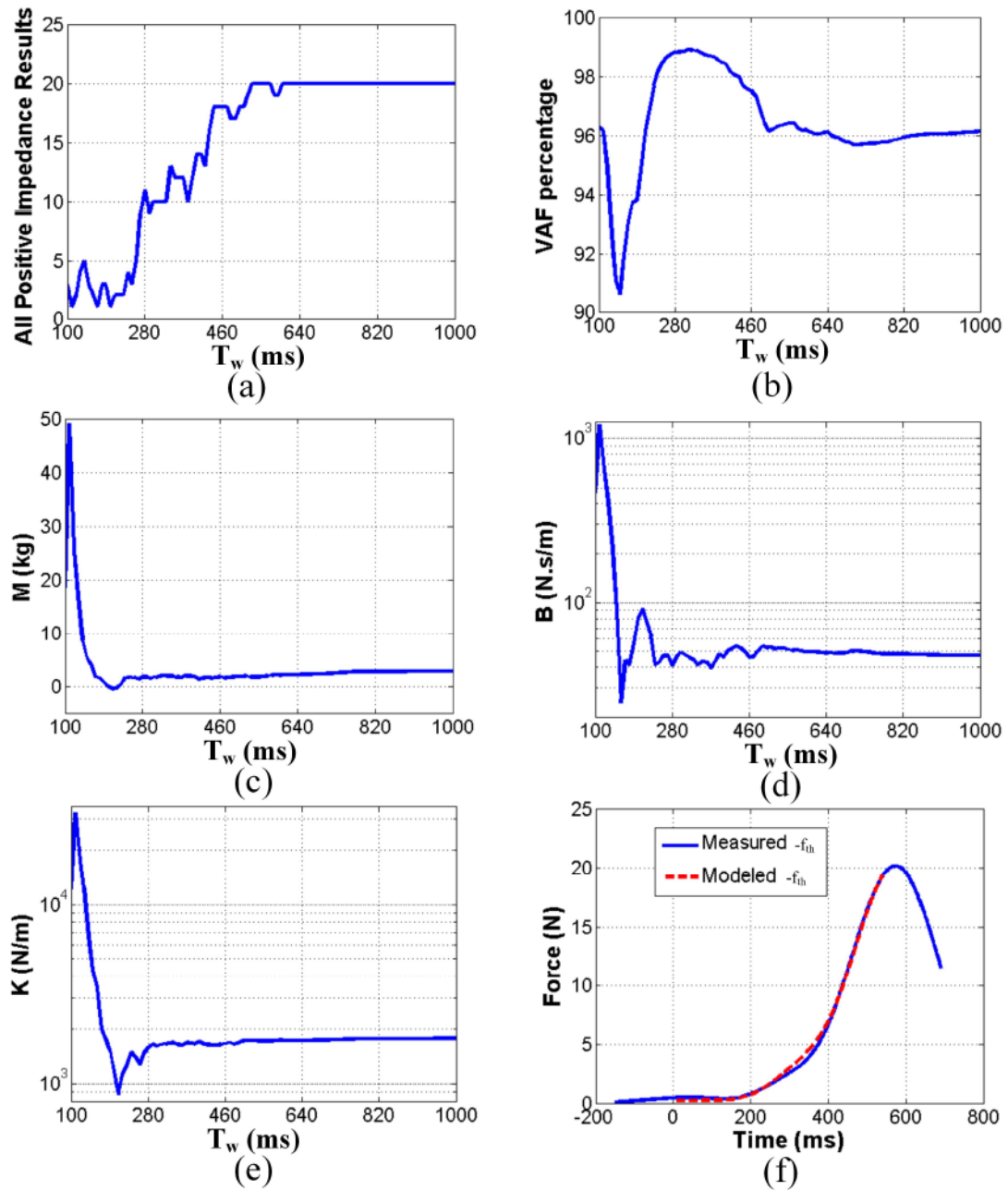
FIGURE 3.6: Impedance identification results as a function of data window lengths for a typical TIL session: (a) the number of all-positive impedance identification results, (b) average VAF value in percentage of all-positive impedance identification results (c) average M (d) average B e) average K of all-positive impedance identification results, (f) impedance model validation with modeled $-f_{th}$ compared to measured $-f_{th}$ for one perturbation with the determined window size at 530 ms and VAF value at 95

Given the considerable difficulties associated with determining the robot joint friction precisely, we decided to implement the impedance control with a mode-free approach. The Time-Delay Estimation (TDE) scheme [57] is such an approach, which can accurately and efficiently estimate the robot non-linear unmodeled dynamics. Let us write the rigid-body dynamics of the slave robot as

$$M_s\ddot{\theta}_s + f(\theta_s, \dot{\theta}_s) - \tau_p = \tau_s \tag{3.11}$$

Remember that M_s denotes the moment of inertia of the slave robot around the rotation axis, θ_s refers to the slave robot's joint angle, f denotes joint friction, τ_p is the external joint torque caused by the Cartesian force f_p applied by the patient ($\tau_p = J_s \cdot f_p$), and τ_s is the controller motor torque in the joint space. Now, let $\bar{M}_s$ denote the nominal value of inertia. We have

$$\bar{M}_s\ddot{\theta}_s + (M_s - \bar{M}_s)\ddot{\theta}_s + f - J_sf_p = \tau_s \tag{3.12}$$

Let us group together all uncertain terms:

$$N = (M_s - \bar{M}_s)\ddot{\theta}_s + f \tag{3.13}$$

This term can be estimated by the TDE scheme by assuming that N is continuous or at least piecewise continuous with respect to time t. We can approximate N at time t by its value at $t - L$ where L is a sufficiently small time delay (or number of sample points). From (3.12) and (3.13):

$$\hat{N}(t) = N(t - L) = \tilde{N}$$
$$= \tilde{\tau}_s + \tilde{J}_s\tilde{f}_p - \bar{M}_s\tilde{\ddot{\theta}}_s \tag{3.14}$$

where $\hat{N}$ denotes the estimated value of N at time t and the tilde symbol (also later in (3.22)) denotes the time-delayed value of the corresponding variable (by L sample points). The Cartesian force f_p is used because it is directly measured with the ATI force sensor in the Cartesian space.

Now, consider the control law

$$\tau_s = \bar{M}_s \cdot a_q + \hat{N} - J_sf_p \tag{3.15}$$

where a_q is the reference joint acceleration. By combining (3.11) and (3.15) we have $\ddot{\theta}_s = a_q$. For the impedance controller, the target dynamics is assumed to be

$$M_d(\ddot{y}_s - \ddot{y}_{sd}) + B_d(\dot{y}_s - \dot{y}_{sd}) + K_d(y_s - y_{sd}) = f_p \tag{3.16}$$

where $\ddot{y}_{sd}$, $\dot{y}_{sd}$ and y_{sd} denote the desired slave robot acceleration, velocity and position.

Let a_y be the reference acceleration in Cartesian space, and let

$$a_y = J_s \cdot a_q + \dot{J}_s \cdot \dot{\theta}_s \qquad (3.17)$$

or equivalently

$$a_q = J_s^{-1} \cdot (a_y - \dot{J}_s \cdot \dot{\theta}_s) \qquad (3.18)$$

Together with the kinematic relationship linking joint space acceleration with Cartesian space acceleration:

$$\ddot{y}_s = J_s \cdot \ddot{\theta}_s + \dot{J}_s \cdot \dot{\theta}_s \qquad (3.19)$$

we have from (3.16) and (3.17) that

$$\begin{aligned} \ddot{y}_s &= a_y \\ &= \ddot{y}_{sd} - M_d^{-1} \cdot [B_d(\dot{y}_s - \dot{y}_{sd}) + K_d(y_s - y_{sd}) - f_p] \end{aligned} \qquad (3.20)$$

Further, take (3.20) into (3.18), and then combining with (3.15) we have

$$\tau_s = \bar{M}_s J_s^{-1} \{ \ddot{y}_{sd} - M_d^{-1} \cdot [B_d(\dot{y}_s - \dot{y}_{sd}) + K_d(y_s - y_{sd}) - f_p] - \dot{J}_s \dot{\theta}_s \} + \hat{N} - J_s f_p \qquad (3.21)$$

Because we want the estimate to be as close as possible to the actual value, the time delay L is taken to be 1 sample point: so we use the data from current time t minus 1 *ms* to estimate the uncertain N term in (3.13). The known value of inertia $\bar{M}_s$ is selected with the objective of guaranteeing a fast estimation convergence rate. It is determined by first choosing a small positive value for $\bar{M}_s$ and then gradually ramping it up until the system starts making noisy response [57].

Finally the control torque can be expressed in the following form for implementation:

$$\begin{aligned} \tau_s = \frac{\bar{M}_s}{L_s cos(\theta_s)} \{ \ddot{y}_{sd} &- M_d^{-1} \cdot [B_d(L_s cos(\theta_s)\dot{\theta}_s - \dot{y}_{sd}) \\ &+ K_d(L_s sin(\theta_s) - y_{sd}) - f_p] + L_s sin(\theta_s)\dot{\theta}_s^2 \} \\ &+ \tilde{\tau}_s + L_s cos(\tilde{\theta}_s \tilde{f}_p - \bar{M} \tilde{\ddot{\theta}}_s) - L_s cos(\theta_s) f_p \quad (3.22) \end{aligned}$$

where $\ddot{y}_{sd}$, $\dot{y}_{sd}$ and y_{sd} are all equal to 0 for the considered task.

3.4.2 Derivation of Desired Impedance

After Z_{th} is estimated during the TIL phase as discussed in Section 3.3, we will be able to calculate the desired impedance to be specified for the impedance controller regulating the relationship between f_p and $\dot{y}_s$ during the TOOL phase. The desired impedance will be the impedance displayed by the slave robot during the TIL phase as this is the impedance that helped to successfully complete the cooperative task with the patient. Thus it is necessary to account for the possible impedance distortion caused by the teleoperation system dynamics and it is desirable to investigate what will be the displayed impedance $Z_d(s) = -F_p(s)/\dot{Y}_s(s)$ as a function of the measured Z_{th} and the teleoperation system parameters that quantify its transparency.

From (3.6), we can derive the desired impedance to be approximated and implemented during the TOOL phase:

$$Z_d = \frac{Z_{th} - h_{11}}{h_{12}h_{21} + h_{22}(Z_{th} - h_{11})} \tag{3.23}$$

Thus, the therapist's identified impedance Z_{th} needs to be modulated as shown above to act as the desired impedance for the slave robot in the TOOL phase. In practice, we will use optimization techniques to approximate Z_d to be in the form of (3.9) for controller implementation.

3.5 Experimental Results

In this section we present the experimental results for our proof-of-concept LAR telerehabilitation session. We present the results in two subsections for the TIL phase and the TOOL phase respectively.

3.5.1 TIL Phase Results

As discussed in Section 3.2 and Section 3.3, we accomplish two main objectives in the TIL phase: teleoperation and identification of the therapist's arm impedance. In DFR teleoperation, we use a feedback gain $K_f = 0.5$ because of the following two reasons: 1) it provides the therapist with a good perception of the perturbations from the patient side; 2) the force feedback is not too strong for the therapist to handle with ease. A total of three TIL sessions were carried out, each lasting around $60\ s$ containing 20 to 26 perturbations. The experimental trials were carried out during the same day with one healthy person (the author of the thesis) acting as the therapist and another healthy person (the supervisory investigator) acting as the patient (see Appendix D and Appendix E). The arm

TABLE 3.1: Therapist arm impedance identification results

Session	M_{th} (kg)	B_{th} (N.s/m)	K_{th} (N/m)	$\frac{Nb_{pos}}{Nb_{tot}}$	T_w (ms)
1	1.48	60.87	1085.80	75%	420
2	1.70	52.48	1733.83	100%	530
3	2.61	53.23	1543.95	96%	860
Average	1.92	55.54	1454.52	90%	603

impedance identification results are presented in Table 3.1, including M_{th}, B_{th}, K_{th}, the percentage of all-positive identification results Nb_{pos} over the total number of considered perturbations in each session, and the chosen data window length T_w for model identification.

As can be seen from Table 3.1, with our impedance model identification approach, 90% of the perturbations yield all-positive identification results with an average data window length of about 600 ms. We use the averaged impedance parameters: $M_{th} = 1.92$ *kg*, $B_{th} = 55.54$ *N.s/m* and $K_{th} = 1454.52$ *N/m* to to make up the Z_{th} term in (3.23):

$$Z_{th} = M_{th} \cdot s + B_{th} + \frac{K_{th}}{s} \tag{3.24}$$

In addition, other parameters related to the robot dynamics and teleoperation controller are used to calculate the numerical value of Z_d in Equation 3.23. Their values are grouped together in Table 3.2. Note that the values for M_m, M_s and B_s are obtained using system identification method similar to what was done in [6]. L_m and L_s are obtained by directly measuring the concerned robot links. K_f, K_{pv} and K_{ps} are directly specified in the the controller software. Numerical calculation yields the following result:

$$Z_d = \frac{A \cdot s^4 + B \cdot s^3 + C \cdot s^2 + D \cdot s + E}{a \cdot s^3 + b \cdot s^2 + c \cdot s} \tag{3.25}$$

with $A = -0.0229$, $B = -15.220$, $C = -1096.453$, $D = -36346.370$, $E = -4.985 \cdot 10^5$, $a = 0.0226$, $b = -3.843$ and $c = -143.766$. However we cannot implement directly Equation 3.25 into the impedance controller in Equation 3.22 as it requires the impedance to be specified with M_d, B_d and K_d.

Ideally we would be able to rewrite Equation 3.25 into:

$$\frac{A \cdot s^4 + B \cdot s^3 + C \cdot s^2 + D \cdot s + E}{a \cdot s^3 + b \cdot s^2 + c \cdot s} = M_d \cdot s + B_d + \frac{K_d}{s} \tag{3.26}$$

TABLE 3.2: Teleoperation control and analysis parameters

Variable Name	Numerical Value
M_m $(kg.m^2)$	0.052
M_s $(kg.m^2)$	0.072
B_s $(N.m.s/rad)$	7.92
L_m (m)	0.267
L_s (m)	0.267
K_f	0.50
K_{pv} $(N.m/rad)$	1285.03
K_{ps} $(N.m/(rad/s))$	36.72

or equivalently

$$(A - M_d \cdot a)s^4 + (B - B_d \cdot a - M_d \cdot b)s^3$$
$$+ (C - B_d \cdot b - K_d \cdot a - M_d \cdot c)s^2$$
$$+ (D - B_d \cdot c - K_d \cdot b)s + (E - K_d \cdot c) = 0 \quad (3.27)$$

giving five equations to satisfy simultaneously:

$$Eq_1 \triangleq A - M_d \cdot a = 0$$
$$Eq_2 \triangleq B - B_d \cdot a - M_d \cdot b = 0$$
$$Eq_3 \triangleq C - B_d \cdot b - K_d \cdot a - M_d \cdot c = 0$$
$$Eq_4 \triangleq D - B_d \cdot c - K_d \cdot b = 0$$
$$Eq_5 \triangleq E - K_d \cdot c = 0 \quad (3.28)$$

In order to solve for the three variables from the 5 equation system that cannot be simultaneously satisfied, we adopt an optimization approach in which we we obtain the values for M_d, B_d and K_d by minimizing the following cost function over a certain value range for the three variables:

$$Cost = |Eq_1| + |Eq_2| + |Eq_3| + |Eq_4| + |Eq_5|, M_d \in [0, 10], B_d \in [0, 1000], K_d \in [0, 10000] \quad (3.29)$$

The minimization yields the following results $M_d = 3.89 \ kg$, $B_d = 160.14 \ N.s/m$ and $K_d = 3467.36 \ N/m$. The approximated impedance is compared to the original Z_d calculated in Equation 3.25 using Bode plot in Fig. 3.7. As can be seen from the plot, there is a good match between the original Z_d and the approximated impedance with M_d, B_d and K_d at low frequency range which is most relevant to the screwdriving task.

(a)

(b)
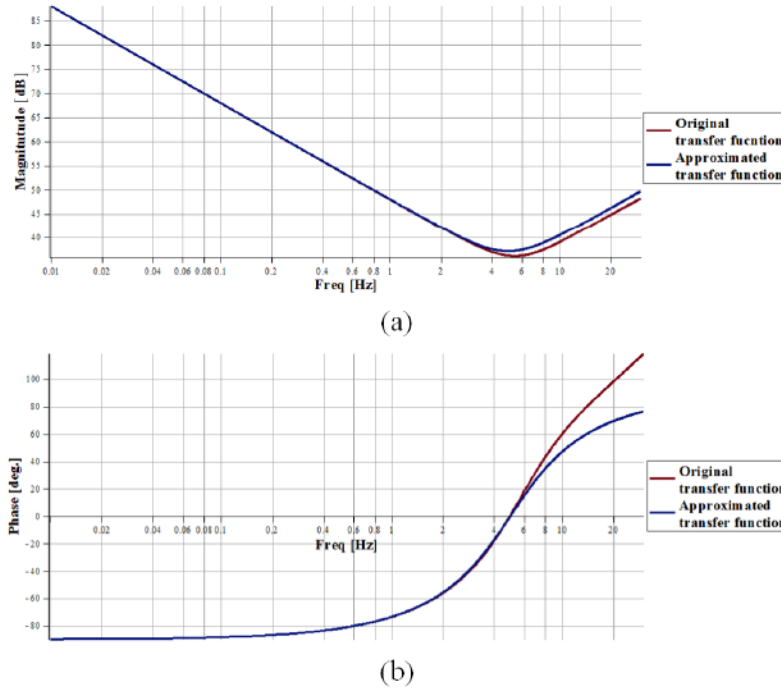
FIGURE 3.7: Comparison of the Bode plot between the original transfer function Z_d and the approximated transfer function $M_d s + B_d + K d/s$ used for implementation in both (a) magnitude, (b) phase at lower frequency of up to 30 Hz

.

3.5.2　TOOL Phase Results

In the TOOL phase, the slave robot is programmed under the impedance control law specified in (3.22) with the parameters of M_d, B_d and K_d found in TIL phase discussed in the previous subsection. $\bar{M}_s$ is selected to be 0.3 $kg.m^2$ by gradually increasing its value until the system starts to display instability. The patient (imitated by a healthy person) is then able to complete the screwdriving task with the slave robot alone in this phase. The impedance control implementation is validated by comparing the actual slave robot position against the simulated slave robot position based on the desired impedance and the measured interaction forces. The comparison result is plotted in Fig. 3.8 where a good match is shown. Note that the effect of the strong stiction inherent in our industrial manipulator arm is still visible but it is mitigated (position error no more than 0.2 mm during the task) thanks to the TDE approach. We can also see from Fig. 3.8 that the maximum displacement in the Y direction of the slave arm is around 15 mm, which is also the case in the TIL phase, showing that the desired behaviour has been successfully mapped from the therapist to the slave robot during the TOOL phase.
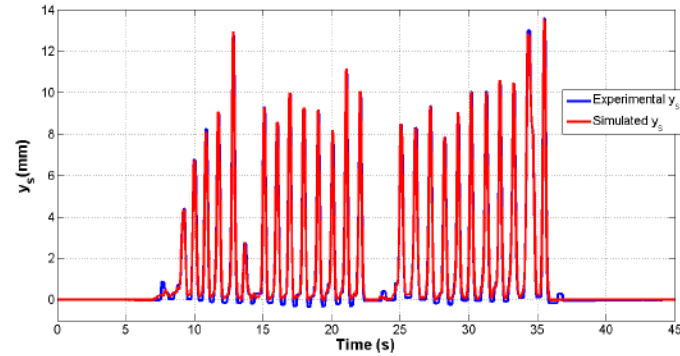
FIGURE 3.8: Comparison between simulated position based on force measurement and the actual position during TOOL phase

3.6   Conclusion

In this chapter, we demonstrated the proposed LAR telerehabilitation concept for a screwdriving task. During the TIL phase, the therapist supported the patient in completing the screwdriving task and simultaneously the impedance of his arm was measured by the master haptic device. The measured impedance was then processed taking into account the teleoperation system dynamics in order to obtain the desired impedance parameters used for impedance control implementation during the TOOL phase. In the TOOl phase, the impedance control was successfully implemented on the slave robot and the therapist's role in the screwdriving task was successfully replicated by the slave robot.

Chapter 4

Learn-and-Replay Telerehabilitation Paradigm: 2-DOF Task

In this chapter, we apply the Learn-and-replay (LAR) paradigm to a 2-DOF collaborative peg-in-the-hole task. The LAR paradigm essentially consists of two phases: a therapist-in-loop (TIL) phase and a therapist-out-of-loop (TOOL) phase. In the TIL phase the therapist interacts with the patient through the haptic teleoperation loop to perform one or more repetitions of a cooperative therapy task. During this phase we measure the therapist's arm impedance without interrupting the task execution. During the TOOL phase the therapist's cooperative role in completing the therapy task is played out by the patient-side robot. Following our implementation of the LAR principle on a 1-DOF screwdriving task, experimenting with more degrees of freedom is a necessary and natural next step in developing the LAR telerehabilitation paradigm. First, more DOFs are desirable from the system specification point view, as patients can exercise more complicated therapy tasks targeting different motor functions. Technically speaking, involving more DOFs also introduces interesting problems in terms of arm impedance identification, impedance distortion compensation and impedance control.

Similar to Chapter 3, we first give a description of the cooperative task in Section 4.1 and the teleoperation system used for performing it in Section 4.2. Then, the human arm impedance identification method adapted to the 2-DOF task is presented in Section 4.3. In Section 4.4, we present the Time-Delay Estimation TDE impedance control implementation for the slave robot in the generalized multi-DOF scenario. The results for arm impedance estimation during the TIL phase and the patient-robot impedance-based interactions during the therapist-out-of-loop (TOOL) phase are presented in Section 4.5.

4.1 Therapy Task

The 2-DOF task consists of the patient trying to put an aluminum mechanical part representing a 1-dimensional "hole" onto a peg held by the therapist as shown in Fig. 4.2(a). In the proposed LAR paradigm, the patient will insert the hole onto the peg attached to the end-effector of the slave robot shown in Fig. 4.2(b), which is teleoperated by the therapist from the master interface shown in Fig. 4.2(c). While "hole-onto-the-peg" insertion seems to be a more appropriate term to name the considered task, since the peg and the hole are play interchangeable roles, we still name the task "peg-in-the-hole" insertion. The peg-in-the-hole insertion task is a challenging manipulation task, involving both position and force control. In our case, the task requires the patient to first align the hole with the peg by wiggling it primarily in the Y direction, illustrated in Fig. 4.1(a). This is made possible by the curved opening of the hole as well as the curvature of the peg tip. This step is also shown in Fig. 4.2(a) in the direction manipulation case, where no robots are involved. Once the hole and the peg are lined up (illustrated in Fig. 4.1(b)), the patient pushes the hole onto the peg by exerting a force in the X direction (illustrated in Fig. 4.1). The X and Y Cartesian directions are defined for the slave robot in Fig. 4.2(b). Note that the X-Y frame origin is placed at the centre of the peg tool when the slave robot is at home position (detailed in Section 4.2), and it does not move with the peg tool. We name this frame the slave base frame. For the master robot, X and Y Cartesian directions are the same as the slave robot and the frame origin is attached to the handle when the master robot is at its home position. Although the master frame origin is also defined using the end-effector, it doesn't move with the handle either once it is defined. We name this X-Y frame related to the master robot the master base frame. Note that the master robot is not at its home position in Fig. 4.2(c). The master robot is at its home position when θ_{1m} and θ_{2m} shown in Fig. 4.2(c) are both zero. More details of these two joint angles will be given in Section 4.2, using axes parallel to the X and Y axis of the master robot but attached to the robot centre axis shown as X_0 and Y_0 in Fig. 4.2(c).

Similar to the 1-DOF task in Chapter 3, the therapist holds firmly the master haptic device in both X and Y directions while the patient tries to complete the task during the TIL phase. We make this choice because it is desirable for the patient to learn to behave compliantly. For the peg-in-the-hole task to be able to be completed, the both operators cannot be both compliant or both rigid at the same time (or else the hole risks not being able to be lined up with and inserted into the peg).

For the realization of this teleoperation system, readers can get more information in Appendix B, Appendix **??** and Appendix F.
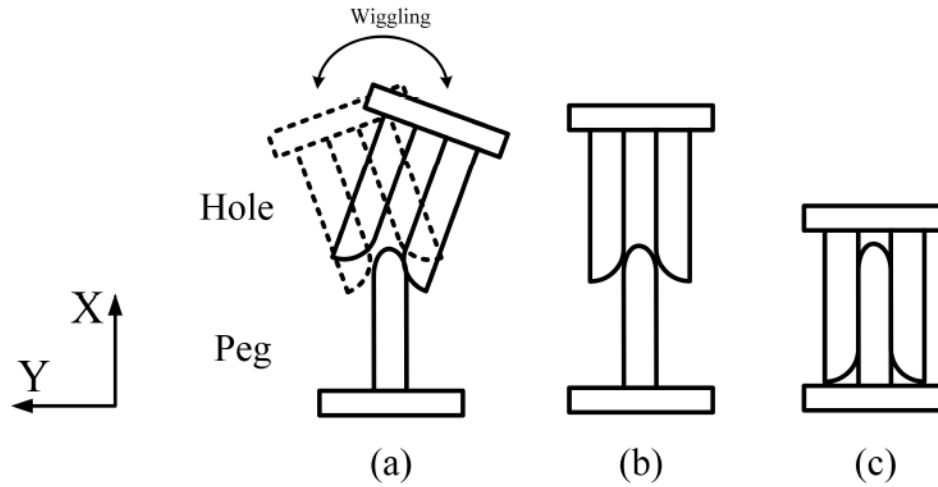
FIGURE 4.1: Illustration of the peg-in-the-hole task. (a) Wiggling of the hole in the Y direction. (b) Alignment in the of the peg and the hole. (c) The hole pushed onto the peg.

4.2 Teleoperation System

In this task, we face the difficulty of teleoperating two robots with different kinematics, workspaces and DOFs, because of our choice of the master and slave robots. We solve this problem by making the robot with more DOFs and a larger workspace have a similar effective geometry as the robot with fewer DOFs and a smaller workspace. To do so, we make the 7-DOF slave robot take on an effective 2-DOF geometry. The 1st, 4th and 6th joints of the slave robot are arranged according to inverse kinematics such that the distance between the 1st joint axis and the 6th joint axis, which is L_{1s} in Fig. 4.2(b), takes on a desired value and becomes the length of the 1st "effective link" of the slave robot. The detailed kinematics of the Motoman SIA5F robot and the inverse kinematics used for jogging the slave robot into its home position can be found in Appendix A

During teleoperation, high gain PID control is applied to joints 2 to 5 of the slave robot in order to maintain this geometry. The 2nd "effective link" of the slave robot is the same as the actuated link presented in Chapter 3 (comprising of the last link of the slave robot, the force sensor and peg tool) with link length L_{2s} (named L_s in Chapter 3) as shown in Fig. 4.2(b). For the master robot, both robot joints are actuated and the link lengths are L_{1m} and L_{2m} respectively, as shown in Fig. 4.2(c). Note that L_{2m} is the same as L_m in Chapter 3 for the 1-DOF task. We define that at home position, the 1st effective link and the 2nd effective link of the slave robot are perpendicular to each other (shown in Fig. 4.2(b)), while the 2nd effective link points to the positive X direction. The same can be said about the master robot: at home position, the 1st link and the 2nd link are perpendicular to one another, while the 2nd link points to the positive X direction.
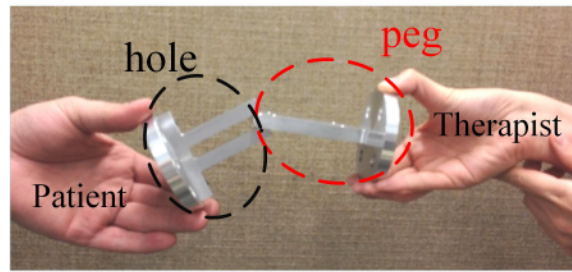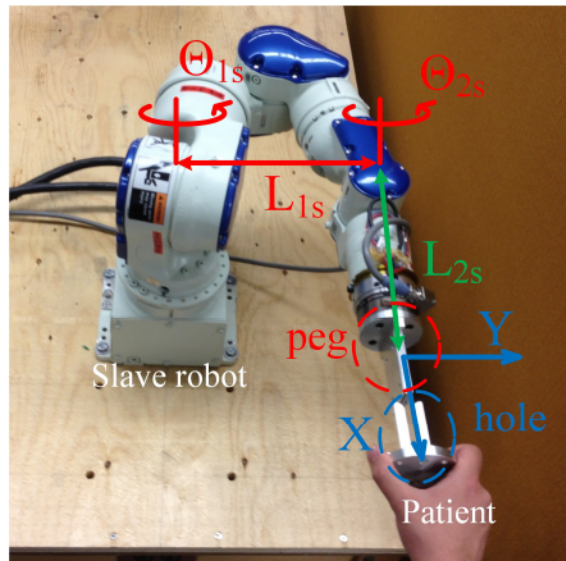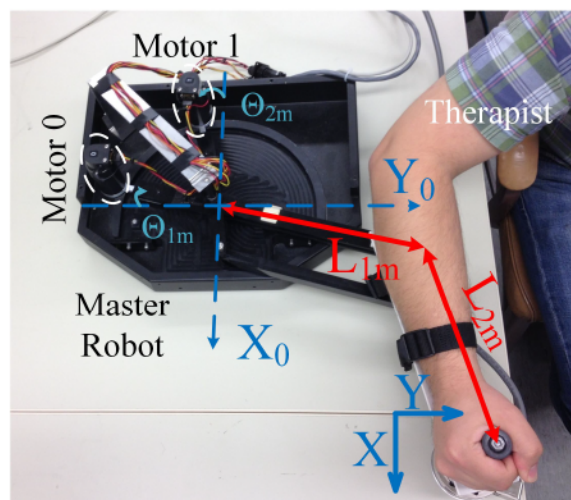
FIGURE 4.2: (a) Direct manipulation: The peg-in-the-hole task without using any robots. (b) Configuration of the slave (patient-side) Yaskawa Motoman SIA5F robot as the slave. (c) Configuration of the master (therapist-side) rehabilitation robot for as the master.
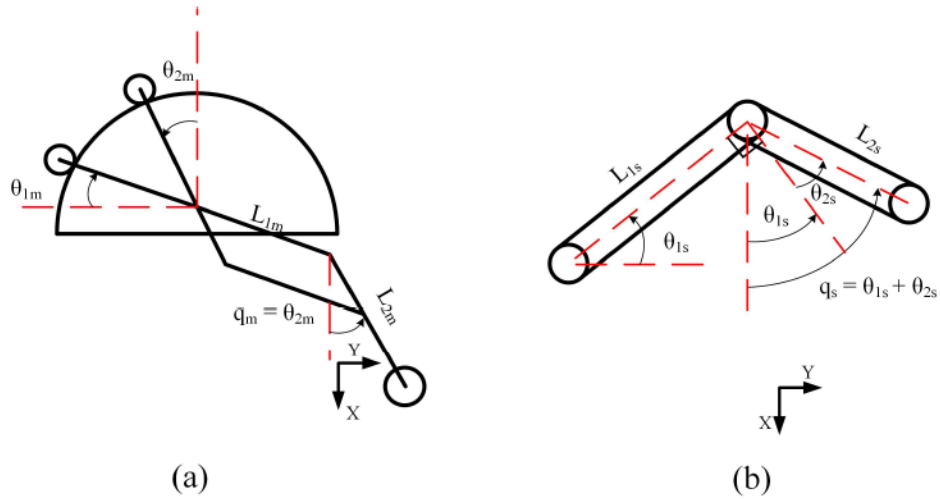
FIGURE 4.3: Illustration of (a) the master robot and (b) the slave robot joint angle configurations.

In terms of joint angles, we use the 1st and 6th joint angle of the slave robot minus their values when the slave robot is at its home position as the new joint angles: θ_{1s} and θ_{2s}. Therefore, at the home position shown in Fig. 4.2(b), $\theta_{1s} = \theta_{2s} = 0$. For the master robot, we define the 1st joint angle to be the angle formed by rotating the Y_0 axis counterclockwise around the robot centre joint to be parallel to the 1st robot link (L_{1m}), and the 2nd joint angle to be the angle formed by rotating the X_0 axis counterclockwise to be parallel to the 2nd robot link (L_{2m}). Note that in the configuration presented in Fig. 4.2(c), θ_{1m} has a negative value while θ_{2m} has a positive value. The joint angle configurations for the master and the slave are illustrated in Fig. 4.3.

We made $L_{1s} = L_{1m} = 0.254m$, using the joint angle values detailed in Table A.3 in Appendix A. As we saw in the last chapter, $L_{2s} = L_{2m} = 0.2667m$. Therefore, we have made the master and slave robots have similar effective geometries. During teleoperation, we simply make the slave robot follow the master robot by using the current values of θ_{1m} and $\theta_{2m} - \theta_{1m}$ as the reference positions for θ_{1s} and θ_{2s}. This can be seen from from Fig. 4.3, by defining the angles between the X-axis and the second link of both robots (L_{2m} and L_{2s}) as q_m and q_s respectively. Since q_m and q_s should be equal to each other, we have

$$q_m = \theta_{2m} = q_s = \theta_{1s} + \theta_{2s} \tag{4.1}$$

Therefore,

$$\theta_{2m} = \theta_{1s} + \theta_{2s} \tag{4.2}$$

$$\theta_{2s} = \theta_{2m} - \theta_{1s} \tag{4.3}$$

Since θ_{1s} takes θ_{1m} as its reference, we can replace θ_{1s} in (4.3) by θ_{2s} and obtain

$$\theta_{2s} = \theta_{2m} - \theta_{1m} \tag{4.4}$$

as the reference angle position for θ_{2s}.

4.2.1   Master and Slave Robots Kinematics

In this subsection we consider the forward kinematics for the master and slave robots.

The kinematic position and velocity mappings between the joint space and the Cartesian space for the master robot are

$$
\begin{aligned}
\mathbf{p_m} &= \begin{bmatrix} x_m \\ y_m \end{bmatrix} \\
&= \begin{bmatrix} -L_{1m} \cdot sin(\theta_{1m}) + L_{2m} \cdot cos(\theta_{2m}) - L_{2m} \\ L_{1m} \cdot cos(\theta_{1m}) + L_{2m} \cdot sin(\theta_{2m}) - L_{1m} \end{bmatrix}
\end{aligned} \tag{4.5}
$$

$$
\begin{aligned}
\dot{\mathbf{p}}_\mathbf{m} &= \begin{bmatrix} \dot{x}_m \\ \dot{y}_m \end{bmatrix} = \mathbf{J_m} \cdot \dot{\boldsymbol{\theta}}_\mathbf{m} \\
&= \begin{bmatrix} -L_{1m} \cdot cos(\theta_{1m}) & -L_{2m} \cdot sin(\theta_{2m}) \\ -L_{1m} \cdot sin(\theta_{1m}) & L_{2m} \cdot cos(\theta_{2m}) \end{bmatrix} \cdot \begin{bmatrix} \dot{\theta}_{1m} \\ \dot{\theta}_{2m} \end{bmatrix}
\end{aligned} \tag{4.6}
$$

where the vector $\mathbf{p_m}$ is used to denote the master robot end-point (corresponding to the handle that the therapist holds) position in the X-Y master base frame, $\mathbf{J_m}$ denotes the master robot's Jacobian matrix and $\dot{\boldsymbol{\theta}}_\mathbf{m}$ denotes the master robot joint angular velocity vector.

Similarly for the slave robot (constrained to 2-DOF motion as explained before), we have

$$
\begin{aligned}
\mathbf{p_s} &= \begin{bmatrix} x_s \\ y_s \end{bmatrix} \\
&= \begin{bmatrix} -L_{1s} \cdot sin(\theta_{1s}) + L_{2s} \cdot cos(\theta_{1s} + \theta_{2s}) - L_{2s} \\ L_{1s} \cdot cos(\theta_{1s}) + L_{2s} \cdot sin(\theta_{1s} + \theta_{2s}) - L_{1s} \end{bmatrix}
\end{aligned} \tag{4.7}
$$

$$
\begin{aligned}
\dot{\mathbf{p}}_\mathbf{s} &= \begin{bmatrix} \dot{x}_s \\ \dot{y}_s \end{bmatrix} = \mathbf{J_s} \cdot \dot{\boldsymbol{\theta}}_\mathbf{s} \\
&= \begin{bmatrix} -L_{1s} \cdot cos(\theta_{1s}) - L_{2s} \cdot sin(\theta_{1s} + \theta_{2s}) & -L_{2s} \cdot sin(\theta_{1s} + \theta_{2s}) \\ -L_{1s} \cdot sin(\theta_{1s}) + L_{2s} \cdot cos(\theta_{1s} + \theta_{2s}) & L_{2s} \cdot cos(\theta_{1s} + \theta_{2s}) \end{bmatrix} \cdot \begin{bmatrix} \dot{\theta}_{1s} \\ \dot{\theta}_{2s} \end{bmatrix}
\end{aligned} \tag{4.8}
$$

where the vector $\mathbf{p_s}$ is used to denote the slave robot end-point (corresponding to the centre of the peg) position in the X-Y slave base frame, $\mathbf{J_s}$ denotes the slave robot's Jacobian matrix and $\dot{\boldsymbol{\theta}}_s$ denotes the slave robot joint angular velocity vector.

Joint torques applied by the motors are denoted by $\boldsymbol{\tau_m} = [\tau_{1m} \ \tau_{2m}]^T$ for the master robot and $\boldsymbol{\tau_s} = [\tau_{1s} \ \tau_{2s}]^T$ for the slave robot. We can therefore relate static joint torques to the end-effector Cartesian forces, $\mathbf{f_m} = [f_{x_m} \ f_{y_m}]^T$ for the master robot and $\mathbf{f_s} = [f_{x_s} \ f_{y_s}]^T$ for the slave robot, by

$$\boldsymbol{\tau_m} = \mathbf{J_m^T} \cdot \mathbf{f_m} \tag{4.9}$$

$$\boldsymbol{\tau_s} = \mathbf{J_s^T} \cdot \mathbf{f_s} \tag{4.10}$$

Similarly, Cartesian forces applied by human operators onto the robots, $\mathbf{f_{th}} = [f_{x_{th}} \ f_{y_{th}}]^T$ for the forces applied to the master robot by the therapist and $\mathbf{f_p} = [f_{xp} \ f_{yp}]^T$ for the forces applied to the slave robot by the patient, can be mapped to their corresponding joint torques $\boldsymbol{\tau_{th}} = [\tau_{1th} \ \tau_{2th}]^T$ and $\boldsymbol{\tau_p} = [\tau_{1p} \ \tau_{2p}]^T$ by

$$\boldsymbol{\tau_{th}} = \mathbf{J_m^T} \cdot \mathbf{f_{th}} \tag{4.11}$$

$$\boldsymbol{\tau_p} = \mathbf{J_s^T} \cdot \mathbf{f_p} \tag{4.12}$$

4.2.2 Master and Slave Robot Dynamics

In this subsection we consider the dynamics for the master and slave robots.

The master robot dynamics can be modeled by

$$\mathbf{M_m}(\boldsymbol{\theta_m}) \cdot \ddot{\boldsymbol{\theta}}_m + \mathbf{C_m}(\boldsymbol{\theta_m}, \dot{\boldsymbol{\theta}}_m) \cdot \dot{\boldsymbol{\theta}}_m + \mathbf{f_{rm}}(\boldsymbol{\theta_m}, \dot{\boldsymbol{\theta}}_m) - \boldsymbol{\tau_{th}} = \boldsymbol{\tau_m} \tag{4.13}$$

where $\mathbf{C_m}$ denotes the Coriolis and centrifugal matrix and $\mathbf{f_{rm}}$ denotes the joints friction vector. According to [58], the master robot dynamics can be obtained by identifying the five parameters

$\alpha_1, \ldots, \alpha_5$ that parameterize the dynamics if only viscous friction is considered:

$$\mathbf{M_m}(\boldsymbol{\theta_m}) = \begin{bmatrix} \alpha_1 & -\frac{1}{2} \cdot \alpha_2 sin(\theta_{1m} - \theta_{2m}) \\ -\frac{1}{2} \cdot \alpha_2 sin(\theta_{1m} - \theta_{2m}) & \alpha_3 \end{bmatrix} \tag{4.14}$$

$$\mathbf{C_m}(\boldsymbol{\theta_m}, \dot{\boldsymbol{\theta}}_m) = \begin{bmatrix} 0 & \frac{1}{2} \cdot \alpha_2 cos(\theta_{1m} - \theta_{2m})\dot{\theta}_{2m} \\ \frac{1}{2} \cdot \alpha_2 cos(\theta_{1m} - \theta_{2m})\dot{\theta}_{1m} & 0 \end{bmatrix} \tag{4.15}$$

$$\mathbf{f_{rm}}(\dot{\boldsymbol{\theta}}_m) = \begin{bmatrix} \alpha_4 \cdot \dot{\theta}_{1m} \\ \alpha_5 \cdot \dot{\theta}_{2m} \end{bmatrix} \tag{4.16}$$

We can obtain the values for $\alpha_1, \ldots, \alpha_5$ by system identification.

The slave robot dynamics can be modeled by

$$\mathbf{M_s}(\boldsymbol{\theta_s}) \cdot \ddot{\boldsymbol{\theta}}_s + \mathbf{C_s}(\boldsymbol{\theta_s}, \dot{\boldsymbol{\theta}}_s) \cdot \dot{\boldsymbol{\theta}}_s + \mathbf{f_{rs}}(\boldsymbol{\theta_s}, \dot{\boldsymbol{\theta}}_s) - \boldsymbol{\tau_p} = \boldsymbol{\tau_s} \tag{4.17}$$

where $\mathbf{C_s}$ denotes the slave robot's Coriolis and centrifugal matrix and $\mathbf{f_{rs}}$ denotes the joints friction vector. We will obtain the numerical values of the slave dynamic model parameters by calculation based on the geometric and mechanical properties of the slave robot

4.2.3   Telerehabilitation System Controller

The same DFR teleoperation control architecture used in Chapter 3 is adopted for the 2-DOF peg-in-the-hole task: the master robot provides position reference for the slave robot while the interaction forces captured by the force sensor attached to the slave end-effector are displayed via the master robot. The control system schematic is presented in Fig.4.4. Note that uppercase letters are used to denote the Laplace transforms of the corresponding time-domain position, velocity, force and torque variables.

The matrix $\mathbf{Q}$ is introduced to transform the maser robot joint angles into reference joint angles for the corresponding slave joints (according to the relationships $\theta_{1m} \rightarrow \theta_{1s}$ and $\theta_{2m} - \theta_{1m} \rightarrow \theta_{2s}$:

$$\mathbf{Q} = \begin{bmatrix} 1 & 0 \\ -1 & 1 \end{bmatrix} \tag{4.18}$$

$\mathbf{K_s}$ refers the PD position controller for the slave robot:

$$\mathbf{K_s} = \begin{bmatrix} K_{v1} + \dfrac{K_{p1}}{s} & 0 \\ 0 & K_{v2} + \dfrac{K_{p2}}{s} \end{bmatrix} \tag{4.19}$$

Note that the inputs to the controller matrix $\mathbf{K_s}$ are velocities, not positions, as shown later in (4.26). This is the reason why it might look like an PI controller but it is actually a PD controller.

$\mathbf{K_f}$ refers to the force feedback gain matrix for the master robot:

$$\mathbf{K_f} = \begin{bmatrix} K_{f1} & 0 \\ 0 & K_{f2} \end{bmatrix} \tag{4.20}$$

$\mathbf{Z_m}$ and $\mathbf{Z_s}$ denote the linear impedance matrices in the joint domain of the master and slave robot that we approximate from the nonlinear robot dynamics as we will detail later in Section 4.5. $\mathbf{Z_{th}}$ and $\mathbf{Z_s}$ refer to the impedance matrices in the Cartesian domain of the therapist's arm and the patient's arm respectively. As can be seen in Fig. 4.4, the teleoperation system is divided into five subsystems: therapist, master robot, control & communication, slave robot and patient. For the therapist and patient, we have

$$\mathbf{F_{th}} = \mathbf{F_t^* h} - \mathbf{Z_{th}} \cdot \mathbf{\dot{P}_m} \tag{4.21}$$

$$\mathbf{F_p} = \mathbf{F_p^*} - \mathbf{Z_p} \cdot \mathbf{\dot{P}_p} \tag{4.22}$$

where F_{th}^* and F_p^* denote the therapist's and patient's exogenous input forces (generated by the muscles with command sent from the central nervous system). For the master robot and the slave robot we have

$$\mathbf{T_{th}} + \mathbf{T_m} = \mathbf{Z_m} \cdot \mathbf{\dot{\Theta}_m} \tag{4.23}$$

$$\mathbf{T_p} + \mathbf{T_s} = \mathbf{Z_m} \cdot \mathbf{\dot{\Theta}_s} \tag{4.24}$$

As the therapist and patient work in Cartesian space but the robots work in joint spaces, Jacobian matrices are needed as interfaces between the therapist and master robot, as well as between the patient and the slave robot, to convert Cartesian forces to joint domain torques (based on (4.11) and (4.12)) and to convert joint velocities to Cartesian velocities (based on (4.6) and (4.8)). As for the controller, we have

$$\mathbf{T_m} = \mathbf{J_m^T K_f} \cdot \mathbf{F_p} \tag{4.25}$$
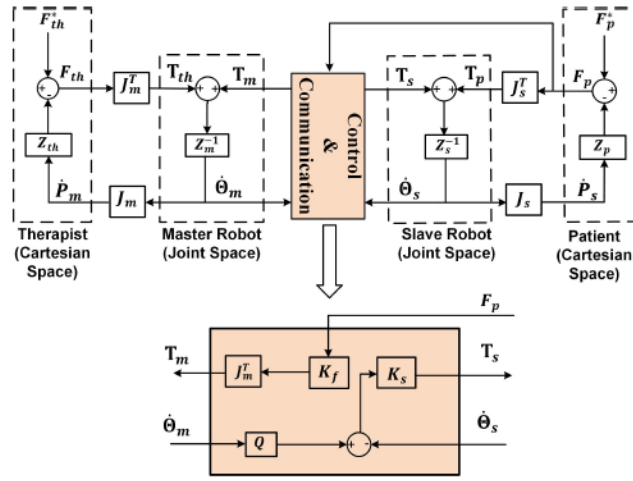
FIGURE 4.4: Schematic of the teleoperation control architecture

for the force feedback control on the master robot, and

$$\mathbf{T_s} = \mathbf{K_s} \cdot (\mathbf{Q} \cdot \dot{\mathbf{\Theta}}_\mathbf{m} - \dot{\mathbf{\Theta}}_\mathbf{s}) \tag{4.26}$$

for the slave robot's position control.

By combining (4.23), (4.24), (4.25) and (4.26), the overall system dynamics in the frequency domain can be derived:

$$\mathbf{J_m} \cdot \mathbf{Z_m^{-1}} \cdot \mathbf{J_m^T}(\mathbf{F_{th}} + \mathbf{K_f} \cdot \mathbf{F_p}) = \dot{\mathbf{P}}_\mathbf{m} \tag{4.27}$$

$$\mathbf{J_s} \cdot \mathbf{Z_s^{-1}} \cdot (\mathbf{J_s^T} \cdot \mathbf{F_p} + \mathbf{K_s} \cdot (\mathbf{Q} \cdot \mathbf{J_m^{-1}} \cdot \dot{\mathbf{P}}_\mathbf{m} - \mathbf{J_s^{-1}} \cdot \dot{\mathbf{P}}_\mathbf{s})) = \dot{\mathbf{P}}_\mathbf{s} \tag{4.28}$$

Equations (4.27) and (4.28) can be manipulated into the following 2-port network hybrid matrix form

$$\begin{bmatrix} \mathbf{F_{th}} \\ -\dot{\mathbf{P}}_\mathbf{s} \end{bmatrix} = \begin{bmatrix} \mathbf{H_{11}} & \mathbf{H_{12}} \\ \mathbf{H_{21}} & \mathbf{H_{22}} \end{bmatrix} \begin{bmatrix} \dot{\mathbf{P}}_\mathbf{m} \\ \mathbf{F_p} \end{bmatrix} \tag{4.29}$$

where

$$\mathbf{H_{11}} = \mathbf{J_m^{-T}} \cdot \mathbf{Z_m} \cdot \mathbf{J_m^{-1}} \tag{4.30}$$

$$\mathbf{H_{12}} = -\mathbf{K_f} \tag{4.31}$$

$$\mathbf{H_{21}} = -(\mathbf{J_s} \cdot \mathbf{Z_s^{-1}} \cdot \mathbf{K_s} \cdot \mathbf{J_s^{-1}} + \mathbf{I_{2 \times 2}})^{-1} \cdot \mathbf{J_s} \cdot \mathbf{Z_s^{-1}} \cdot \mathbf{K_s} \cdot \mathbf{Q} \cdot \mathbf{J_m^{-1}} \tag{4.32}$$

$$\mathbf{H_{22}} = -(\mathbf{J_s} \cdot \mathbf{Z_s^{-1}} \cdot \mathbf{K_s} \cdot \mathbf{J_s^{-1}} + \mathbf{I_{2 \times 2}})^{-1} \cdot \mathbf{J_s} \cdot \mathbf{Z_s^{-1}} \cdot \mathbf{J_s^T} \tag{4.33}$$

and $\mathbf{I}_{2\times 2}$ is the 2-by-2 identity matrix. The 2-port network hybrid matrix will be used later in Section to help derive the desired impedance matrices for the impedance controller.

4.3 Identification of Human Arm Impedance

This section is an extension of the human arm impedance identification strategy used in Chapter 3 to the 2-DOF scenario. We use the initial wiggling forces in the Y direction for the peg and hole alignment and the subsequent pushing forces along the X direction once the peg and the hole are aligned as excitation inputs needed for human arm impedance identification. Again, a zero position is defined for the task as $x_m = 0.04\ m$ and $y_m = 0$, or equivalently $\theta_{1m} = -9°$ and $\theta_{2m} = 0°$. The zero position is displayed to the therapist via a computer monitor. It is desirable for the therapist's arm to return to the same position after each force perturbation. The X-coordinate of the zero position on the is non-zero because some initial distance is needed as buffer between the first master robot link and the robot frame, so that the disturbances along the X-axis will not lead to the robot link hitting the robot frame.

We consider the energy absorbed by the therapist's arm in both the X and Y directions over the timespan T:

$$E_x = \int_0^T -f_{x_{th}}(t)\dot{x}_m(t)\,\mathrm{d}t \tag{4.34}$$

$$E_y = \int_0^T -f_{y_{th}}(t)\dot{y}_m(t)\,\mathrm{d}t \tag{4.35}$$

Similar to the 1-DOF task, over a number of peg-in-the-hole insertion repetitions, the absorbed energy as shown in Fig.4.5 rises when the perturbation starts either in the X or the Y direction. Therefore, a force perturbation onset in the X or Y direction is determined as the moment when $\dot{E}_x$ or $\dot{E}_y$ becomes positive.

Different from the 1-DOF case, in which the screwdriving task involves a series of perturbations, the peg-in-the-hole insertion task involves considerably less perturbation forces being fed back to the therapist. Therefore, we have to use a series of repetitions of the peg-in-the-hole insertion task to identify the arm impedance of the therapist, and we consider that each peg-in-hole task is comprised of one perturbation in the X direction and one perturbation in the Y direction. Although in reality the wiggling in the Y direction may be comprised of a number of lateral force peaks and so are the X direction pushing forces, we only consider the first couple of hundred data points for model consistency and passivity reasons. As discussed in Chapter 3 Section 3.3, the human cannot react
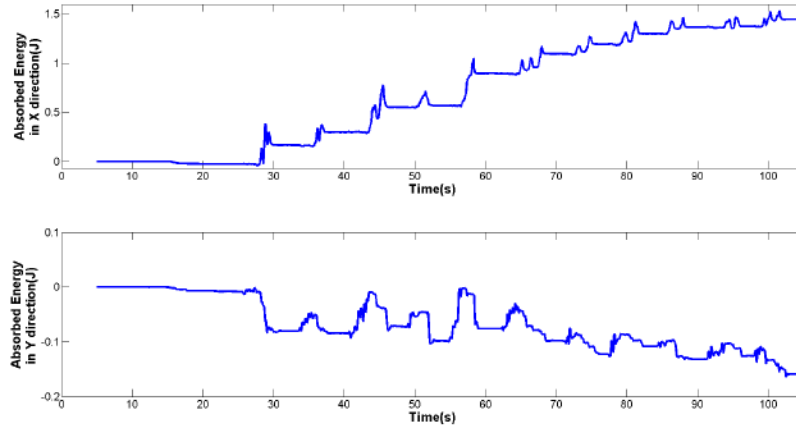
FIGURE 4.5: Absorbed mechanical energy in the X direction (top) and the Y direction (bottom) over repeated peg-in-the-hole insertions
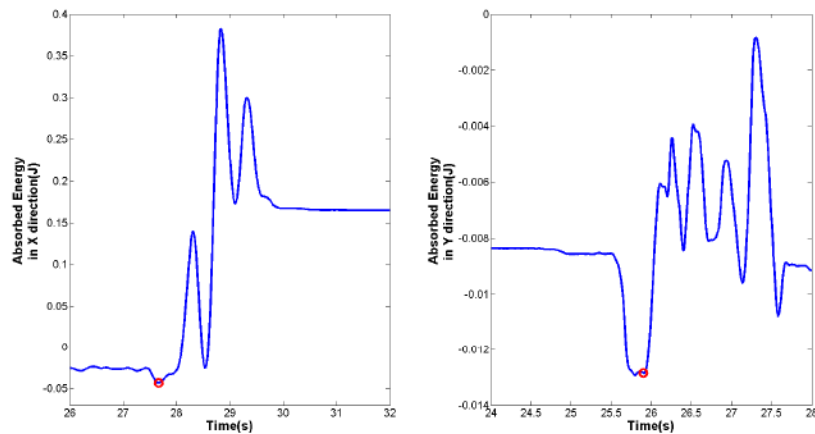
FIGURE 4.6: Absorbed mechanical energy in the X direction (left) and the Y direction (right) during the initial period of the peg-in-the-hole insertion with the estimated perturbation onset circled in red

voluntarily to the abrupt motion (thus remains passive) during the first 100~150 ms window [53] and ideally we would like to use a data window length within this range for the arm impedance model identification. At the same time, arm impedance model identification does not necessarily yield consistent results with the number of data points available in the 100~150 ms window length. Thus the compromise between the above two concerns prompt us to relax the permissible window length to the first couple hundred data points and the determination of the actual data window length will be given shortly after in this section. The energy plot of a peg-in-the-hole insertion is shown in Fig. 4.6 and the force plot of the same task is shown in Fig. 4.7.
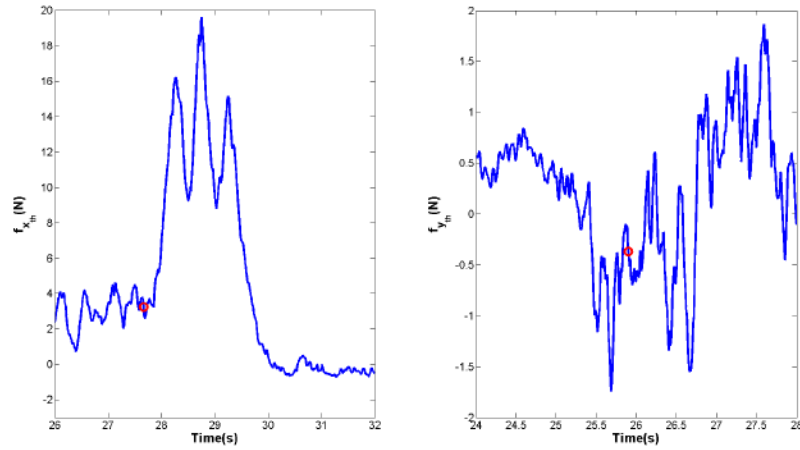
FIGURE 4.7: Force profile of $f_{x_{th}}$ (left) and $f_{y_{th}}$ (right) during the initial period of the peg-in-the-hole insertion with the estimated perturbation onset from absorbed energy data circled in red

We can see from Fig. 4.7 that wiggling force profile in the Y direction can be quite noisy, therefore giving reason to our use of the more smooth energy-based criterion for detecting the onset of perturbation. Note that the perturbation in the X direction occurs later than the perturbation in the Y direction because the wiggling in the Y direction occurs first.

In the X direction, the overall human arm behaviour is passive as the energy absorbed during each perturbation is seen to be positive in Fig. 4.5, while the human arm behaviour in the Y direction is active since the energy ends up being negative after this series of peg-in-the-hole insertion tasks. This is consistent with the findings in [6] as forces applied in the X direction have a bigger amplitude than those in the Y direction (shown in Fig. 4.7). In [6], the human arm impedance was measured precisely using the same Quanser rehabilitation robot when the test subject was asked to grab the handle rigidly, while the robot applied undernamed perturbations. It was found that when the steady-state amplitude of the force perturbation was increased from 2N to 8N, the arm demonstrated overall passivity as opposed to the overall active behaviour in the 2N case. This was because for a higher amplitude force perturbation, the energy initially absorbed by the hand was larger than the energy generated when the subject returned his hand to the target position. For a smaller amplitude force perturbation, the hand was perturbed with less force, resulting in a slower velocity compared to the 8N case as the hand was "knocked away". Therefore the energy absorbed at the application of the force perturbation was less than the energy generated during the return movement. The same phenomenon is reproduced here.

Although the overall behaviour of the human arm in the Y direction may be active, we will use the data immediately after the perturbation is applied in order to capture the passive behaviour of

the human arm before the CNS is activated [7]. This is because we desire to obtain the passive impedance of the human arm, as later during the TOOL phase, implementing an active impedance may endanger the patient's safety. Data points up to 1s will be used for human arm impedance identification, as was done in Chapter 3. The upper bound is chosen to be 1s as a compromise between the need for a longer window length for impedance model identification and a shorter window for passivity concerns.

In summary for each perturbation (whether in the X direction or the Y direction), we will define a time t_p signifying the starting moment of this perturbation by analyzing the absorbed energy. A complete 2-DOF Cartesian arm impedance model identified using force and position data collected over the time window $[t_p,\ t_w]$ can be written as

$$\mathbf{M} \cdot \ddot{\mathbf{p}}(t) + \mathbf{B} \cdot \dot{\mathbf{p}}(t) + \mathbf{K} \cdot \mathbf{p}(t) = -\mathbf{f}(t),\ t \in [t_p,\ t_w] \tag{4.36}$$

where $\mathbf{p}(t) = \mathbf{p_{th}}(t) - \mathbf{p_{th}}(t_p)$ and $\mathbf{f}(t) = \mathbf{f_{th}}(t) - \mathbf{f_{th}}(t_p)$ in order to consider only the therapist arm's position/velocity/acceleration and force *changes* caused by the force disturbance.

The matrices $\mathbf{M}$, $\mathbf{B}$ and $\mathbf{K}$ can be written as

$$\mathbf{M} = \begin{bmatrix} m_{xx} & m_{xy} \\ m_{yx} & m_{yy} \end{bmatrix},\ \mathbf{B} = \begin{bmatrix} b_{xx} & b_{xy} \\ b_{yx} & b_{yy} \end{bmatrix},\ \mathbf{K} = \begin{bmatrix} k_{xx} & k_{xy} \\ k_{yx} & k_{yy} \end{bmatrix} \tag{4.37}$$

As a result, if such a complete coupled 2-DOF impedance model is to be used, there are 12 parameters to be identified given less than 1s of data (1000 data points since for our system, the control and data recording operate at 1kHz) via linear least-squares regression, which is difficult. Therefore, we have decided to simplify the problem by adopting the approach used in [7] in which decoupled models are used. To this end, we adopt a decoupled model of the impedance matrix by modifying the $\mathbf{M}$, $\mathbf{B}$ and $\mathbf{K}$ in (4.37) to

$$\mathbf{M} = \begin{bmatrix} m_{xx} & 0 \\ 0 & m_{yy} \end{bmatrix},\ \mathbf{B} = \begin{bmatrix} b_{xx} & 0 \\ 0 & b_{yy} \end{bmatrix},\ \mathbf{K} = \begin{bmatrix} k_{xx} & 0 \\ 0 & k_{yy} \end{bmatrix} \tag{4.38}$$

We separate the perturbations into X-direction perturbations and Y-direction perturbations. Then, we use the X-direction perturbation data $(f_{x_{th}}, x_m, \dot{x}_m, \ddot{x}_m)$ to identify m_{xx}, b_{xx} and k_{xx}, and the Y-direction perturbation data $(f_{y_{th}}, y_m, \dot{y}_m, \ddot{y}_m)$ to identify m_{yy}, b_{yy} and k_{yy}. In this way, the 2-DOF arm impedance model identification is transformed into two 1-DOF arm impedance model identification exercises.

We use the same linear least-squares regression model identification technique as in Chapter 3. First, the force and position signals from the entire series of peg-in-the-hole insertion tasks are filtered with a Savitzky-Golay filter or order 6 and window size of 101 sample points. Next the data are again filtered with a Butterworth low-pass filter of order 5 and 5 Hz cut-off frequency. Again this cut-off frequency was chosen because spectral analysis on the measured signals show that the frequency content above 5 Hz can be negligible. The other filtering parameters were chosen in Chapter 3 so that the identification method provided the best results in identifying the now impedance parameters of a mass-spring system. Then, velocity and acceleration data are obtained by applying central differencing to the filtered position data. Finally, linear-squares regression model identification is applied to each X-direction perturbation data chunk and each Y-direction perturbation data chunk, defined by a t_p and t_w pair, determined as described below.

In order to determine the data window length $T_w = t_w - t_p$, the same approach utilized in Chapter 3 is applied. The algorithm presented in Fig. 3.5 is applied to a grid of window length candidates $T_w \in [100ms, 1000ms]$ at 10 ms steps for perturbations in the X and Y directions, respectively. The process aims at minimizing the window length T_w while achieving a maximum number of positive identified impedance parameters and guaranteeing a high enough average VAF value (at least 95%) over the series of peg-in-the-hole insertion tasks under consideration. The identification results for the series of peg-in-the-hole insertion tasks considered in the X direction as a function of T_w is shown in Fig. 4.8 while the results in Y direction are shown in Fig. 4.9.

As it can be seen from Fig. 4.8(a) in the X direction, the number of all-positive impedance identification results (m_{xx}, b_{xx} and k_{xx} are all positive) increases with the length of the data window until reaching 10 out of the 11 total perturbations, which is similar to the 1-DOF case presented in Fig. 3.6 in Chapter 3. From Fig. 4.9(a), in the Y direction after the initial increase, the number of all-positive impedance identification results (m_{yy}, b_{yy} and k_{yy} are all positive) decreases rapidly with T_w. The maximum all-positive impedance results count is also smaller (7 over 11) compared to the X direction results (10 over 11). This shows that the arm becomes quickly active in the Y direction and therefore the passive impedance model for the arm no longer works. The VAF values also point to the same observation: While VAF for the X direction decreases slowly with the increase of T_w and eventually drops to around 97, the VAF value for the Y direction decreases much rapidly as more data points are taken into consideration, indicating arm activity. This is due to the much larger amplitude of force perturbations in the X direction compared to the amplitude of force perturbations in the Y direction (see Fig. 4.7). This confirms the findings of [6], as discussed earlier in this section. The above observation further gives sense to our combined approach of minimizing T_w while maximizing the number of all-positive impedance results and taking the VAF into account, because while the increase in T_w may increase the all-positive impedance results count up to a certain T_w, it
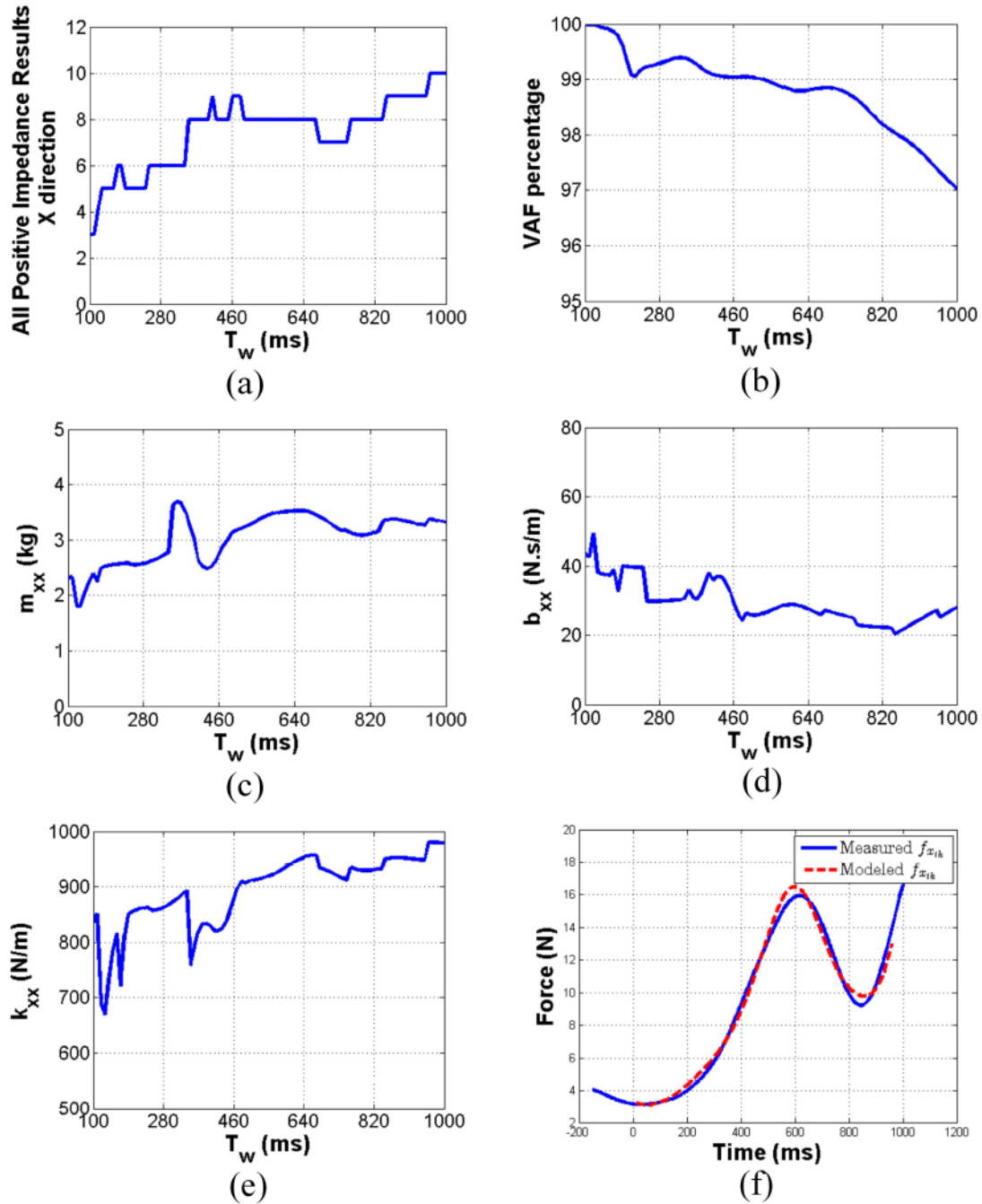
FIGURE 4.8: Impedance identification results as a function of data window lengths T_w for a series of peg-in-the-hole insertion tasks in the X direction: (a) the number of all-positive impedance identification results, (b) average VAF value in percentage of all-positive impedance identification results; (c) average m_{xx}, (d) average b_{xx}, (e) average k_{xx} of all-positive impedance identification results, (f) impedance model validation with modeled $f_{x_{th}}$ compared to measured $f_{x_{th}}$ for one perturbation with the determined window size at 960 ms and VAF value at 99
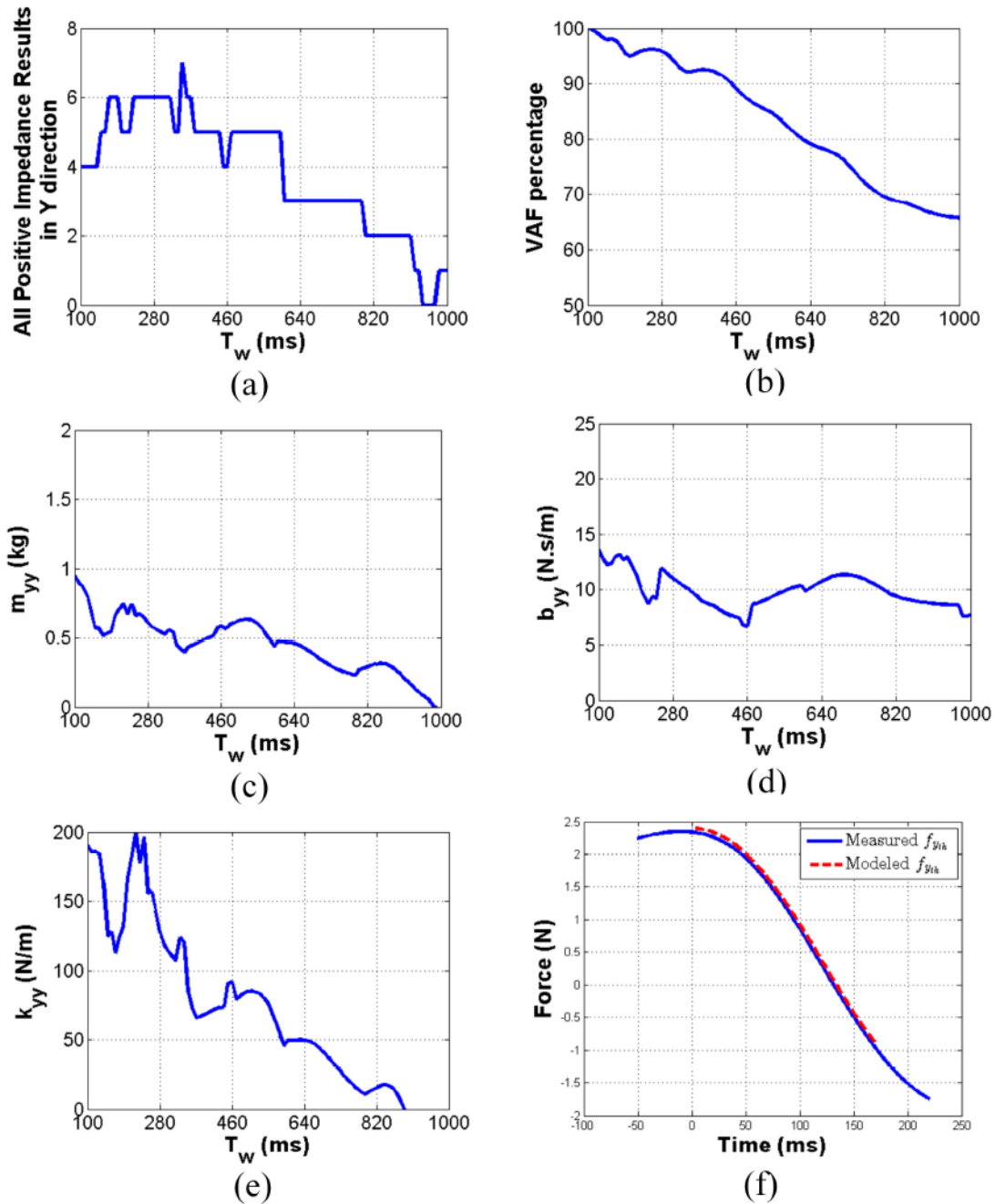
FIGURE 4.9: Impedance identification results as a function of data window lengths T_w for a series of peg-in-the-hole insertion tasks in the Y direction: (a) the number of all-positive impedance identification results, (b) average VAF value in percentage of all-positive impedance identification results; (c) average m_{yy}, (d) average b_{yy}, (e) average k_{yy} of all-positive impedance identification results, (f) impedance model validation with modeled $f_{y_{th}}$ compared to measured $f_{y_{th}}$ for one perturbation with the determined window size at 170 ms and VAF value at 99

tends to decrease the VAF value. Fig. 4.8(c)-(e) show the average m_{xx}, b_{xx} and k_{xx} for all-positive impedance identification results and Fig. 4.9(c)-(e) show the average m_{yy}, b_{yy} and k_{yy}. Finally for the considered series of peg-in-the-hole tasks, T_w is determined to be 960 *ms* for the X direction perturbations and 170 *ms* for the Y direction perturbations. The validation results for one perturbation (origin of the time axis represents the determined onset) in X direction and Y direction are shown in Fig. 4.8(f) and Fig. 4.9(f), respectively, over the timespan of their respective determined T_w.

4.4 Impedance control of Yaskawa Motoman SIA5F robot in the Multi-DOF Scenario

4.4.1 Impedance Controller Design

A more general form of the Time-Delay Estimation (TDE) based impedance controller is implemented on the slave Motoman SIA5F robot during the TOOL phase. Consider the general rigid-body dynamics of the slave robot specified in (4.17). Similar to the derivation in Section 3.4 of Chapter 3, we can separate out a nominal inertia matrix $\bar{\mathbf{M}}_s$ and group the uncertain terms in a matrix $\mathbf{N}$ to have the following robot dynamics:

$$\bar{\mathbf{M}}_s \cdot \ddot{\boldsymbol{\theta}}_s + \mathbf{N} - \boldsymbol{\tau}_p = \boldsymbol{\tau}_s \tag{4.39}$$

with

$$\mathbf{N} = (\mathbf{M}_s - \bar{\mathbf{M}}_s) \cdot \ddot{\boldsymbol{\theta}}_s + \mathbf{C}_s + \mathbf{f}_{rs} \tag{4.40}$$

$\mathbf{N}$ is assumed to be at least piece-wise continuous with respect to time t and therefore we can estimate its value at time t by its past value at time $t - L$ where L is a sufficiently small time delay. Based on (4.39), $\boldsymbol{\tau}_p = \mathbf{J}_s^{\mathrm{T}} \cdot \mathbf{f}_p$, as well as by using the hat symbol ˆ to denote estimated value and the tilde symbol ˜ to denote the time delayed value (by L samples), we have

$$\hat{\mathbf{N}}(t) = \mathbf{N}(t - L) = \tilde{N}$$
$$= \tilde{\boldsymbol{\tau}}_s + \breve{\mathbf{J}}_s^{\mathrm{T}} \cdot \tilde{\mathbf{f}}_p - \bar{\mathbf{M}}_s \cdot \tilde{\ddot{\boldsymbol{\theta}}}_s \tag{4.41}$$

With the target robot dynamics

$$\mathbf{M}_d(\ddot{\mathbf{p}}_s - \ddot{\mathbf{p}}_{sd}) + \mathbf{B}_d(\dot{\mathbf{p}}_s - \dot{\mathbf{p}}_{sd}) + \mathbf{K}_d(\mathbf{p}_s - \mathbf{p}_{sd}) = \mathbf{f}_p \tag{4.42}$$

where $\mathbf{M_d}$, $\mathbf{B_d}$, $\mathbf{K_d}$ are the desired impedance matrices and $\ddot{\mathbf{p}}_{\mathbf{sd}}$, $\dot{\mathbf{p}}_{\mathbf{sd}}$, $\mathbf{p_{sd}}$ denote the desired robot acceleration, velocity and position vectors, we can derive the following control law following the same approach used in Section 3.4 of Chapter 3:

$$\boldsymbol{\tau}_{\mathbf{s}} = \bar{\mathbf{M}}_{\mathbf{s}} \cdot \mathbf{J}_{\mathbf{s}}^{-1}\{\ddot{\mathbf{p}}_{\mathbf{sd}} - \mathbf{M}_{\mathbf{d}}^{-1} \cdot [\mathbf{B_d}(\dot{\mathbf{p}}_{\mathbf{s}} - \dot{\mathbf{p}}_{\mathbf{sd}}) + \mathbf{K_d}(\mathbf{p_s} - \mathbf{p_{sd}}) - \mathbf{f_p}] - \dot{\mathbf{J}}_{\mathbf{s}}\dot{\boldsymbol{\theta}}_{\mathbf{s}}\} + \hat{\mathbf{N}} - \mathbf{J}_{\mathbf{s}}^{\mathbf{T}}\mathbf{f_p} \qquad (4.43)$$

For our application, time delay L is taken to be only 1 sample point (1 ms) for preserving accuracy. The nominal matrix $\bar{\mathbf{M}}$ is a diagonal matrix with positive parameters, and is determined by starting with small initial values for the diagonal entries and gradually increasing their values until the system is on the verge of instability (motions becoming jerky). In this way, a fast estimation convergence can be guaranteed. $\mathbf{f_p}$ is provided by the force sensor after low-pass filtering the force signals with a 5 Hz cut-off frequency. $\ddot{\mathbf{p}}_{\mathbf{sd}}$, $\dot{\mathbf{p}}_{\mathbf{sd}}$ and $\mathbf{p_{sd}}$ are all equal to $[0, 0]^T$ for the task considered, as the desired position is the stationary zero position discussed at the beginning of Section 4.3. $\mathbf{M_d}$, $\mathbf{B_d}$ and $\mathbf{K_d}$ take the following forms:

$$\mathbf{M_d} = \begin{bmatrix} m_{dxx} & m_{dxy} \\ m_{dyx} & m_{dyy} \end{bmatrix}, \quad \mathbf{B_d} = \begin{bmatrix} b_{dxx} & b_{dxy} \\ b_{dyx} & b_{dyy} \end{bmatrix}, \quad \mathbf{K_d} = \begin{bmatrix} k_{dxx} & k_{dxy} \\ k_{dyx} & k_{dyy} \end{bmatrix} \qquad (4.44)$$

Next we discuss how the desired impedance is found.

4.4.2 Derivation of Desired Impedance

The desired impedance matrices $\mathbf{M_d}$, $\mathbf{B_d}$ and $\mathbf{K_d}$ come from the identified therapist arm impedance $\mathbf{Z_{th}}$ as distorted by the teleoperation system dynamics. From (4.29) we can derive that the impedance $\mathbf{Z_d}$ displayed to to the patient via the slave robot during the TIL phase defined by

$$\mathbf{F_p} = -\mathbf{Z_d} \cdot \dot{\mathbf{P}}_{\mathbf{s}} \qquad (4.45)$$

is

$$\mathbf{Z_d} = \left[\mathbf{H_{21}}(\mathbf{Z_{th}} - \mathbf{H_{11}})^{-1}\mathbf{H_{12}} + \mathbf{H_{22}}\right]^{-1} \qquad (4.46)$$

where $\mathbf{Z_{th}}$ is expressed using the identified $\mathbf{M}$, $\mathbf{B}$, $\mathbf{K}$ matrices identified in Section 4.3 as

$$\mathbf{Z_{th}} = \mathbf{M} \cdot s + \mathbf{B} + \frac{\mathbf{K}}{s} \qquad (4.47)$$

and the H_{ij} are the defined in (4.30) - (4.33).

$\mathbf{Z_d}$ calculated from (4.46) should be the target impedance replicated by the slave robot in the TOOL phase. However, in practice we cannot use the result directly because of the following reasons:

1. After the calculation of (4.30)-(4.33) and (4.46) (i.e. after taking into account all the matrices for robot kinematics, dynamics, controllers, and therapist arm impedance), the end result of $\mathbf{Z_d}$ is quite involved. For example in the 1-DOF case in Chapter 3, Z_d was expressed by a 4th order numerator and a third order denominator. We solved the problem by minimizing a cost function measuring the difference between parameters of the original Z_d and a specific form of impedance corresponding to a mass-spring-damper system (see (3.25)-(3.29)). In the 2-DOF case, (4.46) will give expressions of $\mathbf{Z_d}$ with 37th order numerators and 36th order denominators (for each matrix entry). Keep in mind that for impedance controller implementation according to (4.44), $\mathbf{Z_d}$ should take the following form:

$$\mathbf{Z_d} = \begin{bmatrix} Z_{dxx} & Z_{dxy} \\ Z_{dyx} & Z_{dyy} \end{bmatrix}$$
$$= \begin{bmatrix} m_{dxx} \cdot s + b_{dxx} + \dfrac{k_{dxx}}{s} & m_{dxy} \cdot s + b_{dxy} + \dfrac{k_{dxy}}{s} \\ m_{dyx} \cdot s + b_{dyx} + \dfrac{k_{dyx}}{s} & m_{dyy} \cdot s + b_{dyy} + \dfrac{k_{dyy}}{s} \end{bmatrix} \quad (4.48)$$

2. Diagonal terms of $\mathbf{Z_d}$ (which have the most influence over the slave robot during the TOOL phase) can potentially have small damping ratios ζ_x and ζ_y defined as

$$\zeta_x = \frac{b_{dxx}}{2 \cdot \sqrt{k_{dxx} \cdot m_{dxx}}}, \quad \zeta_y = \frac{b_{dyy}}{2 \cdot \sqrt{k_{dyy} \cdot m_{dyy}}} \quad (4.49)$$

which will create instability during impedance control. Another potential source of instability for impedance control is the activity of the specified impedance. The passivity/activity of the specified impedance can be checked using Theorem (1) derived in [6]), with a total of 8 conditions.

Theorem 1. [6] Consider transfer matrix $\mathbf{Z_d}(\mathbf{s})$ of the form in (4.48). $\mathbf{Z_d}(s)$ is positive real (thus the impedance it represents is passive) if and only if all of the following conditions are satisfied:

$$m_{dxy} = m_{dyx} \tag{4.50}$$

$$m_{dxx} \geq 0 \tag{4.51}$$

$$m_{dxx} m_{dyy} \geq m_{dxy} m_{dyx} \tag{4.52}$$

$$b_{dxx} \geq 0 \tag{4.53}$$

$$4 b_{dxx} b_{dyy} \geq (b_{dxx} + b_{dyx})^2 \tag{4.54}$$

$$k_{dxy} = k_{dyx} \tag{4.55}$$

$$k_{dxx} \geq 0 \tag{4.56}$$

$$k_{dxx} k_{dyy} \geq k_{dxy} k_{dyx} \tag{4.57}$$

Our solution to the above-mentioned issues is to first neglect the non-diagonal terms Z_{dxy} and Z_{dyx} of $\mathbf{Z_d}$ in (4.48). By taking $m_{dxy} = m_{dyx} = 0$, $k_{dxy} = k_{dyx} = 0$ and $b_{dxy} = b_{dyx} = 0$, (4.50) and (4.55) are satisfied and all the other 6 conditions in Theorem 1 are reduced to the positivity of m_{dxx}, m_{dyy}, b_{dxx}, b_{dyy}, k_{dxx} and k_{dyy}. Then we apply a process of gradient-based constrained minimization (implemented via *fmincon* command in MATLAB) that will yield $\mathbf{Z_d}$ in the (4.48) while guaranteeing the obtained result's passivity and damping ratio. The cost function that we minimize can be written as

$$Cost(m_d, b_d, k_d) = \sqrt{\sum_{i=1}^{n} (|Z_{ds}(j\omega_i)| - |m_d \cdot j\omega_i + b_d + \frac{k_d}{j\omega_i}|)^2} \tag{4.58}$$

where Z_{ds} designates Z_{dxx} or Z_{dyy} in $\mathbf{Z_d}$ obtained via (4.46) and m_d, b_d, k_d represent the corresponding entries in $\mathbf{M_d}$, $\mathbf{B_d}$ and $\mathbf{K_d}$ matrix. Therefore, there are two cost functions in total for best approximating the frequency response of the diagonal entries of the original $\mathbf{Z_d}$ over a frequency interval $\omega \in [\omega_s, \ \omega_f]$ scanned at steps of $\Delta\omega$ size. Therefore in (4.58), ω_i can be expressed as $\omega_i = \omega_s + \Delta\omega \cdot i$ and $n = \dfrac{\omega_f - \omega_s}{\Delta\omega}$.

For each cost function, the minimization problem can be formulated as

$$\min_{m_d, b_d, k_d} Cost(m_d, b_d, k_d) \ such\,that \begin{cases} 0 < m_d < 50 \\[6pt] 0 < b_d < 1000 \\[6pt] 0 < k_d < 10000 \\[6pt] \dfrac{b_d}{2 \cdot \sqrt{k_d \cdot m_d}} > 0.6 \end{cases} \tag{4.59}$$

The first three constraints guarantee the positivity of the obtained parameters, therefore the passivity of $\mathbf{Z_d}$ based on our discussion about Theorem 1. Some a priori knowledge of the human arm is used to provide the upper bounds for individual impedance parameters. The last constraint guarantees enough damping ratio in each $\mathbf{Z_d}$ diagonal entry. The value 0.6 was based on the impedance controller implementation issues observed over a large number of trials. Having addressed the two concerns raised before finding from the minimization process a set of $\mathbf{M_d}$, $\mathbf{B_d}$ and $\mathbf{K_d}$ to be directly implemented in the controller (4.43), we proceed to experiments in the next section.

4.5 Experimental Results

Experimental results for the LAR telerehabilitation session involving the 2-DOF peg-in-the-hole insertion task are presented in this section. Results obtained from the TIL phase and the TOOL phase are presented separately.

4.5.1 TIL Phase

4.5.1.1 Therapist's Arm Impedance Identification

During the TIL phase, a series of 11 peg-in-the-hole insertion tasks were completed via teleoperation. The experimental trials were carried out during the same day with one healthy person (the author of the thesis) acting as the therapist and another healthy person (the supervisory investigator) acting as the patient (see Appendix D and Appendix E). The force feedback gains for the master robot and the position control gains for the slave robot were chosen to be

- $K_{f1} = 0.3$, $K_{f2} = 0.3$

- $K_{p1} = 4629.50\,N.m/rad$, $K_{v1} = 57.87\,N.m/(rad/s)$,
  $K_{p2} = 1468.61\,N.m/rad$, $K_{v2} = 18.36\,N.m/(rad.s)$

While the tasks were being completed, the position and force data on the therapist's side were recorded. By using the technique described in Section 4.3, we obtain identify following results for the therapist's arm impedance:

- $m_{xx} = 3.379\,kg$, $b_{xx} = 25.15\,N.s/m$, $k_{xx} = 980.552\,N/m$

- $m_{yy} = 0.518\,kg$, $b_{yy} = 12.96\,N.s/m$, $k_{yy} = 112.617\,N/m$

We can see that the arm demonstrates a stiffer impedance along the Y direction, which agrees with the findings of [6]. We can write $\mathbf{Z_{th}}$ as

$$\mathbf{Z_{th}} = \begin{bmatrix} 3.379s + 25.15 + \dfrac{980.552}{s} & 0 \\ 0 & 0.518s + 12.96 + \dfrac{112.617}{s} \end{bmatrix} \qquad (4.60)$$

4.5.1.2 Linear Approximation of the Master Robot Dynamics

By applying a persistent perturbation to the master robot, we can identify the coefficients $\alpha_1 \ldots \alpha_5$ of (4.14), (4.15) and (4.16) as

- $\alpha_1 = 0.0556$, $\alpha_2 = 0.0969$, $\alpha_3 = 0.0687$, $\alpha_4 = 0.0942$, $\alpha_5 = 0.0731$

As we can see the resulting robot dynamics based on (4.13) are nonlinear while our analysis (Fig. 4.4) on the teleoperation system follows a linear approach requiring a linear transfer function for Z_m. This issue can be addressed by taking into account the fact that the robot moves around the zero position ($\theta_{1m} \simeq -9°$ and $\theta_{2m} \simeq 0°$, as discussed in Section 4.3) in the considered task. Remember that $\theta_{1m} \neq 0°$ because we wanted to keep a safe distance between the 1st link of the master robot and its own frame. Therefore, we will approximate the $sin(\theta_{1m} - \theta_{2m})$ in (4.14) by -0.1574 and the $cos(\theta_{1m} - \theta_{2m})$ term in (4.15) by 1 (when q is small, $sin(q) \simeq q$ and $cos(q) \simeq 1$). As a result,

$$\mathbf{M_m} \simeq \begin{bmatrix} \alpha_1 & 0.079 \cdot \alpha_2 \\ 0.079 \cdot \alpha_2 & \alpha_3 \end{bmatrix} \qquad (4.61)$$

which is now a constant. Further, we can group $\mathbf{C_m} \cdot \dot{\boldsymbol{\theta}}_m$ and $\mathbf{f_{rm}}$ in (4.13) together because they now both only depend on the joint velocities:

$$\mathbf{C_m} \cdot \dot{\boldsymbol{\theta}}_m + \mathbf{f_{rm}} \simeq \begin{bmatrix} \dfrac{1}{2} \cdot \alpha_2 \dot{\theta}_{2m}^2 + \alpha_4 \dot{\theta}_{1m} \\ \dfrac{1}{2} \cdot \alpha_2 \dot{\theta}_{1m}^2 + \alpha_5 \dot{\theta}_{2m} \end{bmatrix} \qquad (4.62)$$

We can further simplify (4.62), which is a 2-by-1 vector with each each entry made up of the sum of one first order term and one 2nd order term with respect to joint velocity, by ignoring the 2nd order velocity terms because in practice their contribution to $\mathbf{C_m} \cdot \dot{\boldsymbol{\theta}}_m + \mathbf{f_{rm}}$ is much smaller than the 1st order terms. As it can be seen in Fig. 4.10, for a typical peg-in-the-hole insertion task the 1st order
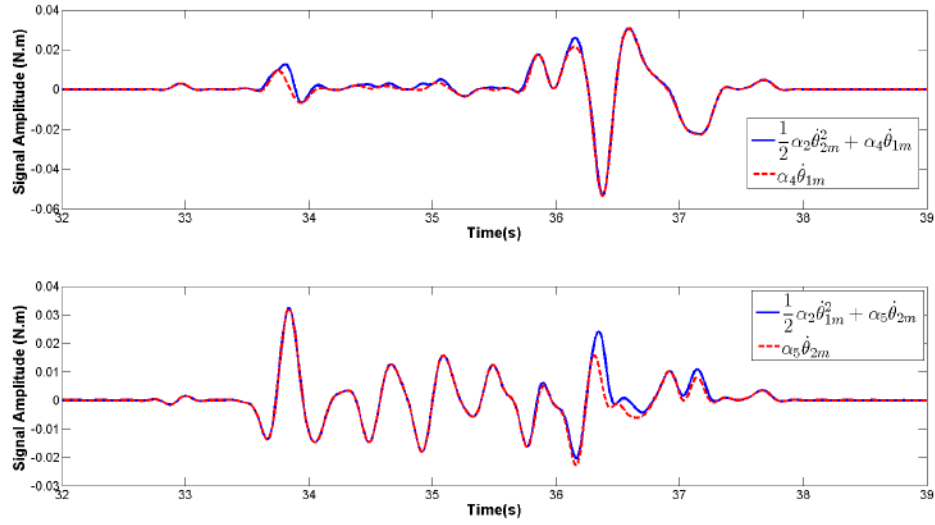
FIGURE 4.10: A comparison between the first order terms with respect to joint velocity and the total sum of the first order terms plus second order terms in $\mathbf{C_m} \cdot \dot{\boldsymbol{\theta}}_m + \mathbf{f_{rm}}$ for a typical peg-in-hole task.

terms can approximate very well the total sum. Therefore,

$$\mathbf{C_m} \cdot \dot{\boldsymbol{\theta}}_m + \mathbf{f_{rm}} \simeq \begin{bmatrix} \alpha_4 \dot{\theta}_{1m} \\ \\ \alpha_5 \dot{\theta}_{2m} \end{bmatrix} \tag{4.63}$$

Combining the above with (4.61), we have the simplified linear dynamics of the master robot:

$$\mathbf{Z_m} = \begin{bmatrix} \alpha_1 & 0.079 \cdot \alpha_2 \\ 0.079 \cdot \alpha_2 & \alpha_3 \end{bmatrix} s + \begin{bmatrix} \alpha_4 & 0 \\ 0 & \alpha_5 \end{bmatrix}$$

$$= \begin{bmatrix} 0.0556 & 0.0077 \\ 0.0077 & 0.0687 \end{bmatrix} s + \begin{bmatrix} 0.0942 & 0 \\ 0 & 0.0731 \end{bmatrix} \tag{4.64}$$

4.5.1.3 Linear Approximation of the Slave Robot Dynamics

As for the slave robot, the numerical values for the parameters in the robot dynamics (4.17) lead us to

$$
\begin{bmatrix} 1.35 + 0.22\sin(\theta_{2s}) & 0.086 + 0.11\sin(\theta_{2s}) \\ 0.086 + 0.11\sin(\theta_{2s}) & 0.086) \end{bmatrix} \cdot \ddot{\boldsymbol{\theta}}_s
$$
$$
+ \begin{bmatrix} 0.11\cos(\theta_{2s})\dot{\theta}_{2s} & 0.11\cos(\theta_{2s})(\dot{\theta}_{1s} + \dot{\theta}_{2s}) \\ -0.11\cos(\theta_{2s})\dot{\theta}_{1s} & 0 \end{bmatrix} \cdot \dot{\boldsymbol{\theta}}_s + \begin{bmatrix} 15.3 & 0 \\ 0 & 9.5 \end{bmatrix} \cdot \dot{\boldsymbol{\theta}}_s = \boldsymbol{\tau}_s + \boldsymbol{\tau}_p \quad (4.65)
$$

By following a similar approach as we did with the master robot, we can approximate the nonlinear slave robot dynamics with linear dynamics. After taking into account the zero position (resulting in $\sin(\theta_{2s}) \simeq 0$ and $\cos(\theta_{2s}) = 1$) and neglecting the higher order dependencies on $\dot{\boldsymbol{\theta}}_s$, we obtain the following linear impedance model for the slave robot:

$$
\mathbf{Z_s} = \begin{bmatrix} 1.35 & 0.086 \\ 0.086 & 0.086 \end{bmatrix} s + \begin{bmatrix} 15.3 & 0 \\ 0 & 9.5 \end{bmatrix} \tag{4.66}
$$

4.5.1.4 Desired Impedance

Now, we have all the elements to calculate $\mathbf{Z_d}$ in (4.46). The calculation is first done in Maple software (Maplesoft^{TM}, Ontario, Canada) and then the polynomial parameters from the diagonal entries of $\mathbf{Z_d}$ (non-diagonal terms are ignored as discussed in Section4.4 in order to respect passivity requirements in Theorem 1) are passed directly into MATLAB for model-order reduction optimization based on the process described in Section 4.4. For optimization (4.58) and (4.59), we sweep the frequency range of interest (low frequency) from $\omega_s = 0.005\ Hz$ to $\omega_f = 20\ Hz$ with steps of $\Delta\omega = 0.005\ Hz$. The optimization yields

$$
\mathbf{M_d} = \begin{bmatrix} 9.77 & 0 \\ 0 & 1.23 \end{bmatrix} \tag{4.67}
$$

$$
\mathbf{B_d} = \begin{bmatrix} 180.56 & 0 \\ 0 & 60.82 \end{bmatrix} \tag{4.68}
$$

$$
\mathbf{K_d} = \begin{bmatrix} 2316.20 & 0 \\ 0 & 360.233 \end{bmatrix} \tag{4.69}
$$
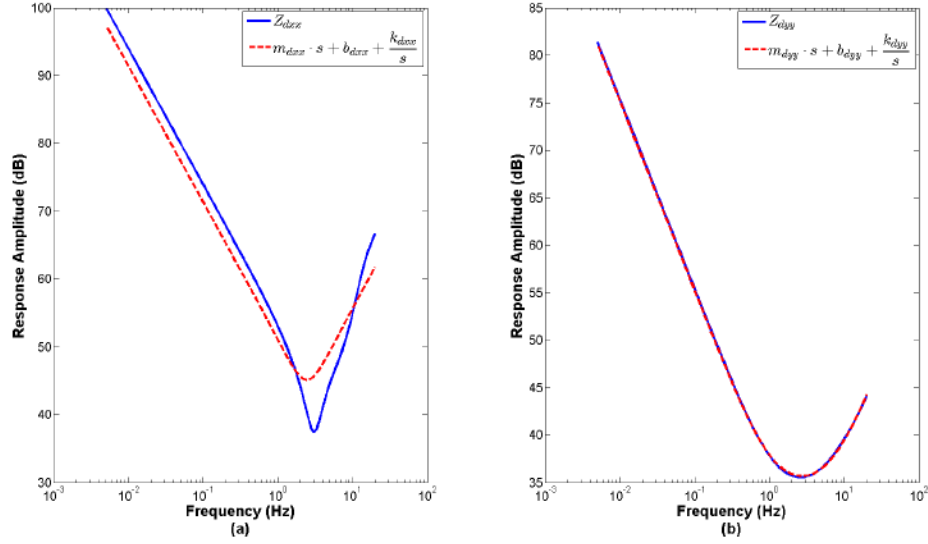
FIGURE 4.11: Comparison of the amplitude of the frequency response between (a) Z_{dxx} and $m_{dxx} \cdot s + b_{dxx} + \frac{k_{dxx}}{s}$; (b) Z_{dyy} and $m_{dyy} \cdot s + b_{dyy} + \frac{k_{dyy}}{s}$

which can be directly applied in (4.43) for impedance control during the TOOL phase. The optimization results are validated by comparing the frequency response of each diagonal entry of $\mathbf{Z_d}$ obtained from (4.46) and the corresponding entry of $\mathbf{M_d} \cdot s + \mathbf{B_d} + \frac{\mathbf{K_d}}{s}$ obtained from model-order reduction optimization. The comparison plots are shown in Fig. 4.11. As it can be seen, after meeting all the constraints, $\mathbf{M_d}$, $\mathbf{B_d}$ and $\mathbf{K_d}$ approximate well the $\mathbf{Z_d}$ removed of its non-diagonal entries.

4.5.2 TOOL Phase

In the TOOL phase, the slave robot is programmed to demonstrate the desired impedance (4.42) via the controller (4.43). $\bar{\mathbf{M}}_s$ is selected to be

$$\bar{\mathbf{M}}_s = \begin{bmatrix} 2.5 & 0 \\ 0 & 0.3 \end{bmatrix} \tag{4.70}$$

by gradually increasing the values until the impedance-controlled robot starts to display instability. Under such circumstances, the TDE approach will have the fastest estimation convergence while ensuring the system stability. We repeated the peg-in-the-hole insertion task in the absence of the therapist for a dozen of times. The task was completed successfully with the slave robot alone. If the robot impedance was not controlled properly, the robot could yield to pressure from the patient
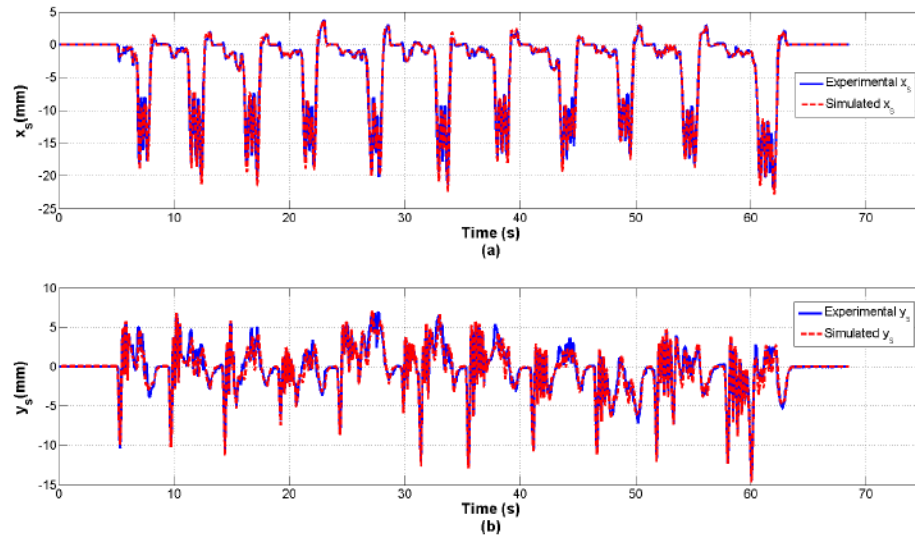
FIGURE 4.12: Comparison between simulated positions based on force measurement and the actual positions during TOOL phase in (a) X direction, (b) Y direction

and the task would fail. The impedance control implementation is validated by comparing the actual robot position in both X and Y directions with what the target impedance model predicts based on the measured forces. A good match in both directions is shown in Fig. 4.12. The desired behaviour has therefore been successfully mapped from the therapist to the slave robot during the TOOL phase for the 2-DOF peg-in-the-hole insertion task.

4.6   Conclusion

In this chapter, we demonstrated the proposed LAR telerehabilitation concept for a 2-DOF peg-in-the-hole task. We first showed that we could complete the therapy task successfully in 2 DOF through teleoperation while measuring the therapist's arm impedance in two directions. We also incorporated the entire system's dynamics into account to derive the desired impedance matrix used for impedance control implementation on the slave robot during TOOL phase. An appropriate optimization algorithm was also designed. In the end, we were able to complete the impedance control in 2 DOF and demonstrated feasibility of the proposed LAR telerehabilitation paradigm on the 2-DOF peg-in-the-hole task.

Chapter 5

Telerehabilitation System Stability Analysis

In this chapter, we investigate the stability analysis issues arising from introducing active operator(s) into the teleoperation system. This is particularly pertinent to telerehabilitation because the therapist's assistive role during the therapist-in-loop phase of the proposed telerehabilitation paradigm can be active [59] (also as discussed in Chapter 4). At the same time the therapist's resistive role can be strictly passive that can be used to relax stability criteria for enhanced transparency in the teleoperation system. On the other hand, multiple active operators may be present in multilateral teleoperation systems. For example in robot-assisted mirror therapy with therapist assistance, which is a special case of trilateral teleoperation, 1, 2 or 3 terminations can be active[45]. Therefore we are interested in improving existing teleoperation stability analysis tools, which assume the simple passivity of operators, to be able to deal with multiple active or strictly passive operators.

5.1   Introduction

Haptic teleoperation and haptic interaction systems (collectively, haptic systems) have seen increasing applications in recent years. In particular, a multilateral haptic teleoperation system can be modeled as a multi-port network representing a teleoperator (consisting of the robots, their controllers and communication channels), connected to one-port network terminations modeling the dynamics of the human operators and/or the environments. Similarly, a multilateral haptic interaction system can be modeled as a multi-port network representing a haptic virtual environment (HVE), connected to one-port network terminations modeling the dynamics of the human operators. The analysis of

stability of such coupled systems can be difficult because the exact physical properties of the human operators and environments are typically unknown, uncertain or time-varying, thus making the classical approaches such as the Routh-Hurwitz criteion, inapplicable. In the presence of these uncertainties, the concept of absolute stability is often utilized. In the case of a two-port network, the absolute stability criterion ensures the coupled system's BIBO (bounded-input/bounded-output) stability for two passive but otherwise arbitrary terminations [60]. Closed-form absolute stability conditions involving the two-port network's immittance parameters are given by a well-known criterion proposed by Llewellyn [61]. Thus, in traditional bilateral teleoperation, Llewellyn's criterion has been widely used for stability analysis, based on the assumption that both the human operator and the environment are linear time invariant (LTI) and passive [12, 62]. In trilateral teleoperation, which is seeing emerging applications in telerehabilitation [43], collaborative surgical training [63] and cooperative multi-robot systems [64], our research group has developed a similar approach for absolute stability analysis based on the same passivity assumption on terminations [65].

For the human arm, although this assumption of passivity is valid when considering tasks involving a relaxed arm (or relaxed grasp) [66], it can be violated in tasks involving posture-maintenance (or rigid grasp) [6]. This could be the case in a bilateral telerehabilitation system for telepresenting a hospital-based therapist to a home-based patient in order to enable home-based rehabilitation. The reasons for considering both the therapist and the patient as active terminations are as follows. First, the therapist would be required to execute complex motor control tasks. For instance, the therapist might exert resistive forces against a patient to build muscle strength – this task bears resemblance to the rigid grasp task, which was shown in [6] to involve activity. Second, inter-muscular feedback with unequal gains has previously been linked to the arm impedance activity [67] making it possible that the patient also demonstrates an active impedance. The degree of activity can be described by the concept of shortage of passivity (SOP) defined mathematically later.

From another perspective, the assumption of having an arbitrary passive termination can lead to conservative stability conditions on the teleoperator. This happens if a termination is strictly input or output passive. For example, a mass-spring-damper system is output strictly passive in the admittance domain with an excess of passivity (EOP) equal to the system damping [68]. Excess of passivity of a termination can be used to design teleoperation systems with higher performance.

In order to derive effective stability conditions for multi-port networks involving active or strictly passive terminations, we can utilize prior knowledge concerning EOP or SOP values on the human operators or/and environments. Past work includes using Mobius transformation to map the impedance of one termination to the driving point impedance seen at the other port connected to an

unknown LTI passive termination [9]. This approach, however, is limited to considering only one active or strictly passive termination for a two-port network while the other termination is simply passive. Wave variables and scattering parameters have also been used to relax Llewellyn's criterion on bounded passive terminations [11], but not for active terminations. Also, in this work, *S*-parameters are needed, but a stability condition expressed *directly* in the immitance (e.g. impedance) domain is more desirable, because *S*-parameters are most accurately measured for systems with higher frequency such as microwave circuits while impedance parameters can be measured accurately for mechanical systems. The approach proposed in this chapter will rely solely on the impedance representation. Another approach to relax conservatism during application of Llewellyn's criterion is the series-shunt approach [62, 69]. These papers allow taking into account the lower and upper bound on the impedance of a passive termination. However, the human operator and environment were still assumed to be passive. All of the above are limited to bilateral teleoperation systems and do not offer stability criteria for trilateral systems. In this chapter, we will utilize the series-shunt approach to take into account different topologies of passive and active terminations to derive explicit stability conditions on the teleoperator, both in two-port network (bilateral) and three-port network (trilateral) cases. The same approach is applicable to *n*-port networks with larger *n*.

The chapter is organized as follows. First, passivity and activity are defined mathematically, and existing absolute stability criteria for two-port and three-port networks are reviewed in Section 5.2. In Section 5.3, the series-shunt approach is applied to two-port and three-port networks to derive stability conditions when one or multiple terminations are active or strictly passive. Although the conditions derived in Section 5.3 are general, they are applied to bilateral and trilateral teleoperation systems in Section 5.4. Closed-form conditions on controller parameters under position-error-based (PEB) control paradigm and experimental results are presented. Finally Section 5.5 contains concluding remarks.

5.2 Definitions and Absolute Stability Criteria for Two-port and Three-port Networks

In this section, we review the definitions of passivity and activity as well as the existing stability criteria for two-port and three-port networks. Different passivity/activity topologies will be defined including input strictly passive (ISP), input non-passive (INP), output strictly passive (OSP), output non-passive (ONP), and disc-like non-passive (DNP).

5.2.1 Definitions and Lemmas of passivity and activity

Definition 1. [70] A system with input $u(.)$ and output $y(.)$ where $u(t), y(t) \in \mathbb{R}^m$ is passive if there is a constant β such that

$$\int_0^t y^T(\tau)u(\tau)d\tau \geq \beta \tag{5.1}$$

for all functions $u(.)$ and all $t \geq 0$. The constant β is the energy stored in the system at time $t = 0$. If further, there exist positive constants δ and ε such that

$$\int_0^t y^T(\tau)u(\tau)d\tau \geq \beta + \delta \int_0^t u^T(\tau)u(\tau)d\tau + \varepsilon \int_0^t y^T(\tau)y(\tau)d\tau \tag{5.2}$$

for all functions $u(.)$ and all $t \geq 0$, the system is ISP if $\delta > 0, \varepsilon = 0$, and OSP if $\varepsilon > 0, \delta = 0$. The values of δ and ε are the EOP for the ISP and OSP systems, respectively.

A system is non-passive (active) if it is not passive. Based on the above definition, we can have the corresponding definition for different non-passivities:

Definition 2. In Definition 1, if $\delta < 0$ then the system is INP with SOP of $\eta = -\delta$; if $\varepsilon < 0$ then the system is ONP with SOP of $\mu = -\varepsilon$.
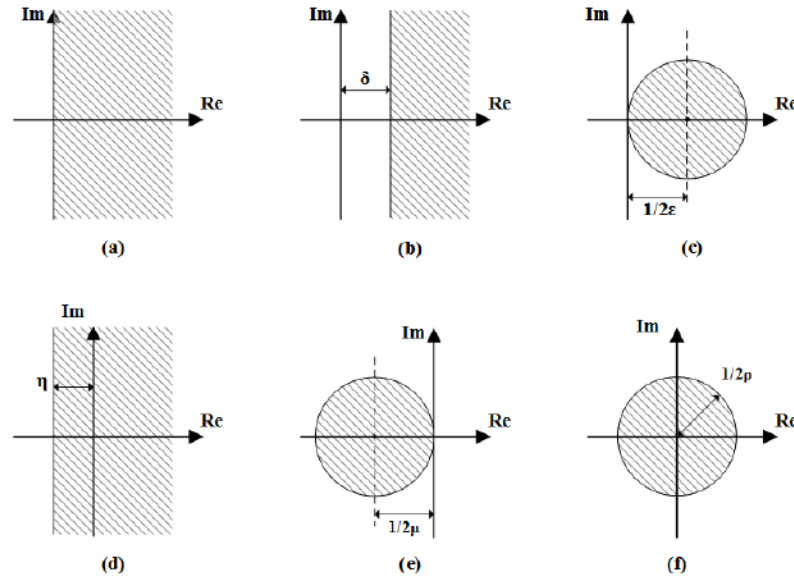
FIGURE 5.1: Nyquist diagram regions of (a) a passive system, (b) an ISP system with EOP of δ, (c) an OSP system with EOP of ε, (d) an INP system with SOP of η, (e) an ONP system with SOP of μ, (f) a DNP system with SOP of ρ.

When a single-input/single-output (SISO) system is represented in the frequency domain by a transfer function, the following lemmas establish the connection between different types of passivity and the region covered by the transfer function's Nyquist diagram (Fig.5.1):

Lemma 5.1. *[70] A system represented by an LTI rational transfer function $G(s)$ with all poles having negative real parts is passive if and only if* $\mathrm{Re}(G(j\omega)) \geq 0, \forall \omega$ *(Fig. 5.1(a)).*

Lemma 5.2. *[70] A system represented by an LTI rational transfer function $G(s)$ with all poles having negative real parts is ISP with EOP of δ if and only if* $\mathrm{Re}(G(j\omega)) \geq \delta, \forall \omega$ *(Fig. 5.1(b)).*

Lemma 5.3. *[70] A system represented by an LTI rational transfer function $G(s)$ with all poles having negative real parts is OSP with EOP of ε if and only if* $\mathrm{Re}(G(j\omega)) \geq \varepsilon|G(j\omega)|, \forall \omega$, *i.e. the Nyquist diagram of $G(j\omega)$ is contained in a circle with center on the real axis at $1/2\varepsilon$ and with a radius of $1/2\varepsilon$ (Fig.5.1(c)).*

By the same token, the SOP of INP and ONP systems can be related to their Nyquist diagrams in Fig. 5.1(d) and Fig. 5.1(e) respectively. Finally, we define a DNP system with its transfer function:

Definition 3. An LTI system $G(s)$ is called DNP with SOP of ρ (not based on (5.2) but) if $|G(j\omega)| \leq 1/2\rho$, i.e., the Nyquist diagram of $G(s)$ is contained in a circle centered at the origin with a radius of $1/2\rho$ (Fig. 5.1(f)).

The reason for considering these passivity/activity topologies is their direct physical relevance in the immittance domain. For example, the impedances of the human arm in rigid and relaxed grasping tasks have been shown to be INP and ISP, respectively [6]. Given the reciprocal relationship between impedance and admittance, it is easy to see that an INP termination in the impedance domain is ONP in the admittance domain and vice versa, while an ISP termination in the impedance domain is OSP in the admittance domain and vice versa. Thus, the admittances of the human arm in rigid and relaxed grasping tasks are ONP and OSP, respectively. Also, due to the limited co-contraction of human arm muscles, there is an upper bound on the magnitude of the arm impedance, which means the arm can always be modeled by a DNP impedance. Therefore, there is a need for considering the effect of INP, ISP, ONP, OSP and DNP immittance on stability. Note that although the rest of the chapter is based on impedance parameters, the results derived here will apply to any immittance representation.

5.2.2 Existing absolute stability criteria for two-port and three-port networks

We review two absolute stability criteria in the literature that we will later use to derive stability conditions with different termination impedance topologies. Immittance-based stability criteria lend

themselves well to our extension of the series-shunt approach. Therefore, first we consider an LTI two-port network which can be modeled by its impedance (Z) parameters as

$$\begin{bmatrix} V_1(s) \\ V_2(s) \end{bmatrix} = \begin{bmatrix} Z_{11}(s) & Z_{12}(s) \\ Z_{21}(s) & Z_{22}(s) \end{bmatrix} \begin{bmatrix} I_1(s) \\ I_2(s) \end{bmatrix} \tag{5.3}$$

where the effort/flow pairs (V_1, V_2) and (I_1, I_2) denote the voltages and currents at the two terminals. A three-port network's impedance matrix relationship incorporates three pairs of effort/flow variables:

$$\begin{bmatrix} Z_{11}(s) & Z_{12}(s) & Z_{13}(s) \\ Z_{21}(s) & Z_{22}(s) & Z_{23}(s) \\ Z_{31}(s) & Z_{32}(s) & Z_{33}(s) \end{bmatrix} \tag{5.4}$$

Lemma 5.4. *[60] The two-port network (5.3) is absolutely stable if and only if*

1. *Z_{11} and Z_{22} have no poles in the right-half plane (RHP),*

2. *Any poles of Z_{11} and Z_{22} on the imaginary axis are simple with real and positive residues, and*

3. *For all real positive frequencies ω,*

$$\mathrm{Re}(Z_{11}) \geq 0$$
$$\mathrm{Re}(Z_{22}) \geq 0$$
$$2\mathrm{Re}(Z_{11})\mathrm{Re}(Z_{22}) - \mathrm{Re}(Z_{12}Z_{21}) - |Z_{12}Z_{21}| \geq 0 \tag{5.5}$$

Lemma 5.5. *[65] The three-port network with the impedance matrix Z in (5.4) satisfying the symmetrization condition*

$$Z_{13}Z_{21}Z_{32} - Z_{12}Z_{23}Z_{31} = 0 \tag{5.6}$$

is stable if and only if

$$\text{Re}(Z_{11}) \geq 0, \tag{5.7}$$

$$\text{Re}(Z_{22}) \geq 0, \tag{5.8}$$

$$\text{Re}(Z_{33}) \geq 0, \tag{5.9}$$

$$2\text{Re}(Z_{11})\text{Re}(Z_{22}) - |Z_{12}Z_{21}| + \text{Re}(Z_{12}Z_{21}) \geq 0, \tag{5.10}$$

and

$$2\text{Re}(Z_{11})\text{Re}(Z_{22})\text{Re}(Z_{33})$$
$$- \text{Re}(Z_{11})(|Z_{23}Z_{32}| + \text{Re}(Z_{23}Z_{32}))$$
$$- \text{Re}(Z_{22})(|Z_{13}Z_{31}| + \text{Re}(Z_{13}Z_{31}))$$
$$- \text{Re}(Z_{33})(|Z_{12}Z_{21}| + \text{Re}(Z_{12}Z_{21}))$$
$$+ 4\text{Re}(\sqrt{Z_{12}Z_{21}})\text{Re}(\sqrt{Z_{13}Z_{31}})\text{Re}(\sqrt{Z_{23}Z_{32}}) \geq 0 \tag{5.11}$$

5.3 Main Results

In this section we consider the two-port and three-port networks described by (5.3) and (5.4).

5.3.1 Decomposition of terminations into series/parallel impedances via Mobius transformation
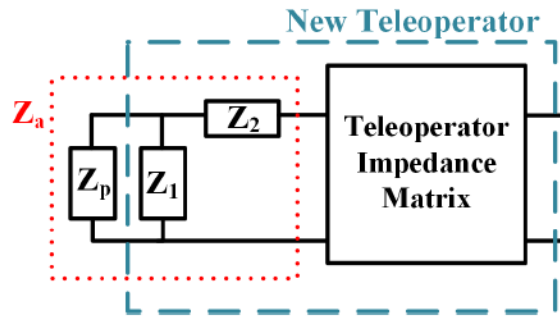
FIGURE 5.2: Decomposition of termination Z_a into a passive impedance Z_p in parallel connection with Z_1 and series connection with Z_2.

In order to utilize information on the topology of termination impedances so that we can derive less conservative stability conditions for overly passive terminations and valid conditions for active terminations, we propose to first decompose a given termination impedance into a passive (but arbitrary) impedance in series/shunt connection with other to-be-determined impedances. Consider a termination impedance Z_a in Fig. 5.2, the impedance topology of which is known, i.e., we know

whether it is passive, active (INP, ONP or DNP with a given SOP), or strictly passive (ISP or OSP with a given EOP). We decompose it into a passive impedance Z_p in parallel connection with an impedance Z_1 and then the total in series connection with an impedance Z_2. The goal is that the overall impedance will represent the topology characterizing Z_a. Note that despite the fact that Z_a and Z_p are complex impedances, we have $Z_1, Z_2 \in \mathbb{R}$; we will see later that they will be able to map the passive impedance Z_p to different regions shown in Figure. 5.1. Now, Z_1 and Z_2 (for each termination) can be assimilated into the original two-port (or three-port) network impedance to make an *augmented network*, such that Lemma 5.4 and 5.5 can be applied to the new coupled system consisting of the passive Z_p (for the corresponding termination) and the augmented network. Fig.5.2 only shows the case for one termination, but the teleoperator can be augmented to incorporate Z_1 and Z_2 for as many terminations as needed. This approach for decomposing termination impedances is illustrated with INP/ISP, OSP and DNP examples in the following.

5.3.1.1 Decomposition of ISP/INP terminations

In the case of ISP and INP terminations, the complex plane regions in Fig. 5.1 (b) and (d) with EOP of δ and SOP of η, respectively, are obtained by a translation of the RHP along the real axis by δ or $-\eta$. Therefore $Z_1 = \infty$, reducing the termination to a series connection of Z_p and Z_2, with Z_2 taking the value of δ or $-\eta$.

5.3.1.2 Decomposition of OSP terminations

If Z_a in Fig. 5.2 is OSP with EOP of ε, we can set the value of Z_2 to 0 and the value of Z_1 to $1/\varepsilon$. The combined impedance Z_a will be

$$Z_a = \frac{Z_p \cdot 1/\varepsilon}{Z_p + 1/\varepsilon} \tag{5.12}$$

Which, as argued below, can characterize a given OSP impedance with EOP of ε. In fact, this is a Mobius transformation [71] with regard to Z_p; recall that Z_p is any arbitrary impedance in the RHP. The transformation (5.12) consists of four steps:

1. Horizontal translation by $1/\varepsilon$ of the region of the impedance Z_p, which is the RHP (Fig. 5.3(a) to Fig. 5.3(b)); i.e., $f_1(Z_p) = Z_p + 1/\varepsilon$

2. Inversion of the result of step 1 (Fig. 5.3(b) to Fig. 5.3(c)); i.e., $f_2(Z_p) = 1/f_1(Z_p)$

3. Scaling the result of step 2 by a factor of $-1/\varepsilon^2$ (Fig. 5.3(c) to Fig. 5.3(d)); i.e., $f_3(Z_p) = -f_2(Z_p)/\varepsilon^2$

4. Horizontal translation by $1/\varepsilon$ (Fig.5.3(d) to Fig.5.3(e)) ; i.e., $f_4(Z_p) = f_3(Z_p) + 1/\varepsilon$.

It is easy to see that $f_4(Z_p)$ is the same as Z_a in (5.12). Therefore, with $Z_1 = 1/\varepsilon$ and $Z_2 = 0$ we can recover the OSP termination with an EOP of ε.
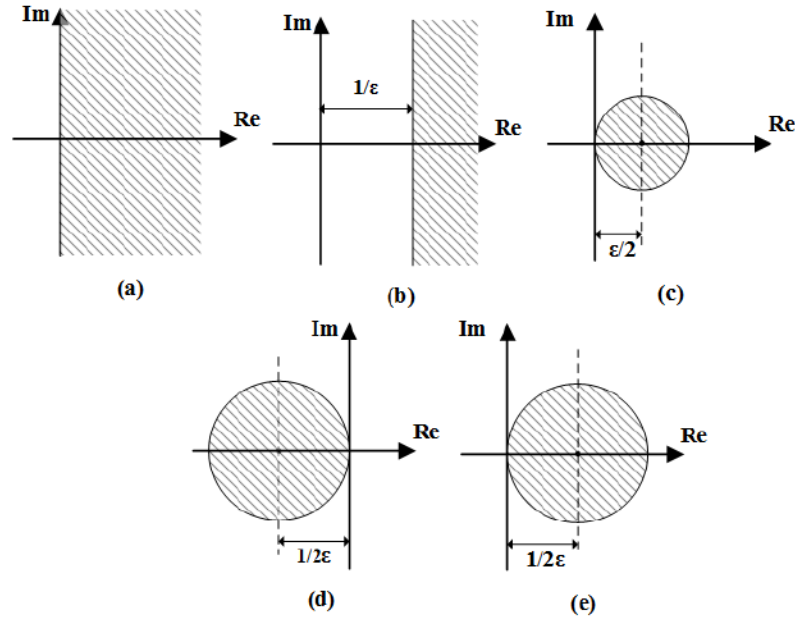
FIGURE 5.3: Step-by-step Mobius transformation of the RHP to OSP topology

5.3.1.3 Decomposition of DNP terminations

From Fig. 5.1(f), it can be seen that a DNP impedance with SOP of ρ can be obtained by applying a horizontal translation of $-1/2\rho$ to the region covered by an OSP impedance with EOP of ρ. Therefore, we can set the value of Z_1 to $1/\rho$ and Z_2 to $-1/2\rho$ to recover the region covered by a DNP termination in the Nyquist plane.

5.3.1.4 Decomposition of ONP terminations

Similar to the DNP termination, from Fig. 5.1(e) it can be seen that an ONP impedance with SOP of μ can be obtained by applying a horizontal translation of $-1/\mu$ to the region covered by an OSP impedance with EOP of μ. Therefore, we can set the value of Z_1 to $1/\mu$ and Z_2 to $-1/\mu$ to recover the region covered by a DNP termination in the Nyquist plane.

5.3.2 Augmented teleoperator impedance with different termination combinations

After termination impedance decomposition in Section 5.3.1, we can incorporate the Z_1 and Z_2 associated with each termination into the teleoperator impedance matrix to form a new teleoperator impedance matrix.

5.3.2.1 Bilateral teleoperator case

In the two-port network case, the new teleoperator impedance matrix calculation can be systematically carried out by first calculating the equivalent *chain matrix* for the two-port network comprised of the Z_1 and Z_2 combination at each termination. Then, the new teleoperator can be expressed in terms of its chain (ABCD) parameters by calculating the product of the chain matrices of the individual two-port networks as the three two-port networks are in cascade connection (Fig. 5.4) [60]. The reason for utilizing the chain matrix instead of, say, the impedance matrix representation for each two-port network is this very ability to multiply the matrices of the cascaded networks to get the matrix for the total network. Finally, the equivalent impedance matrix of the augmented teleoperator can be obtained by performing a parameter conversion from the total chain matrix to impedance matrix.
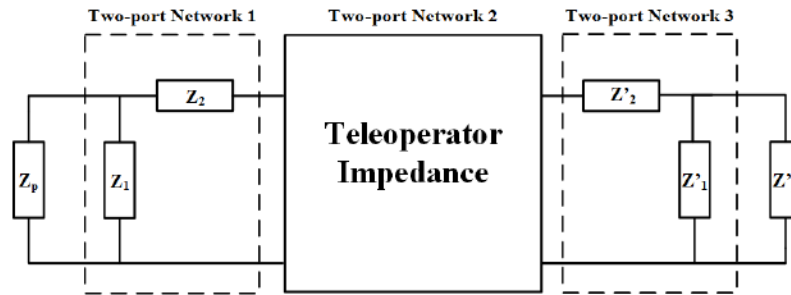
FIGURE 5.4: Cascade connection of two-port networks 1-3, consisting of the original teleoperator two-port network and two equivalent two-port networks from termination decompositions

Next, the INP, OSP and DNP terminations are considered to form different termination combinations for the two ports of the two-port network and their corresponding augmented teleoperator impedance matrices are reported in Table 5.1. Due to the symmetries, only six distinct cases exist: INP-INP (i.e., ports 1 and 2 are connected to INP terminations that are not necessarily the same), OSP-OSP, DNP-DNP, INP-OSP, INP-DNP, and OSP-DNP. We take termination 1's EOP/SOP to be a and termination 2's EOP/SOP to be b. Note that it suffices to change the sign of the SOP of an INP termination in order to get the results for an ISP termination.

TABLE 5.1: Augmented teleoperator impedance matrix with different termination topology combinations, where $M = Z_{22} + a(Z_{11}Z_{22} - Z_{12}Z_{21})$, and $N = Z_{11} + b(Z_{11}Z_{22} - Z_{12}Z_{21})$

Term. 1 \ Term. 2	INP with SOP of b	OSP with EOP of b	DNP with SOP of b
INP with SOP of a	$\begin{bmatrix} Z_{11}-a & Z_{12} \\ Z_{21} & Z_{22}-b \end{bmatrix}$	$\begin{bmatrix} \frac{N-abZ_{22}-a}{1+bZ_{22}} & \frac{Z_{12}}{1+bZ_{22}} \\ \frac{Z_{21}}{1+bZ_{22}} & \frac{Z_{12}}{1+bZ_{22}} \end{bmatrix}$	$\begin{bmatrix} \frac{N-abZ_{22}-a}{1+bZ_{22}} & \frac{Z_{12}}{1+bZ_{22}} \\ \frac{Z_{21}}{1+bZ_{22}} & \frac{-1+bZ_{22}}{2b(1+bZ_{22})} \end{bmatrix}$
OSP with EOP of a	⋆	$\begin{bmatrix} \frac{N}{aN+bZ_{22}+1} & \frac{Z_{12}}{aN+bZ_{22}+1} \\ \frac{Z_{21}}{aN+bZ_{22}+1} & \frac{M}{aN+bZ_{22}+1} \end{bmatrix}$	$\begin{bmatrix} \frac{N}{aN+bZ_{22}+1} & \frac{Z_{12}}{aN+bZ_{22}-1-2aZ_{11}} \\ \frac{Z_{21}}{aN+bZ_{22}+1} & \frac{aN+bZ_{22}-1-2aZ_{11}}{2b(aN+bZ_{22}+1)} \end{bmatrix}$
DNP with SOP of a	⋆	⋆	$\begin{bmatrix} \frac{2aN-bZ_{22}-1}{a(2aN+bZ_{22}+1)} & \frac{2Z_{12}}{2aN+bZ_{22}+1} \\ \frac{Z_{21}}{2aN+bZ_{22}+1} & \frac{2aN-4aZ_{11}+bZ_{22}-1}{2b(2aN+bZ_{22}+1)} \end{bmatrix}$

Stability criterion for each combination can be then derived by applying Lemma 5.4 to the new teleoperator impedance. An example will be studied in Section 5.4.

5.3.2.2 Trilateral teleoperator case

Following a similar approach, the augmented teleoperator impedance matrix can be derived for a three-port network. While a total of 35 distinct combinations exist if we consider all the termination impedance topologies mentioned so far (ISP, INP, OSP, ONP and DNP), for brevity we only report the augmented impedance matrix for one case: the three terminations are INP with SOP values of a, b, and c, respectively. The impedance matrix is

$$\begin{bmatrix} Z_{11}-a & Z_{12} & Z_{13} \\ Z_{21} & Z_{22}-b & Z_{23} \\ Z_{31} & Z_{32} & Z_{33}-c \end{bmatrix} \tag{5.13}$$

Again, stability criteria can be derived for the three-port network by applying Lemma 5.5 to the new teleoperator impedance matrix given that we have incorporated activity or excessive passivity of the terminations into the teleoperator, leaving the terminations with only passive impedances. An example will be studied in Section 5.4. Note that if the symmetrization condition (5.6) is satisfied for the original impedance teleoperator matrix (5.4), it is still satisfied for the augmented impedance matrix (5.13).

5.4 Case Studies: Application of Proposed Approach to Bilateral and Trilateral Teleoperation

In this section, we apply the proposed approach for stability analysis with non-passive operator/environment to both bilateral and trilateral teleoperation systems, although the approach described above can be used for any multi-port network. As discovered in [6], human arms can exhibit INP impedance behaviors under rigid grasping conditions. Therefore, in both bilateral and trilateral cases we consider the presence of at least one INP termination. In practice, the level of activity/passivity can be determined using a similar approach in [6] where the time-domain force and velocity data are examined and definitions in Section 5.2 are applied. Stability criteria for each case will be derived in terms of the teleoperator impedance parameters, followed by derivation of closed-form conditions on the control gains within a given control architecture. Finally experiments are

performed to verify the stability criteria. Note that although we applied the proposed approach to INP terminations only, it can be applied to any considered termination topology to derive stability conditions.

5.4.1 Bilateral teleoperation under two INP terminations

Consider a bilateral teleoperation system where the two operators acting on the master and slave robots demonstrate INP impedances of with SOP values of a and b, respectively. As discussed in 5.1 this could be the case in a telerehabilitation setting. Now by applying Lemma 5.4 to the bilateral teleoperator matrix for the INP-INP case in Table 5.1, the condition set (5.5) is revised to

$$\text{Re}(Z_{11}) \geq a$$

$$\text{Re}(Z_{22}) \geq b$$

$$2(\text{Re}(Z_{11}) - a)(\text{Re}(Z_{22}) - b) - \text{Re}(Z_{12}Z_{21}) - |Z_{12}Z_{21}| \geq 0 \qquad (5.14)$$

Note that by setting a or b to zero, the stability theorem derived in [9], where only one port is terminated to an INP termination while the other port is terminated to an arbitrarily passive termination, can be recovered. However, our approach is equally applicable to bilateral teleoperation systems with one or two active terminations.

Now consider a bilateral teleoperation system under position error based (PEB) control. For details of the control architecture, readers can refer to [26]. The impedance matrix representing the system can be expressed as:

$$\begin{bmatrix} Z_m + C_m & C_m \\ C_s & Z_s + C_s \end{bmatrix} \qquad (5.15)$$

Where, in the force-velocity domain, the master and slave robots are modeled as $Z_m = M_m s + B_m$ and $Z_s = M_s s + B_s$, and the local position controllers for the two robots are $C_m = K_{vm} + K_{pm}/s$ and $C_s = K_{vs} + K_{ps}/s$. We assume $K_{vm}, K_{vs}, K_{pm}, K_{ps} \geq 0$. Assume the operator on the master side can be characterized by an INP impedance with SOP value of a while the operator on the slave side can be characterized by an INP impedance with SOP value of b. By applying (5.4.1) to (5.15), we have the following closed-form stability condition to be satisfied involving the controller gains for a given set of robot parameters:

$$K_{vm} + B_m \geq a$$

$$K_{vs} + B_s \geq b$$

$$(K_{vm} + B_m - a)(B_s - b) + K_{vs}(B_m - a) \geq \frac{(K_{pm}K_{vs} - K_{vm}K_{ps})^2}{4K_{pm}K_{ps}} \tag{5.16}$$
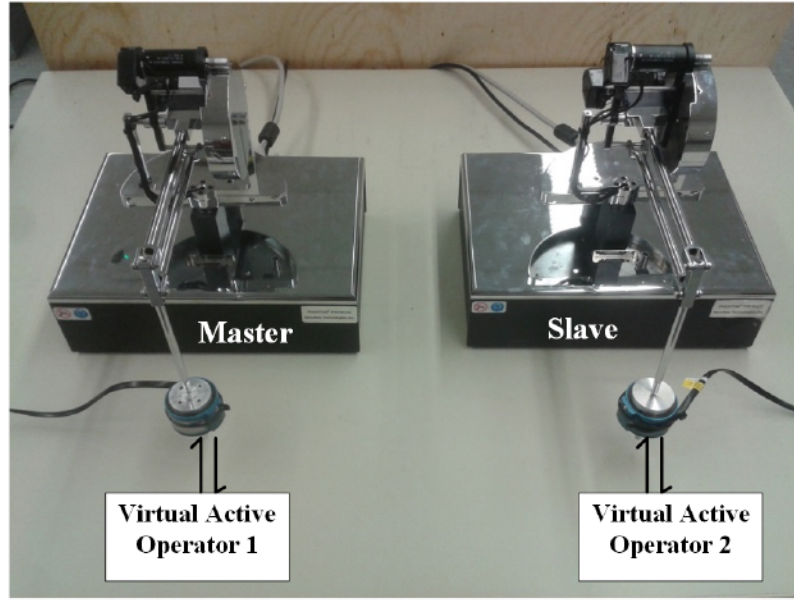
FIGURE 5.5: Bilateral teleoperation experimental setup with both the master and slave robot coupled to virtual active operators.
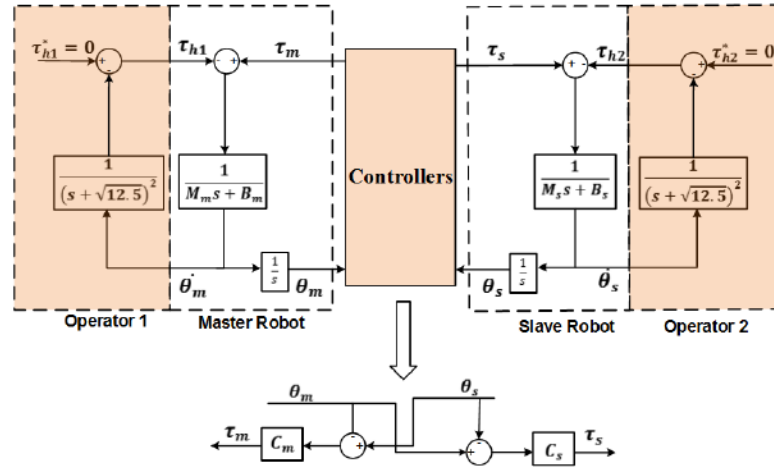
FIGURE 5.6: Schematic of the bilateral teleoperation experimental setup. The virtual systems are distinguished from physical systems by being shaded in orange.

Next, we perform experiments to compare the stability conditions derived directly from (5.5) and (5.4.1); recall that (5.4.1) led to (5.4.1) and (5.5) would lead to the same with $a = b = 0$. Bilateral

teleoperation is set up as shown in Fig. 5.5 using a pair of 3-DOF Phantom Premium 1.5A haptic devices (Geomagic Inc., Wilmington, MA, USA). Only the first joint of each robot is teleoperated, and the other two joints are controlled to be locked in place by using high-gain control. The sampling time is $1ms$. The robot dynamics are identified as mass-damper with $M_m = M_s = 0.015$ and $B_m = B_s = 0.01822$ in joint space [72]. The active operators are realized in the virtual environment with the transfer function $\frac{1}{(s+\sqrt{12.5})^2}$. The reason why we use virtual operators is that they allow us to have control over the exact SOP of each active operator, which is beneficial in verifying our stability analysis approach. Plotting the Nyquist diagram of the transfer function can show an SOP of $a = b = 0.01$ for the terminations. A detailed schematic of the experimental system is presented in Fig. 5.6, where τ and θ denote torque and angular position, respectively. Also subscripts $h1, h2, m, s$ denote operator 1, operator 2, the master and the slave respectively. Two sets of experiments are conducted, with the following control gains:

1. $K_{vm} = 0.1, K_{pm} = 20, K_{ps} = 12, K_{vs} = 0.1$;

2. $K_{vm} = 0.1, K_{pm} = 32, K_{ps} = 10, K_{vs} = 0.1$;

For the first set of control gains, both (5.5) and (5.4.1) predicted stability. As the experimental result in Fig.5.7(a) show, the bilateral teleoperation system is indeed stable in the presence of a persistent sinusoidal input of amplitude 0.08 Nm and frequency 5 rad/s. For the second set of controller gains, (5.5) predicted stability while (5.4.1) predicted instability. The experimental results in Fig.5.7 show that the robot positions in the teleoperation system diverge if we release the robots from two different initial conditions. Overall, the conclusion is that with active operators, Llewellyn's theorem cannot be used for controller design while the new approach can be.
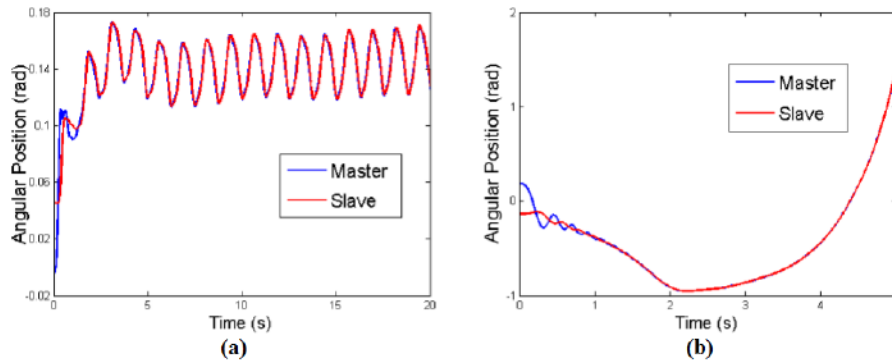
FIGURE 5.7: Bilateral master-slave joint position profiles for the first set (a) and the second set (b) of control gain.

5.4.2 Trilateral teleoperation under one INP termination

Consider a trilateral teleoperation system coupled to an active environment characterized by an INP impedance with a SOP value of c. The trilateral system considered here is a dual-user teleoperation system, consisting of two master robots and a remote environment. The two users collaboratively control a robot to perform a desired task. This type of trilateral systems is seeing emerging applications such as collaborative surgical training where a novice (operator 1) is trained by an experienced surgeon (operator 2) to perform a surgical task on the remote environment. In the case of beating heart surgery, for instance, the remote environment (the beating heart) is active, introducing the necessity of a stability analysis capable of dealing with non-passive environments in trilateral teleoperation. Also, motor complex tasks from either operator lead to activity of that termination for the trilateral teleoperator.

Using the three-port network model of the trilateral teleoperator and applying Lemma 5.5 to (5.13) while assuming the two users are passive ($a = b = 0$) but the environment is INP with a SOP value of c, conditions (5.9) and (5.11) are revised to

$$\text{Re}(Z_{33}) \geq c \tag{5.17}$$

$$2\text{Re}(Z_{11})\text{Re}(Z_{22})(\text{Re}(Z_{33}) - c)$$
$$- \text{Re}(Z_{11})(|Z_{23}Z_{32}| + \text{Re}(Z_{23}Z_{32}))$$
$$- \text{Re}(Z_{22})(|Z_{13}Z_{31}| + \text{Re}(Z_{13}Z_{31}))$$
$$- (\text{Re}(Z_{33}) - c)(|Z_{12}Z_{21}| + \text{Re}(Z_{12}Z_{21}))$$
$$+ 4\text{Re}(\sqrt{Z_{12}Z_{21}})\text{Re}(\sqrt{Z_{13}Z_{31}})\text{Re}(\sqrt{Z_{23}Z_{32}}) \geq 0 \tag{5.18}$$

As discussed in [73], the desired position for each robot is obtained by calculating the weighted sum of positions of the other two robots. The parameter α determines this weight, which can be interpreted as the relative authority of each operator over the slave robot's position. By adopting the PEB control architecture in [73] and the aforementioned complementary-linear-combination (CLC) authority sharing laws, we have the following impedance matrix representing the system:

$$\begin{bmatrix} C_{m1} + M_{m1}s & -(1-\alpha)C_{m1} & -\alpha C_{m1} \\ -\alpha C_{m2} & C_{m2} + M_{m2}s & -(1-\alpha)C_{m2} \\ -\alpha C_{ms} & -(1-\alpha)C_{ms} & C_{ms} + M_s s \end{bmatrix} \tag{5.19}$$

where the robots are modeled as $Z_{m1} = M_{m1}s$ and $Z_{m2} = M_{m2}s$ on the users side and $Z_s = M_s s$ on the environment side. Similar to the bilateral teleoperation case in Section 5.4.1, local position

controllers are $C_{m1} = K_{vm1} + K_{pm1}/s$ and $C_{m2} = K_{vm2} + K_{pm2}/s$ on the users side and $C_s = K_{vs} + K_{ps}/s$ on the environment side. We assume K_{vm1}, K_{vm2}, K_{vs}, K_{pm1}, K_{pm2}, $K_{ps} \geq 0$. Note that in order to satisfy the symmetrization condition (5.6), α has to take the value of $\frac{1}{2}$. By applying the revised Lemma 5.5 to (5.19), we can get the following *sufficient frequency-independent* stability conditions for the trilateral teleoperation system:

$$
\begin{aligned}
K_{vs} &\geq \frac{3c}{2} \\
\frac{K_{vm1}}{K_{pm1}} &= \frac{K_{vm2}}{K_{pm2}} \\
\frac{5K_{vs} - 6c - 2\sqrt{6K_{vs}^2 - 15K_{vs}c + 9c^2}}{K_{vs}} &\leq \frac{K_{vs}K_{pm2}}{K_{ps}K_{vm2}} \\
&\leq \frac{5K_{vs} - 6c + 2\sqrt{6K_{vs}^2 - 15K_{vs}c + 9c^2}}{K_{vs}}
\end{aligned}
\tag{5.20}
$$

FIGURE 5.8: Trilateral teleoperation experimental setup with the slave robot interacting with virtual active environment

Finally, we put the previously-derived theoretical stability conditions to test by performing a 1-DOF trilateral teleoperation experiment. The two Phantom Premium 1.5A haptic devices used in Section 5.4.1 are used here as the two master robots. The slave robot at the environment side is a Phantom Omni haptic device (Geomagic Inc., Wilmington, MA, USA) (Fig. 5.8). Two master robots are actuated with (human operators modeled by) persistent sinusoidal inputs of amplitude 0.07 Nm, frequency 5 rad/s and phase 1.5 rad. The active environment is implemented as a virtual environment with transfer function $\frac{1}{(s+\sqrt{1.25})^2}$, giving an SOP value of $c = 0.1$ on the remote environment. Based on (5.20), we chose the following stabilizing control gains (according to the theoretical stability condition): $K_{pm1} = 4$, $K_{vm1} = 0.1$, $K_{pm2} = 4$, $K_{vm2} = 0.1$, $K_{ps} = 8$, *and* $K_{vs} = 0.2$. The result is shown in Fig. 5.9, which shows the stability of the teleoperation system in this case.
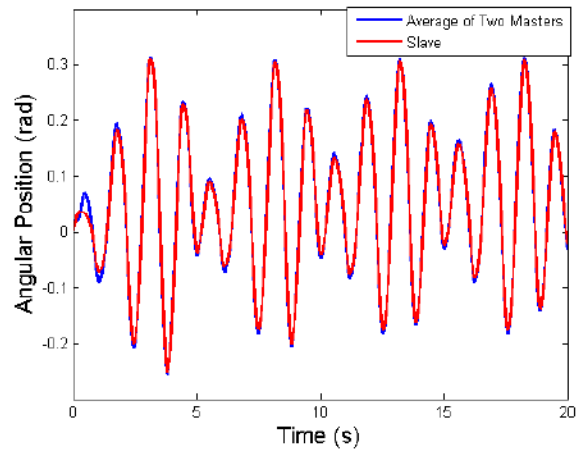
FIGURE 5.9: Robot joint positions for environment INP, dual-user PEB control.

The above demonstrates that the proposed approach can be used to provide effective controller design guidelines in the presence of active operator/environment in trilateral teleoperation.

5.5 Conclusions

In this chapter, we demonstrated the proposed series-shunt for stability analysis in the presence of strictly passive or active operators/environments for bilateral and trilateral teleoperation systems. Different from previously proposed approaches, this approach can effectively deal with strict passivity/activity in any number of terminations, easily apply to both bilateral and trilateral teleoperation, and rely solely on immittance parameters, which are relatively easy to obtain for mechanical systems. We detailed the approach for termination impedance decomposition for different impedance topologies and applied the approach to PEB bilateral and trilateral teleoperation with one or more INP terminations. Experiments were performed to verify the stability criteria and demonstrate the difference between the newly derived stability criteria and the traditional ones.

Chapter 6

Conclusions and Future Work

6.1 Conclusions

This thesis develops both practical implementations of task-oriented telerehabilitation therapy technologies aiming at partially automating the rehabilitation process and thus time-sharing a therapist. It also presents theoretical stability analysis tools for teleoperation systems with two or more human operators such as telerehabilitation systems. Remember that in the telerehabilitation context, a hospital-based therapist is haptically linked and telepresented to a home-based disabled patient in order to effectively simulate traditional in-hospital therapies, e.g., those in which a therapist physically helps and cooperates with a patient in performing therapy tasks, over a distance.

In Chapter 3, we proposed and demonstrated a novel telerehabilitation approach: The learn-and-replay (LAR) paradigm. We first introduced our experimental telerehabilitation system and a 1-DOF therapy task involving driving a woodscrew into a wooden plate held by an industrial manipulator. Robot kinematics and teleoperation control were carefully considered. Next, we introduced the therapist arm impedance identification technique, which was able to detect force perturbation onsets based on the time profile of mechanical energy absorption of the arm. The identification method had the advantage of not introducing external disturbances and not restricting the therapist's posture. Then time-delay estimation (TDE) based impedance control was introduced as an appropriate control method for our industrial manipulator. Finally, results from a successful LAR session was shown for the 1-DOF screwdriving task.

In Chapter 4, the LAR paradigm was applied to a 2-DOF peg-in-the-hole insertion task. During the therapist-in-loop (TIL) phase, the therapist held the peg still in two directions through teleoperation

so that the patient could put the hole onto the peg. The therapist's arm impedance was measured in the two directions during the TIL phase. Next the measured impedance was ajusted taking into account the teleoperation system's 2-DOF dynamics in order to obtain the desired impedance for impedance control of the slave robot during the TOOL phase. In the TOOL phase, the impedance control was successfully implemented on the slave robot and the therapist's role in the 2-DOF peg-in-the-hole insertion task was replicated by the slave robot with success. Together with Chapter 3, this showed the feasibility of the proposed LAR telerehabilitation paradigm and its potential in time-sharing a therapist and thus partly automating the rehabilitation therapy.

In Chapter 5, we first reviewed the need for a teleoperation system stability analysis approach that can take into account strict passivity or activity information of one or multiple terminations. Traditional Llewellyn's stability analysis approach requires that all terminations are passive, which can be violated in telerehabilitation as the therapist becomes active during assistive therapy. Then different termination categories were defined, including input strictly passive (ISP), output strictly passive (OSP), input non-passive (INP), output non-passive (ONP) and disk-like non-passive (DNP). We showed that the series-shunt approach can be applied to a teleoperation system involving one or more of the aforementioned terminations. Explicit stability criteria were then drawn during case studies for a bilateral teleoperation system with two INP terminations and a trilateral teleoperation system with one INP termination. The stability criteria were validated with experiments involving virtual operators. The series-shunt approach was thus shown to be able to effectively deal with strict passivity or activity in any number of terminations.

6.2 Future Work

For the proposed LAR telerehabilitation paradigm presented in Chapter 3 and Chapter 4, future work can take the following steps:

1. DEVELOPMENT OF MORE CLINICALLY RELEVANT THERAPY TASKS SUITABLE FOR THE PROPOSED LAR PARADIGM. With the involvement of therapists and clinicians, new multi-DOF tasks that are closely related to current rehabilitation practices for upper-limb rehabilitation can be designed. The tasks need to be closely related to activities of daily living (ADL). Currently candidates include

   (a) *Door opening task* where the slave robot can be equipped with a doorknob-shaped end-effector that the patient can turn with his/her their wrist while the therapist "holds" the door via teleoperation

(b) *Jar lid opening task* where the patient tries to open a jar lid held by the slave robot with the help of the therapist who uses the teleoperation system to stabilize the jar.

(c) *Vacuum cleaning task* where the patient practices vacuuming a space by manipulating the slave robot's handle-shaped end-effector, while the therapist carries the weight of the vacuum cleaner via teleoperation.

In all of these proposed tasks, during the TIL phase the therapist can provide different degrees of difficulty for the specific task by modulating his/her impedance.

2. DEVELOPMENT OF MORE SOPHISTICATED ARM IMPEDANCE IDENTIFICATION TECHNIQUES. Advanced on-line arm impedance identification can be developed in order to capture the possibly varying impedance of the therapist's arm over a spatial trajectory such that tasks that require different impedance characteristics of the therapist's arm or significant arm displacements can also be incorporated into the proposed LAR paradigm.

3. CLINICAL STUDIES. After achieving the previous two goals and making sure that a reliable LAR system both in software and hardware is built, clinical patient-oriented studies can be carried out to study the usefulness of the proposed paradigm in real clinical settings. Patient and therapist user experience, as well as LAR system reliability for various tasks will be the focus of clinical studies.

For the telerehabilitation stability analysis with termination activity/strict passivity work presented in Chapter 5, future work can be performed in the following directions:

1. USE OF PHYSICAL SYSTEMS FOR EXPERIMENTAL VALIDATION. The implemented active virtual operators can be replaced with robots under impedance control, so that we have a physical energetically active system demonstrating desired active impedances. Such experiments will provide more convincing evidence of the practical value of our proposed stability analysis approach in dealing with real physical systems.

2. IMPLICATIONS OF IMPROVED STABILITY ANALYSIS ON TELEOPERATION TRANSPARENCY AND THUS HUMAN TASK PERFORMANCE. To further demonstrate the usefulness of our stability analysis, studies can be done with regard to the impact of relaxed stability conditions on teleoperation task performance in the presence of strictly passive terminations.

3. MULTI-DOF MULTI-LATERAL SYSTEMS. Although Chapter 5 only considered 1-DOF robots, which can only engage in 1-DOF teleoperation tasks, the proposed series-shunt approach can be extended into multilateral teleoperation systems with *multi-DOF* robots. Such studies will further enrich the series-shunt approach.

Bibliography

[1] H. Krebs and N. Hogan, "Therapeutic robotics: a technology push," *Proceedings of the IEEE*, vol. 94, no. 9, pp. 1727–1738, Sept 2006.

[2] T. Andersson, J. Fredlund, E. Hastad, D. Härensten, J. Karlsson, M. Leterius, H. Lundberg, and T. Sreand, "Rehabliteringsstation för strokepatienter," *Virtuella världar och haptika gränssnitt för rehabilitering i hemmet. Projekt Produktutveckling, Produktion och produktionsutveckling, Chalmers Tekniska Högskola tillsammans med Högskolan för Design och Konstverk, Göteborg*, 2003.

[3] P. F. Hokayem and M. W. Spong, "Bilateral teleoperation: An historical survey," *Automatica*, vol. 42, no. 12, pp. 2035 – 2057, 2006.

[4] R. Tao and M. Tavakoli, "Multilateral haptic system stability analysis: The effect of activity or passivity of terminations via a series-shunt approach," in *Haptics Symposium (HAPTICS), 2014 IEEE*, Feb 2014, pp. 203–208.

[5] Z. Xiu, A. Kitagawa, H. Tsukagoshi, C. Liu, and M. Ido, "Internet-based tele-rehabilitatioon system–bilateral tele-control with variable time delay," in *IEEE/RSJ International Conference on Intelligent Robots and Systems*. IEEE, 2006, pp. 5208–5213.

[6] M. Dyck, "Measuring the dynamic impedance of the human arm," Master's thesis, University of Alberta, 2013.

[7] M. S. Erden and A. Billard, "End-point impedance measurements at human hand during interactive manual welding with robot," in *Robotics and Automation (ICRA), 2014 IEEE International Conference on*, May 2014, pp. 126–133.

[8] L. Rozo, S. Calinon, D. Caldwell, P. Jiménez, and C. Torras, "Learning collaborative impedance-based robot behaviors," in *AAAI Conference on Artificial Intelligence*, 2013, pp. 1422–1428.

[9] A. Jazayeri and M. Tavakoli, "Revisiting Llewellyn's absolute stability criterion for bilateral teleoperation systems under non-passive operator or environment," in *Proceedings of the 2012 IEEE/RSJ International Conference on Intelligent Robots and Systems (IROS)*, vol. 1, Vilamoura, Portugal, 2012, pp. 70–75.

[10] A. Jazayeri, M. Dyck, and M. Tavakoli, "Stability analysis of teleoperation systems under strictly passive and non-passive operator," in *Proceedings of the IEEE World Haptics Conference 2013*, Daejeon, Korea, 2013.

[11] A. Haddadi and K. Hashtrudi-Zaad, "Bounded-impedance absolute stability of bilateral teleoperation control systems," *IEEE Transactions on Haptics*, vol. 3, no. 1, pp. 15–27, 2010.

[12] R. Adams and B. Hannaford, "A two-port framework for the design of unconditionally stable haptic interfaces," in *Intelligent Robots and Systems, 1998. Proceedings., 1998 IEEE/RSJ International Conference on*, vol. 2, 1998, pp. 1254–1259 vol.2.

[13] T. Sheridan, "Telerobotics," *Automatica*, vol. 25, no. 4, pp. 487 – 507, 1989.

[14] R. C. Goertz and W. M. Thompson, "Electronically controlled manipulator," *Nucleonics (US) Ceased publication*, vol. 12, 1954.

[15] W. R. Ferrell, "Remote manipulation with transmission delay," *Human Factors in Electronics, IEEE Transactions on*, no. 1, pp. 24–32, 1965.

[16] B. Hannaford, "A design framework for teleoperators with kinesthetic feedback," *IEEE Transactions on Robotics and Automation*, vol. 5, pp. 426–434, 1989.

[17] G. Niemeyer and J.-J. Slotine, "Stable adaptive teleoperation," *Oceanic Engineering, IEEE Journal of*, vol. 16, no. 1, pp. 152–162, 1991.

[18] R. Lozano, N. Chopra, and M. W. Spong, "Passivation of force reflecting bilateral teleoperators with time varying delay," in *Proceedings of the 8. Mechatronics Forum*, 2002, pp. 954–962.

[19] P. Berestesky, N. Chopra, and M. W. Spong, "Discrete time passivity in bilateral teleoperation over the internet," in *Robotics and Automation, 2004. Proceedings. ICRA'04. 2004 IEEE International Conference on*, vol. 5.   IEEE, 2004, pp. 4557–4564.

[20] C. Secchi, S. Stramigioli, and C. Fantuzzi, "Digital passive geometric telemanipulation," in *ICRA*, 2003, pp. 3290–3295.

[21] G. Hirzinger, B. Brunner, J. Dietrich, and J. Heindl, "Sensor-based space robotics-rotex and its telerobotic features," *Robotics and Automation, IEEE Transactions on*, vol. 9, no. 5, pp. 649–663, 1993.

[22] P. Desbats, F. Geffard, G. Piolain, and A. Coudray, "Force-feedback teleoperation of an industrial robot in a nuclear spent fuel reprocessing plant," *Industrial Robot: An International Journal*, vol. 33, no. 3, pp. 178–186, 2006.

[23] M. Utsumi, T. Hirabayashi, and M. Yoshie, "Development for teleoperation underwater grasping system in unclear environment," in *Underwater Technology, 2002. Proceedings of the 2002 International Symposium on.* IEEE, 2002, pp. 349–353.

[24] G. Guthart and J. K. Salisbury Jr, "The intuitivetm telesurgery system: Overview and application." in *ICRA*, 2000, pp. 618–621.

[25] M. Ghodoussi, S. E. Butner, and Y. Wang, "Robotic surgery-the transatlantic case," in *Robotics and Automation, 2002. Proceedings. ICRA'02. IEEE International Conference on*, vol. 2. IEEE, 2002, pp. 1882–1888.

[26] M. Tavakoli, A. Aziminejad, R. Patel, and M. Moallem, "High-fidelity bilateral teleoperation systems and the effect of multimodal haptics," *IEEE Transactions on Systems, Man and Cybernetics – Part B*, vol. 37, no. 6, pp. 1512–1528, December 2007.

[27] W. Seamone and G. Schmeisser, "Early clinical evaluation of a robot arm/worktable system for spinal-cord-injured persons." *Journal of rehabilitation research and development*, vol. 22, no. 1, pp. 38–57, 1985.

[28] D. Khalili and M. Zomlefer, "An intelligent robotic system for rehabilitation of joints and estimation of body segment parameters," *IEEE Transactions on Biomedical Engineering*, vol. 35, no. 2, pp. 138–146, 1988.

[29] M. P. Dijkers and P. C. deBear, "Patient and staff acceptance of robotic technology in occupational therapy: A pilot study." *Journal of Rehabilitation Research & Development*, vol. 28, no. 2, p. 33, 1991.

[30] P. S. Lum, C. G. Burgar, and P. C. Shor, "Evidence for improved muscle activation patterns after retraining of reaching movements with the mime robotic system in subjects with post-stroke hemiparesis," *Neural Systems and Rehabilitation Engineering, IEEE Transactions on*, vol. 12, no. 2, pp. 186–194, 2004.

[31] D. J. Reinkensmeyer, L. E. Kahn, M. Averbuch, A. McKenna-Cole, B. D. Schmit, and W. Z. Rymer, "Understanding and treating arm movement impairment after chronic brain injury: progress with the arm guide," *Journal of rehabilitation research and development*, vol. 37, no. 6, pp. 653–662, 2000.

[32] G. Colombo, M. Joerg, R. Schreier, V. Dietz *et al.*, "Treadmill training of paraplegic patients using a robotic orthosis," *Journal of rehabilitation research and development*, vol. 37, no. 6, pp. 693–700, 2000.

[33] J. E. Deutsch, J. Latonio, G. C. Burdea, and R. Boian, "Post-stroke rehabilitation with the rutgers ankle system: a case study," *Presence: Teleoperators and Virtual Environments*, vol. 10, no. 4, pp. 416–430, 2001.

[34] D. J. Williams, H. I. Krebs, and N. Hogan, "A robot for wrist rehabilitation," in *Engineering in Medicine and Biology Society, 2001. Proceedings of the 23rd Annual International Conference of the IEEE*, vol. 2.   IEEE, 2001, pp. 1336–1339.

[35] T. Worsnopp, M. Peshkin, J. Colgate, and D. Kamper, "An actuated finger exoskeleton for hand rehabilitation following stroke," in *IEEE 10th International Conference on Rehabilitation Robotics (ICORR)*.   IEEE, 2007, pp. 896–901.

[36] B. Volpe, H. Krebs, N. Hogan, L. Edelsteinn, C. Diels, and M. Aisen, "Robot training enhanced motor outcome in patients with stroke maintained over 3 years," *Neurology*, vol. 53, no. 8, pp. 1874–1874, 1999.

[37] P. S. Lum, C. G. Burgar, P. C. Shor, M. Majmundar, and M. Van der Loos, "Robot-assisted movement training compared with conventional therapy techniques for the rehabilitation of upper-limb motor function after stroke," *Archives of physical medicine and rehabilitation*, vol. 83, no. 7, pp. 952–959, 2002.

[38] J. Hidler, D. Nichols, M. Pelliccio, K. Brady *et al.*, "Advances in the understanding and treatment of stroke impairment using robotic devices," *Top Stroke Rehabil*, vol. 12, no. 2, pp. 22–35, 2005.

[39] L. E. Kahn, P. S. Lum, W. Z. Rymer, and D. J. Reinkensmeyer, "Robot-assisted movement training for the stroke-impaired arm: Does it matter what the robot does?" *Journal of rehabilitation research and development*, vol. 43, no. 5, p. 619, 2006.

[40] H. Van der Loos and D. Reinkensmeyer, "Rehabilitation and health care robotics," in *Springer Handbook of Robotics*, B. Siciliano and O. Khatib, Eds.   Springer Berlin Heidelberg, 2008, pp. 1223–1251.

[41] C. R. Carignan and H. I. Krebs, "Telerehabilitation robotics: bright lights, big future?" *Journal of rehabilitation research and development*, vol. 43, no. 5, p. 695, 2006.

[42] V. G. Popescu, G. C. Burdea, M. Bouzit, and V. R. Hentz, "A virtual-reality-based telerehabilitation system with force feedback," *Information Technology in Biomedicine, IEEE Transactions on*, vol. 4, no. 1, pp. 45–51, 2000.

[43] C. R. Carignan and P. A. Olsson, "Cooperative control of virtual objects over the internet using force-reflecting master arms," *in Proccedings of IEEE International Conference on Robobotics and Automation*, vol. 2, pp. 1221–1226, 2004.

[44] S. F. Atashzar, I. G. Polushin, and R. V. Patel, "Networked teleoperation with non-passive environment: Application to tele-rehabilitation," in *2012 IEEE/RSJ International Conference on Intelligent Robots and Systems (IROS)*.   IEEE, 2012, pp. 5125–5130.

[45] M. Shahbazi, S. F. Atashzar, and R. V. Patel, "A framework for supervised robotics-assisted mirror rehabilitation therapy," in *2014 IEEE/RSJ International Conference on Intelligent Robots and Systems (IROS)*, 2014, pp. 3567–3572.

[46] S. M. McLean, M. Burton, L. Bradley, and C. Littlewood, "Interventions for enhancing adherence with physiotherapy: a systematic review," *Manual Therapy*, vol. 15, no. 6, pp. 514–521, 2010.

[47] D. W. Franklin, R. Osu, E. Burdet, M. Kawato, and T. E. Milner, "Adaptation to stable and unstable dynamics achieved by combined impedance control and inverse dynamics model," *Journal of neurophysiology*, vol. 90, no. 5, pp. 3270–3282, 2003.

[48] E. Burdet, R. Osu, D. W. Franklin, T. E. Milner, and M. Kawato, "The central nervous system stabilizes unstable dynamics by learning optimal impedance," *Nature*, vol. 414, no. 6862, pp. 446–449, 2001.

[49] A. Ajoudani, N. G. Tsagarakis, and A. Bicchi, "Tele-impedance: Towards transferring human impedance regulation skills to robots," in *2012 IEEE International Conference on Robotics and Automation (ICRA)*.   IEEE, 2012, pp. 382–388.

[50] F. A. Mussa-Ivaldi, N. Hogan, and E. Bizzi, "Neural, mechanical, and geometric factors subserving arm posture in humans," *The Journal of Neuroscience*, vol. 5, no. 10, pp. 2732–2743, 1985.

[51] H. Gomi, Y. Koike, and M. Kawato, "Human hand stiffness during discrete point-to-point multi-joint movement," in *Engineering in Medicine and Biology Society, 1992 14th Annual International Conference of the IEEE*, vol. 4, Oct 1992, pp. 1628–1629.

[52] J. M. Dolan, M. B. Friedman, and M. L. Nagurka, "Dynamic and loaded impedance components in the maintenance of human arm posture," *Systems, Man and Cybernetics, IEEE Transactions on*, vol. 23, no. 3, pp. 698–709, 1993.

[53] I. L. Kurtzer, J. A. Pruszynski, and S. H. Scott, "Long-latency reflexes of the human arm reflect an internal model of limb dynamics," *Current Biology*, vol. 18, no. 6, pp. 449–453, 2008.

[54] M. W. Spong, S. Hutchinson, and M. Vidyasagar, *Robot modeling and control*.   Wiley New York, 2006, vol. 3.

[55] C. Canudas de Wit, H. Olsson, K. Aström, and P. Lischinsky, "A new model for control of systems with friction," *IEEE Transactions on automatic control*, vol. 40, no. 3, pp. 419–425, 1995.

[56] M. R. Kermani, R. V. Patel, and M. Moallem, "Friction identification and compensation in robotic manipulators," *Instrumentation and Measurement, IEEE Transactions on*, vol. 56, no. 6, pp. 2346–2353, 2007.

[57] J. W. Jeong, P. H. Chang, and K. B. Park, "Sensorless and modeless estimation of external force using time delay estimation: application to impedance control," *Journal of Mechanical Science and Technology*, vol. 25, no. 8, pp. 2051–2059, 2011.

[58] M. Dyck and M. Tavakoli, "Measuring the dynamic impedance of the human arm without a force sensor," in *13th Int. Conf. Rehabilitation Robotics*, 2013.

[59] S. F. Atashzar, A. Saxena, M. Shahbazi, and R. V. Patel, "Involuntary movement during haptics-enabled robotic rehabilitation: Analysis and control design," in *2014 IEEE/RSJ International Conference on Intelligent Robots and Systems (IROS)*, 2014.

[60] S. Haykin, *Active Network Theory*.   Reading, MA: Addison-Wesley, 1970.

[61] F. B. Llewellyn, "Some fundamental properties of transmission systems," *Proceedings of the IRE*, vol. 40, no. 3, pp. 271–283, 1952.

[62] K. Hashtrudi-Zaad and S. E. Salcudean, "Analysis of control architectures for teleoperation systems with impedance/admittance master and slave manipulators," *International Journal of Robotics Research*, vol. 20, no. 6, pp. 419–445, 2001.

[63] S. Nudehi, R. Mukherjee, and M. Ghodoussi, "A shared-control approach to haptic interface design for minimally invasive telesurgical training," *IEEE Transactions on Control Systems Technology*, vol. 13, no. 4, pp. 588–592, 2005.

[64] W. Lo, Y. Liu, I. Elhajj, N. Xi, Y. Wang, and T. Fukuda, "Cooperative teleoperation of a multirobot system with force reflection via internet," *IEEE/ASME Transactions on Mechatronics*, vol. 9, no. 4, pp. 661–670, 2004.

[65] J. Li, M. Tavakoli, and Q. Huanq, "Stability analysis of trilateral haptic collaboration," in *World Haptics Conference (WHC), 2013*, 2013, pp. 611–616.

[66] N. Hogan, "Controlling impedance at the man/machine interface," in *Proceedings of IEEE International Conference on Robotics and Automation*, 1989, pp. 1626–1631 vol.3.

[67] ——, "The mechanics of multi-joint posture and movement control," *Biological Cybernetics*, vol. 52, pp. 315–331, 1985.

[68] H. J. Marquez, *Nonlinear Control Systems Analysis and Design*. Wiley, 2003.

[69] R. Adams and B. Hannaford, "Control law design for haptic interfaces to virtual reality," *IEEE Transactions on Control Systems Technology*, vol. 10, no. 1, pp. 3–13, January 2002.

[70] R. Lozano, B. Maschke, B. Brogliato, and O. Egeland, *Dissipative Systems Analysis and Control: Theory and Applications*. Secaucus, NJ, USA: Springer-Verlag New York, Inc., 2007.

[71] N. Levinson and R. M. Redheffer, *Complex Variables*. McGraw-Hill, 1970.

[72] A. Jazayeri and M. Tavakoli, "A passivity criterion for sampled-data bilateral teleoperation systems," *IEEE Transactions on Haptics*, vol. 6, no. 3, pp. 363–369, 2013.

[73] B. Khademian and K. Hashtrudi-Zaad, "Shared control architectures for haptic training: Performance and coupled stability analysis," *The International Journal of Robotics Research*, vol. 30, pp. 1627–1642, 2011.

[74] J. J. Craig, *Introduction to Robotics: Mechanics and Control*. Pearson/Prentice Hall Upper Saddle River, NJ, USA:, 2005.

Appendix A

Yaskawa Motoman SIA5F Robot Kinematics

In this Appendix we first detail the Yaskawa Motoman SIA5F original robot kinematics. Its dimensions, link frames and Denavit-Hartenberg(DH) parameters will be presented in Section A.1. Then we will derive a simplified version from the full kinematics, with which we will derive the inverse kinematics used in Section 4.2 of Chapter 4 to jog the slave robot to a *specified* home position.

A.1   SIA5F dimensions and DH parameters

The detailed dimensions of the Motoman SIA5F robot is shown in Fig. A.1(a), taken from the product manual. This is the robot's *default* home position (different from the home position that we defined in Chapter 3 and Chapter 4). The length measurements are in *mm*. DH frames are attached to the robot according to [74]. The frames are shown in Fig. A.1(b). Based on the DH frames and the robot dimensions, we can derive the DH parameters for this home position shown in Table A.1.

Now based on the robot's home position, let's define for each axis i, the joint rotation angle to be q_i in degrees. Orientations for some of these joint angles are shown in Fig. A.1. Taking this into account, we can have the DH parameters for all configurations allowed by the robot's workspace shown in Table A.2.

TABLE A.1: Denavit-Hartenberg parameters for the Motoman SIA5F robot at its home position

i	α_{i-1} (rad)	a_{i-1} (mm)	d_i mm	θ_i (rad)
1	0	0	0	0
2	$\frac{\pi}{2}$	0	0	0
3	$-\frac{\pi}{2}$	0	270	0
4	$\frac{\pi}{2}$	85	0	$\frac{\pi}{2}$
5	$\frac{\pi}{2}$	60	275	0
6	$-\frac{\pi}{2}$	0	0	0
7	$\frac{\pi}{2}$	0	145	0

TABLE A.2: Denavit-Hartenberg parameters for the Motoman SIA5F robot at its home position

i	α_{i-1} (rad)	a_{i-1} (mm)	d_i mm	θ_i (rad)
1	0	0	0	q_1
2	$\frac{\pi}{2}$	0	0	q_2
3	$-\frac{\pi}{2}$	0	270	q_3
4	$\frac{\pi}{2}$	85	0	$\frac{\pi}{2}+q_4$
5	$\frac{\pi}{2}$	60	275	q_5
6	$-\frac{\pi}{2}$	0	0	q_6
7	$\frac{\pi}{2}$	0	145	q_7

FIGURE A.1: Illustration of (a) dimensions of the Motoman SIA5F robot (b) SIA5F robot with Denavit-Hartenberg frames attached to it.
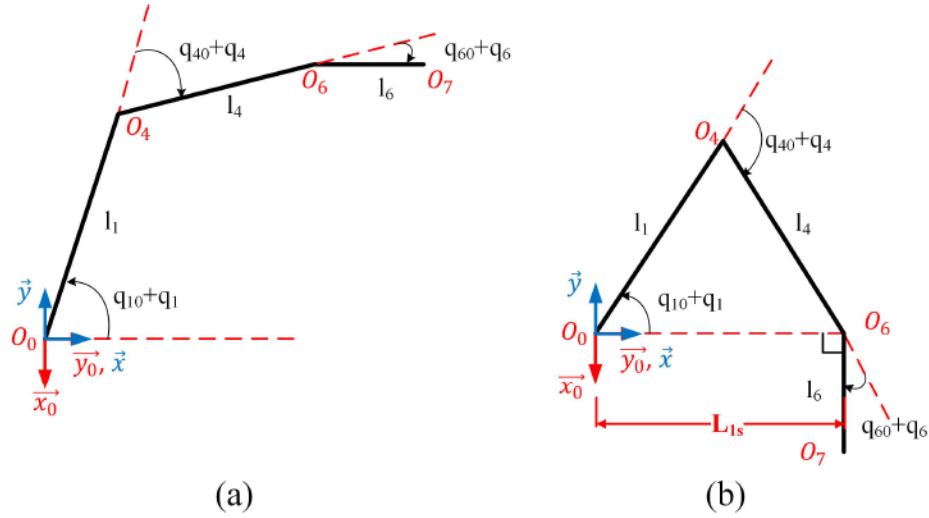
FIGURE A.2: Illustration of the "put down" Motoman robot in the $\vec{x}_0$ and $\vec{y}_0$ plane (a) before moving joint 1, 4 and 6 (b) after moving to the specified home position detailed in Section 4.2 of Chapter 4

A.2 Inverse Kinematics For a Specified Home Position in Section 4.2 of Chapter 4

In order to get the Motoman SIAF5 robot into the configuration shown in Fig. 4.2(b), we first take q_2 to be 90° and q_3 to be 90° to "put down" the Motoman robot into the plane formed by $\vec{x}_0$ and $\vec{y}_0$. From now on we lock the joint angles of q_2 and q_3 and q_5 at their current values and only actuate q_1, q_4 and q_6 to move the robot into the desired home position as shown in Fig. 4.2(b). Now the slave robot's geometry in the $\vec{x}_0$ and $\vec{y}_0$ plane can be shown in Fig. A.2(a). We define the distance between O_0 and O_4 in this plane to be l_1 (while the distance in the $\vec{z}_0$ direction is ignored), the distance between O_4 and O_6 to be l_4 and the distance between O_6 and O_7 to be l_6. From Fig. A.1(a) and Table A.1 we have

$$l_1 = \sqrt{270^2 + 85^2} = 283.06 \ mm \tag{A.1}$$

$$l_4 = \sqrt{60^2 + 270^2} = 276.59 \ mm \tag{A.2}$$

$$l_6 = 145 \ mm \tag{A.3}$$

$$\tag{A.4}$$

Next we denote the angles from l_1 to $\vec{y}_0$ to be $q_{10} + q_1$, from l_1 to l_4 to be $q_{40} + q_4$ and from l_4 to l_7 to be $q_{60} + q_6$. q_{10}, q_{40} and q_{60} are the values of these angles just after putting down the robot, before any changes are applied to the joint angles of joint 1, 4 and 6. Therefore in the configuration

of Fig. A.2(a), $q_1 = q_4 = q_6 = 0$. From the robot dimensions shown in Fig. A.1(a), we have

$$q_{10} = cos^{-1}(\frac{85}{l_1}) = 1.27 \ rad \tag{A.5}$$

$$q_{40} = -cos^{-1}(\frac{60}{l_4}) + (\frac{\pi}{2} - q_{10}) = -1.05 \ rad \tag{A.6}$$

$$q_{60} = 0 - q_{10} - q_{40} = -0.22 \ rad \tag{A.7}$$

Now the objective is to find q_1, q_4 and q_6 such that the robot is arranged in the specified home position in Section 4.2 of Chapter 4, illustrated in Fig. A.2(b).

Now we introduce a new base frame, $\vec{x}$ and $\vec{y}$ which is obtained by rotating the $\vec{x}_0$ and $\vec{y}_0$ frame around O_0 counter clockwise $90°$. The position of point O_6 in the *vecx* and *vecy* plane, $(x, y)^T$, can be expressed as

$$x = l_1 \cdot cos(q_1 + q_{10}) + l_4 \cdot cos(q_1 + q_{10} + q_4 + q_{40}) \tag{A.8}$$

$$y = l_1 \cdot sin(q_1 + q_{10}) + l_4 \cdot sin(q_1 + q_{10} + q_4 + q_{40}) \tag{A.9}$$

Let $cos(q_1 + q_{10}) = c_1$, $cos(q_4 + q_{40}) = c_4$, $cos(q_1 + q_{10} + q_4 + q_{40}) = c_{14}$, $sin(q_1 + q_10) = s_1$, $sin(q_4 + q_40) = s_4$ and $sin(q_1 + q_{10} + q_4 + q_{40}) = s_{14}$. We have

$$x^2 + y^2 = l_1^2 + l_4^2 + 2 \cdot l_1 l_4 c_4 \tag{A.10}$$

from which we can derive

$$c_4 = \frac{x^2 + y^2 - l_1^2 - l_4^2}{2 \cdot l_1 l_4} \tag{A.11}$$

$$s_4 = -\sqrt{1 - c_2^2} \tag{A.12}$$

Note that s_4 is negative because as can be seen in Fig. A.2, $q_4 + q_{40}$ is always negative. Finally we have

$$q_4 = atan2(s_2, c_2) - q_{40} \tag{A.13}$$

given x and y.

Now let's find q_1 as a function of x and y as well. (A.8) and (A.9) can be rearranged into

$$x = k_1 c_1 - k_2 s_1 \tag{A.14}$$

$$y = k_1 s_1 + k_2 c_1 \tag{A.15}$$

where

$$k_1 = l_1 + l_4 c_4 \tag{A.16}$$

$$k_2 = l_4 s_4 \tag{A.17}$$

Take $r = \sqrt{k_1^2 + k_2^2}$ and $\gamma = atan2(k2, k1)$, we can parameterize k_1 and k_2 as

$$k_1 = r \cdot cos(\gamma) \tag{A.18}$$

$$k_2 = r \cdot sin(\gamma) \tag{A.19}$$

Then (A.14) and (A.15) can be written as

$$\frac{x}{r} = cos(\gamma + q_1 + q_{10}) \tag{A.20}$$

$$\frac{y}{r} = sin(\gamma + q_1 + q_{10}) \tag{A.21}$$

Therefore,

$$q_1 + q_{10} = atan2(\frac{y}{r}, \frac{x}{r}) - \gamma = atan2(y, x) - atan2(k_2, k_1) \tag{A.22}$$

Finally, q_1 can be expressed as

$$q_1 = atan2(y, x) - atan2(l_4 s_4, \, l_1 + l_4 c_4) - q_{10} \tag{A.23}$$

From the illustration in Fig. A.2(b), we can see that l_6 is perpendicular to $\vec{y}_0$. Therefore,

$$q_6 = -\frac{\pi}{2} - q_1 - q_4 \tag{A.24}$$

Given the description in Section 4.2 of Chapter 4, the specified home position is $(x, y)^T = (L_{1s}, 0)^T = (254 \, mm, 0)^T$. By applying the numerical values into (A.13), (A.23) and (A.24), we obtain finally $q_4 = -1.1525$, $q_1 = -0.1887$, $q_6 = -0.2296$.

To recapitulate, the Motoman SIA5F robot can be arranged into the specified home position (in comparison with its default home position) in Section 4.2 of Chapter 4 by taking the joint angles in Table A.3.

TABLE A.3: Joint angles that move the Motoman SIA5F robot into the specified home position in Section 4.2 of Chapter 4

q_i	value (rad)
q_1	-0.1887
q_2	$\dfrac{\pi}{2}$
q_3	$\dfrac{\pi}{2}$
q_4	- 1.1525
q_5	0
q_6	- 0.2296
q_7	0

Appendix B

Teleoperation System Detailed Layout

In this appendix we show the detailed layout of our teleoperation system in Fig. B.1, which represents the information flow between different software and hardware with arrows. Data exchanged through the Ethernet network flow through the "Ethernet switch" block. The Ethernet network is based on UDP protocol and can be realized in C++ using Winsock API with the class that is provided in Appendix C.

The master robot is controlled via the custom built Quanser rehabilitation robot controller that handles the analog signals from/to the robot on one hand and digital signals to/from the Quarc robot control application software on the other hand. The Quarc robot control application is written in the Quarc software, which is developed by Quanser Inc. On the same PC that we name "Quanser PC", a C++ communication application receives data from the force sensor mounted on the master robot and from the SIA5F robot control application on the Agile Planet PC. It then relays those data to Quarc robot control application via shared memory for master robot control. It also receives the master robot's position data via shared memory from Quarc robot control application and relays that via UDP to the Agile Planet PC.

On the Agile Planet PC, the CPU is divided between two separate operating systems: WinCE system and Win7 system. WinCE system is in charge of controlling the Motoman SIA5F robot via communicating with the servo packs. It also reads the slave robot force sensor data via UDP and sends the robot positions together with the force sensor data to the C++ communication application on the Quanser PC. Slave robot control programs that are run in WinCE system are developed in Win7 System. It is linked to the WinCE system via a virtual machine framework and thus allows users to interact with the programs on WinCE system during execution.
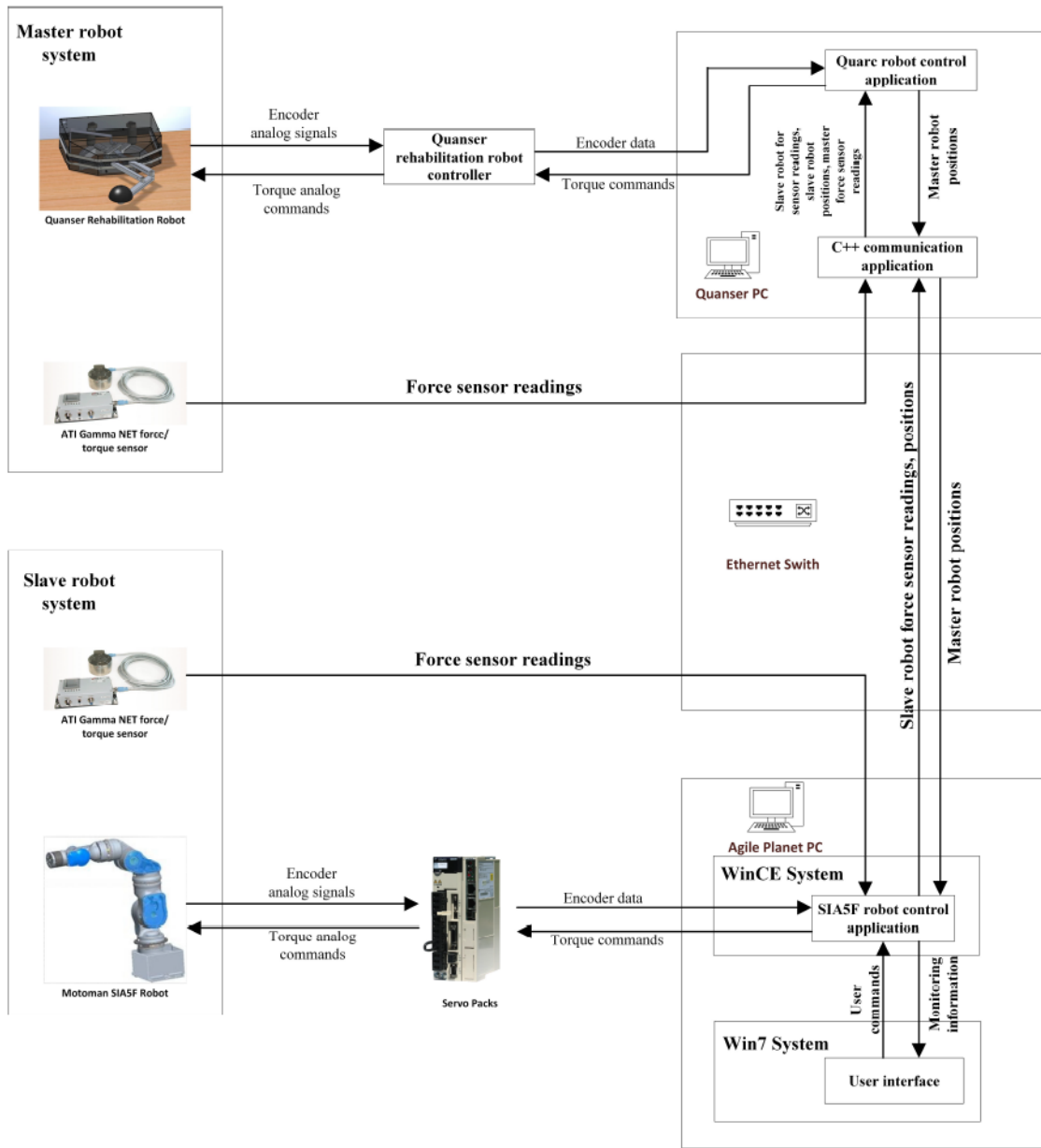
FIGURE B.1: Teleoperation system layout

The entire system runs at 1kHz.

Appendix C

C++ Code For UDP Communication

The following "UDP" class based on the Windows Winsock API is used for building the Ethernet network for teleoperation. It is used to exchange data between the ATI Gamma Net force sensors, the WinCE machine, and the Quanser PC (see Appendix B).

```cpp
ifdef WIN32
typedef int socklen_t;
#include <Winsock2.h>
#endif

#ifdef WINCE
typedef int socklen_t;
#include <Winsock2.h>
#endif

#include <string>


#define NO_FLAGS_SET 0

 class UDP
  {
  public:
    UDP(unsigned short _portNo,  const std::string _destIP, const
   std::string _localIP);
    ~UDP();
    virtual int Initialize();
    int Disconnect();
   void InitializeAsyncEventAndSelect();
   int Send (char* data, unsigned int length);
   int Recv (char* data, unsigned int length);
   int RecvNonblocking(char* data, unsigned int length, unsigned int
   timeout);
```

```cpp
    unsigned int GetPortNumber() const
    {
      return portNo;
    }
    SOCKET  GetSocket() const
    {
      return Socket;
    }
   std::string  GetIP() const
    {
      return destIP;
    }
  protected:
    unsigned short     portNo;
    SOCKET             Socket;
   HANDLE            hWSAEvent;
   std::string       localIP, destIP;
   unsigned long     destAddr, localAddr;
   SOCKADDR_IN       destSockAddr, localSockAddr;
   int               slen;  //size of destSockAddr
  };


/////////////////////////////////////////////////////////////////////////////
//
// Methods for UDP connection
//
/////////////////////////////////////////////////////////////////////////////

#include "UDP.h"
#include <iostream>


#define MSG_WAITALL 0x8
#define NAGLE_OFF

  void DisplayError(const std::string&);

  void DisplayError(const std::string& errString)
  {
     std::cout << "UDP Communication Error : " << errString <<
   std::endl;
  }



   /////////////////////////////////////////////////////////////////////////////
  //Method declarations for UDP class

   /////////////////////////////////////////////////////////////////////////////

  //constructor, assign port number and destination IP address in the
   string format
```

```cpp
UDP::UDP(unsigned short _portNo,  const std::string _destIP, const
 std::string _localIP)
{
  portNo = _portNo;
 destIP = _destIP;
 destAddr = inet_addr(_destIP.c_str());
 localIP = _localIP;
 localAddr = inet_addr(_localIP.c_str());
}

//close socket, returns 1 if succeeded, -1 if failed
int UDP::Disconnect()
{
  int retVal = 1;
  retVal = closesocket(Socket);
  if(retVal == -1)
    {
      //DisplayError("UDP::Disconnect, error during close\n");
      return 0;
    }
  return retVal;
}

//destructor, closes socket and cleanup WSA
UDP::~UDP()
{
  Disconnect();
  #ifdef WIN32
  if(WSACleanup() == SOCKET_ERROR){
   DisplayError("UDP::~UDP, WSACleanup failed\n");
  }
  #endif
}

//initializes WSADATA, UDP socket
int UDP::Initialize()
{

  WSADATA   Data;
  int status = WSAStartup(MAKEWORD(2,2), &Data);
  if(status != 0)
  {
      DisplayError("WSAStartup unsuccessful\n");
      return -1;
  }
  //setup destination address structure
  //memcpy(&destSockAddr.sin_addr, &destAddr, sizeof(destAddr));
  destSockAddr.sin_addr.s_addr = destAddr;
  destSockAddr.sin_family = AF_INET;
   destSockAddr.sin_port = htons(portNo);
  //get address size
  slen = sizeof(destSockAddr);
```

```cpp
//create socket
Socket = socket (AF_INET, SOCK_DGRAM, IPPROTO_UDP);
if (Socket == INVALID_SOCKET)
{
    int WSErrorCode = WSAGetLastError();
    std::cout << "WSErrorCode = " << WSErrorCode << std::endl;
    DisplayError("UDP::Initialize failed on socket creation \n");
    return -1;
}

//memcpy(&localSockAddr.sin_addr, &localAddr, sizeof(localAddr));
localSockAddr.sin_addr.s_addr = localAddr;
localSockAddr.sin_family = AF_INET;
localSockAddr.sin_port = htons(portNo);
slen = sizeof(destSockAddr);


//bind
if (bind(Socket, (struct sockaddr *) &localSockAddr,
 sizeof(SOCKADDR_IN)) == SOCKET_ERROR)
{
    DisplayError("UDPServer: Initialize failed on binding\n");
    closesocket(Socket);
    return -1;
}
  return 1;
}

void UDP::InitializeAsyncEventAndSelect()
{
    hWSAEvent = WSACreateEvent();
    if (NULL == hWSAEvent)
    {
        printf("UDP AsyncEvent: Failed to create Event. Err =
 %u\r\n", WSAGetLastError());
    }
    else
    {
        if (SOCKET_ERROR == WSAEventSelect(Socket, hWSAEvent,
 FD_WRITE|FD_READ|FD_CLOSE)) //FD_READ: recv, FD_WRITE: send
        {
            printf("AyncSocketComms: Failed to select. Err =
 %u\r\n", WSAGetLastError());
            WSACloseEvent(hWSAEvent);
            hWSAEvent = NULL;
        }
        else
        {
            printf("UDP: Async socket ops ready.\r\n");
        }
    }
```

```cpp
}

int UDP::Send(char* data, unsigned int length)
{
    int numsnt = sendto(Socket, data, length, 0, (struct sockaddr
 *)&destSockAddr, slen);
   if ( numsnt == SOCKET_ERROR)
   {
      int WSErrorCode = WSAGetLastError();
      std::cout << "WSErrorCode = " << WSErrorCode<< std::endl;
      DisplayError("UDP:: sendto error");
      return -1;
   }
   return numsnt;
}

int UDP::Recv(char* data, unsigned int length)
{
   int numrec = recvfrom(Socket, data, length, 0, (struct
 sockaddr*)&destSockAddr, &slen);
   if (numrec == SOCKET_ERROR)
   {
      int WSErrorCode = WSAGetLastError();
      std::cout << "WSErrorCode = " << WSErrorCode<< std::endl;
      DisplayError("UDP:: recvfrom error");
      return -1;
   }
   return numrec;
}

int UDP::RecvNonblocking(char* data, unsigned int length, unsigned
 int timeout)
{
   int numrec= 0;
   int flag = 0;
   DWORD waitRes = 0;
   DWORD lastErr = 0;

    if (NULL != hWSAEvent)
    {
        waitRes = WaitForSingleObject(hWSAEvent, timeout);
        if (WAIT_TIMEOUT == waitRes)
        {
                printf("UDP RecvNonblocking: Wait for socket read timed
 out.\r\n");
                numrec = SOCKET_ERROR;
            return numrec;
         }

      else if (WAIT_FAILED == waitRes)
         {
```

```cpp
            printf("UDP RecvNonblocking: Wait for socket read event
failed. Err = %d\r\n", GetLastError());
            numrec = SOCKET_ERROR;
          return numrec;
        }
        else
        {
            // __fallthrough to recv below.
        }
    }

    numrec = recvfrom(Socket, data, length, 0, (struct
sockaddr*)&destSockAddr, &slen);
    lastErr = WSAGetLastError();
    if ((numrec == SOCKET_ERROR) && (WSAEWOULDBLOCK == lastErr))
    {
        //printf("recv returned would block. skipping\r\n");
        //printf("numerc = %d \n", numrec);
        return 0;  //SOCKET ERROR =-1, if returned would stop receiving
thread. so return something else
    }

    if (numrec == 0)
    {
        printf("UDP RecvNonblocking: Connection closed by peer.\n");
        return -1;
    }

    if (numrec == SOCKET_ERROR)
    {
    printf("UDP RecvNonblocking: socket error %d.\n", lastErr);
    return -1;
    }

    return numrec;
}
```

The following code is an example skeleton for using the UDP class to send data to a machine with IP address *HD2IP* from the WinCE machine in a continuous loop.

```cpp
char* HD2IP = "192.168.0.1";
char* CEIP = "192.168.0.2";
unsigned short TeleOpPortSend = 18000; //specify which port to use
UDP* p_udpCESend = new UDP(TeleOpPortSend, HD2IP, CEIP); //create UDP
    instance
struct SendData //data to send to HD2
{
   double data1;
    double data2;
    //etc etc
};

int wmain(int argc, wchar_t** argv){

    if (p_udpCESend->Initialize()==-1){  //initialize p_udpCESend
        cout << "Could not create and bind send socket" << std::endl;

            //error handling code
            return 0;
    }

  // other initalizations

   while( !(GetAsyncKeyState(VK_ESCAPE)&0x8000 ) ) // while 'Esc' is
  not pressed
   {

       // fill sendData struct with the data to be transmitted

       udpStatus = p_udpCESend->Send((char*)&sendData,
  sizeof(sendData));
       if (udpStatus == -1)
     {
        cout << "Error in UDP sending!" << endl;
         //error handling code here
        break;
     }
       SleepTillTick(); // loop roughly every millisecond. A more
  accurate timing method is used in actual experiments.
    }
   delete p_udpCESend;
}
```

Appendix D

Arm Impedance Identification – Participation Information Letter and Consent Form

This Appendix presents the Participation Information Letter and Consent Form for any experiment in this thesis research involving the human arm impedance identification with the Quanser rehabilitation robot.

UNIVERSITY OF ALBERTA

DEPT OF ELECTRICAL AND COMPUTER ENGINEERING

Electrical and Computer Engineering Reseach Facility
Edmonton, Alberta, Canada T6G 2V4
Tel: 780.492.3332
Fax: 780.492.1811
www.ece.ualberta.ca

INFORMATION LETTER and CONSENT FORM

Study Title: Measuring the mechanical impedance of the upper limb using a rehabilitation robot

Research Investigator:

Dr. Mahdi Tavakoli
Assistant Professor
Department of Electrical and Computer Engineering
Electrical and Computer Engineering Research Facility
University of Alberta
Edmonton, AB, T6G 2V4

E: mahdi.tavakoli@ualberta.ca
T: 780.492.8935

Background

You have been invited to participate in a research study that aims to develop techniques to accurately measure the mechanical impedance (e.g., "stiffness") of the human arm and wrist using data collected by two rehabilitation robots (one for testing the arm and one for testing the wrist). The results of this study will be shared at scientific conferences and published in scientific journals and theses of post-secondary students who are assisting the PI on this study. Should you choose to participate in this study, your total time commitment will be under two hours.

This research is a component of a rehabilitation robotics research program in the Telerobotic and Biorobotic Systems Group within the University of Alberta's Department Electrical and Computer Engineering. This research program is a collaboration with Edmonton's Glenrose Rehabilitation Hospital and Quanser, Inc. The work is funded by the National Sciences and Engineering Research Council of Canada and Alberta Innovates – Technology Futures, with in-kind contributions from the Glenrose Rehabilitation Hospital and Quanser, Inc.

Purpose

Individuals who have suffered stroke, spinal cord injury, or other health complications that impair movement often have irregular arm/wrist impedance compared to healthy individuals. Current techniques to measure hand/arm impedance rely on a human expert observing a patient's motions and scoring the impedance on an established ranking system. Since these assessments are based on subjective observation, their accuracy and consistency can vary across clinicians. This creates a need for development of sensitive methods for consistent, objective evaluation of impedance to track a patient's recovery and guide the rehabilitation process.

Measuring the mechanical impedance of the upper limb using a rehabilitation robot

This study focuses on developing techniques to measure the arm and wrist impedance of healthy individuals using data collected by two robots (one for arm assessment and one for wrist assessment). We intend to develop measurement techniques that will supplement traditional clinical assessments of human arm/wrist stiffness with highly sensitive, reproducible, and accurate quantitative measures. The techniques we develop will eventually be evaluated on individuals with motor impairment in a future project beyond the scope of this study.

<u>*Eligibility*</u>

To participate in this study, you must not have been diagnosed with neurological or musculoskeletal ailments that could cause your arm and/or wrist to have different biomechanical properties than those of healthy individuals.

<u>*Study Procedures*</u>

Part One: Background data collection (estimated time: 5 minutes)

All data collection will be completed in the Advanced Controls Laboratory (ECERF W4-050, University of Alberta).

When you arrive at the laboratory, you will be given an opportunity to review this document and ask us questions about the study. If you decide to participate, we will proceed to collect the following background data: your height, weight, dominant hand, gender, and age. This information will be used to check whether the arm/wrist impedance measurements we obtain for our participants show any trends with respect to these factors. We will also measure the length of your right and left forearm, upper arm, and your hand which is used in the calculation of your arm and wrist stiffness. For this reason, **please wear short sleeves when you come to the laboratory.**

Part Two: Arm and wrist impedance measurements (estimated time: 90 minutes)

To measure your upper-limb impedance, two separate phases are considered. The first one is to measure your arm impedance and the second one is to measure your wrist impedance.

For the <u>first phase</u>, you will be seated in front of an upper-limb rehabilitation robot shown in (Fig. 1). Your arm may be secured to the forearm support with nylon safety straps, and a fabric sling suspended from the ceiling will support the weight of your arm against gravity.
In each measurement trial, the robot will gently jiggle your arm (which can be your left arm or your right arm) by applying a series of small position perturbations (no larger than 3 cm) or force perturbations (no larger than 8 N) to your hand. Trials will be performed with your hand positioned at different locations.

For the <u>second phase</u>, you will be seated in front of a table-top haptic device (shown in Fig. 2) to examine your wrist by providing small rotational movements and forces. The robot jiggles your wrist (which can be your left wrist or your right wrist) by applying a series of small angular position perturbations (no larger than 40 degree) to your wrist.

Measuring the mechanical impedance of the upper limb using a rehabilitation robot

In total, including both first and second phases, approximately 45 trials will be completed, each lasting from one to two minutes.

Note that slight modifications may be made to the experimental procedure based on what we learn as we analyze the data from our first few participants. For instance, we may ask you to relax your arm/wrist in some trials and hold it stiff in others. Sometimes we may ask you keep your arm in one position while the robot jiggles it, and other times we may ask you to move your hand along a path.

In addition to the force (including hand force and grasp force) and motion data collected by the robot, we will record videos of the robot jiggling your arm using a camera mounted to the ceiling. (This video will not contain any direct facial images and no sound will be recorded.)

Figure 1: Experiment setup for arm impedance measurement

Figure 2: Experiment setup for wrist impedance measurement

Measuring the mechanical impedance of the upper limb using a rehabilitation robot

<u>Benefits</u>

Beyond the opportunity to have hands-on experience with a brand new robotic technology, there are no direct benefits available to you for participating in this study. However, we hope that this study will help the scientific community to better understand how to accurately measure the impedance of the human arm/wrist, enabling clinicians to more effectively track patients' motor recovery and design therapy programs that will help maximize motor recovery.

There are no financial costs or benefits involved in participating in this research.

<u>Risk</u>

We have taken every measure possible to ensure your safety and minimize any risks involved in participating in this study. However, you should be aware of the following potential risk factors:

- You may find your arm/wrist becomes tired. If this should occur, please let us know so that we can pause the data collection so that you may rest and relax your arm/wrist.
- There is always a small chance that the computer used to program the robot could crash during the experiment. This would *not* cause the robot to move in an unsafe manner.
- If appropriate safeguards had not been put in place, the robots would be capable of producing sudden motions or exerting large forces which could potentially injure your arm/wrist. However, we have taken multiple precautions to minimize the chance of this occurring:
    1. The robots' control software was programmed to ensure it interacts with humans in a gentle manner. For instance, we have implemented processes to prevent quick movements and have included safety checks to immediately turn off the robots' motors if sudden unexpected motion is detected.
    2. We have electrically restricted the robots' motors so that the robots cannot apply forces higher than 20 N to your arm, which is about the force your arm feels when you pick up a full 2 L carton of milk. Also the robots cannot apply moments (angular forces) higher than 2 N.m to your wrist which is about the force your wrist feels when you hold a full 2L carton of milk in your hand when your hand is parallel to the ground.
    3. The robots are positioned so that your torso is outside of the area they can reach. The robots are also clamped to the table top to ensure they do not move out of their positions.
    4. Finally, you will be given an emergency stop button to hold in your free hand. Should you feel any discomfort while interacting with the device, a push of this button will instantly turn off the robot.

<u>Voluntary Participation</u>

Your participation in this study is completely voluntary—you are under no obligation to participate. Should you wish to opt out of the study at any point without penalty, you may do so by verbally informing us. We will not collect any additional data from you if you choose to withdraw after participating in the study. However, we may continue to use any data that we have already collected.

<u>Confidentiality & Anonymity</u>

After we analyze the data collected in this study, the results will be published in scientific journals, shared at scientific conferences, and theses of graduate students assisting the principal investigator in this study.

These results will be presented in an anonymous manner so that you will not be personally identifiable. If you agree to participate in this study, we will assign you a participant number. All data that is collected—and any results we publish—will be labeled by participant number without reference to your name.

The digital data collected in this study (i.e., force and position measurements and video data) will be stored on password-protected computers in our laboratory. Hard-copy data (i.e., handwritten tables with your height, weight, age, etc.) will be stored in a locked filing cabinet in our laboratory. Only the Research Investigator (Dr. Mahdi Tavakoli) and the Research Ethics Committee will have access to this raw data. We do not plan to destroy the data collected in this study as we may use it future research projects.

If you would like to receive a copy of the published research papers produced from this study, please mention your interest to us.

Further Information

If you have any further questions regarding this study, please do not hesitate to contact Dr. Mahdi Tavakoli.

The plan for this study has been reviewed for its adherence to ethical guidelines by a Research Ethics Board at the University of Alberta. If you have concerns about this study or questions regarding participant rights and ethical conduct of research, please contact the Research Ethics Office at 780-492-2615. This office has no direct involvement with this project.

Consent Statement

I have read this form and the research study has been explained to me. I have been given the opportunity to ask questions and my questions have been answered. If I have additional questions, I have been told whom to contact. I agree to participate in the research study described above. I will receive a copy of this consent form after I sign it.

_____   _____

Participant's Name (printed) and Signature   Date

_____   _____

Name (printed) and Signature of Person Obtaining Consent   Date

Appendix E

Interaction with Yaskawa Motoman SIA5F Robot – Risk Assessment

In the experiments performed in Chapter 3 and Chapter 4, one human operator (the supervisory investigator) interacted with the Yaskawa Motoman SIA5F robot via a tool (a screwdriver in Chapter 3 and the hole tool in Chapter 4). For this human-robot interaction, we have taken measures to minimize the following identified risks to ensure the safety of the human operator:

- The human operator might get tired from performing tasks with the robot. If this should happen, the operator can pause the experiment and relax at any time.

- There is a very slight chance that the human operator may be electrocuted due to the high voltage (3 phase, 110V AC) operating on the robot controller. We have performed proper grounding of the robot controller and it has passed ETL safety inspection by Intetek.

- There is a small chance that the software managing robot control and networking might crash. This will not cause the robot to move in any unsafe manner.

- In the case that the robot goes into instability, it is possible that the robot will hit the human operator and cause injury. To mitigate this risk, we have taken the following precautions:

  1. The software that is used for controlling the robot (purchased from Yaskawa Innovation, Inc.) has built-in safety mechanisms that monitor the robot velocity and acceleration, so that the robot will be stopped immediately when sudden movements occur. For our experiments, actuated robot axis velocity limit is set to be 20 °/s for the sixth robot joint and 13 °/s for the second robot joint. The acceleration limit is set to be 375 $°/s^2$ for the sixth robot joint and 255 $°/s^2$ for the second robot joint.

  2. The robot is fixed to a heavy wooden table appropriately with bolts and nuts so it will not move out of position.

  3. The human operator also has an emergency stop button held in one hand at all times, so that he can stop the robot at any moment that he judges unsafe.

Appendix F

Mechanical Drawings for Hardware Interfaces

In this Appendix we provide the drawings of some of the custom built mechanical parts used for the experiments in this thesis.

The Motoman SIA5F end effector and ATI Gamma Net force sensor interface (as shown in Fig. 4.2(b) is comprised of two parts. Part 1 (shown in Fig. F.1) is first mounted onto the Motoman SIA5F end effector, then part 2 (shown in Fig. F.2) is mounted onto part 1. Finally the ATI Gamma force sensor can be mounted onto part 2.

The peg used for the peg-in-the-hole insertion task in Chapter 4 is shown in Fig. F.3. It is also used for holding the wooden plate in the screwdriving task in Chapter 3 as shown in Fig. 3.2(b). It is connected to the force sensor via the interface shown in Fig. F.4.

The hole used for the peg-in-the-hole insertion task in Chapter 4 is shown in Fig. F.5. It can be mounted onto the end effector of a Motoman SIA5F robot via the interface shown in Fig. F.6.
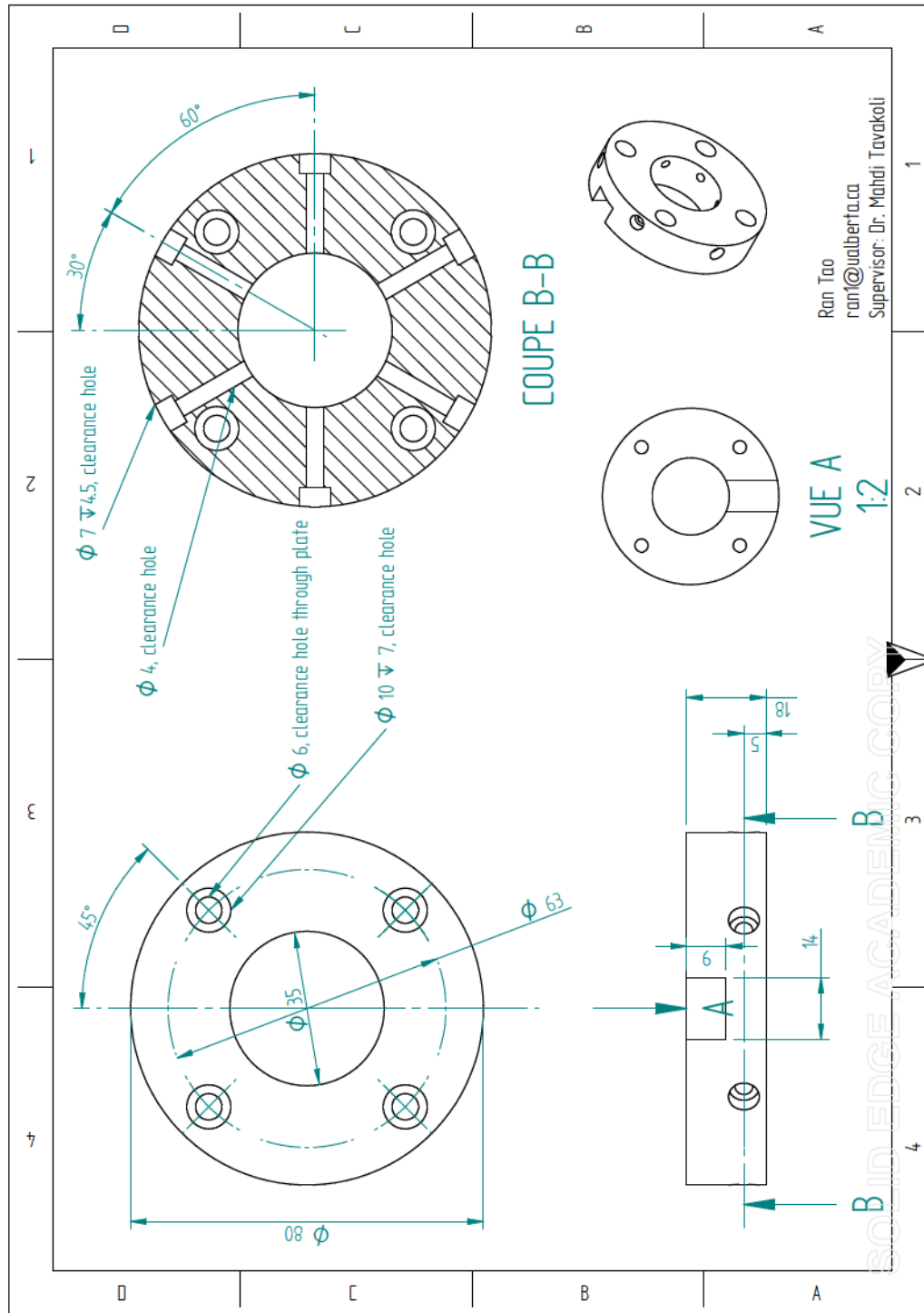
FIGURE F.1: SIA5F end effector and ATI Gamma NET force sensor interface part 1
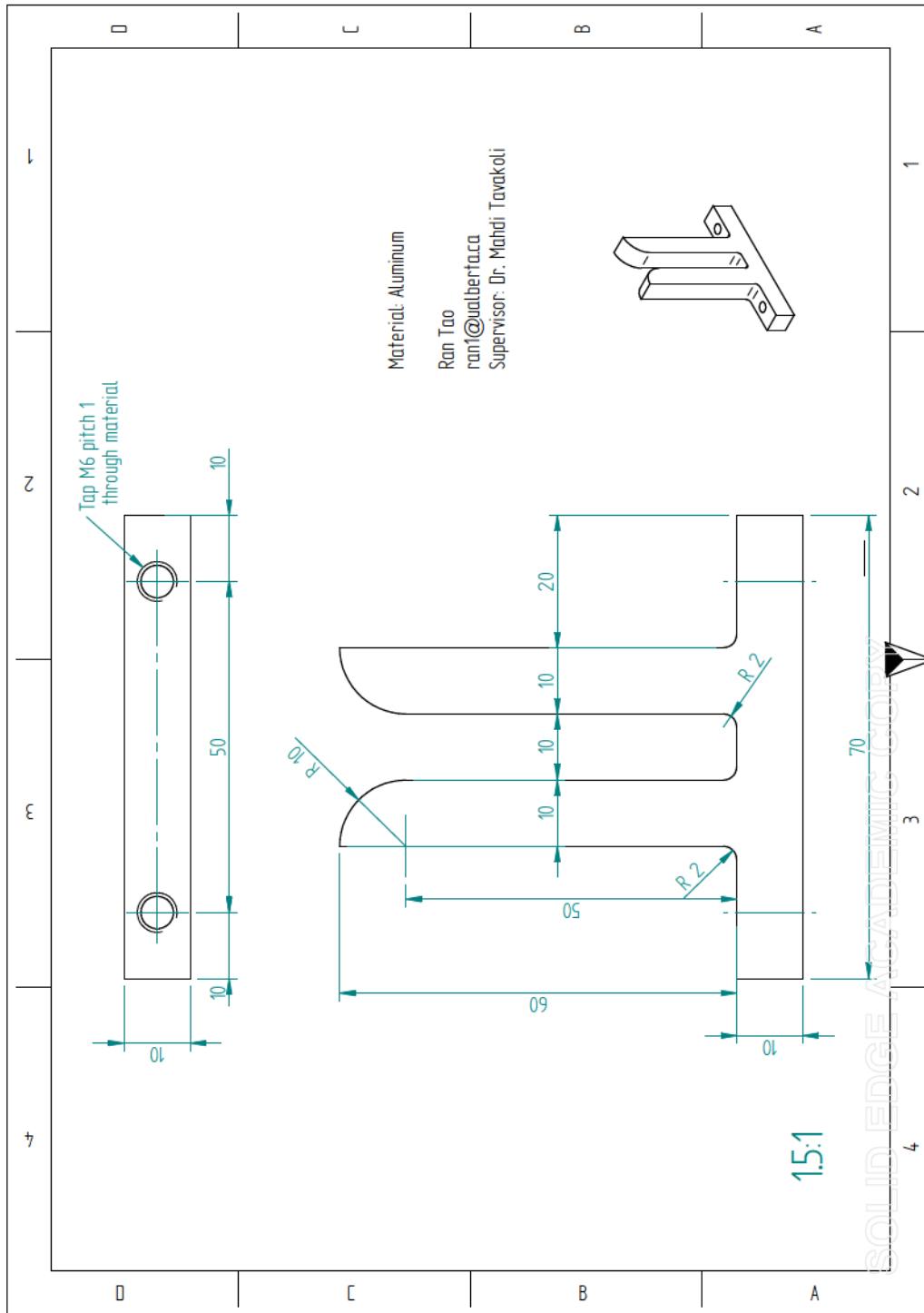
FIGURE F.2: SIA5F end effector and ATI Gamma NET force sensor interface part 2

FIGURE F.3: Peg tool

FIGURE F.4: ATI Gamma Net force sensor and peg tool interface

Material: Aluminum

Ran Tao
ran1@ualberta.ca
Supervisor: Dr. Mahdi Tavakoli

Tap M6 pitch 1
through material

FIGURE F.5: Hole tool

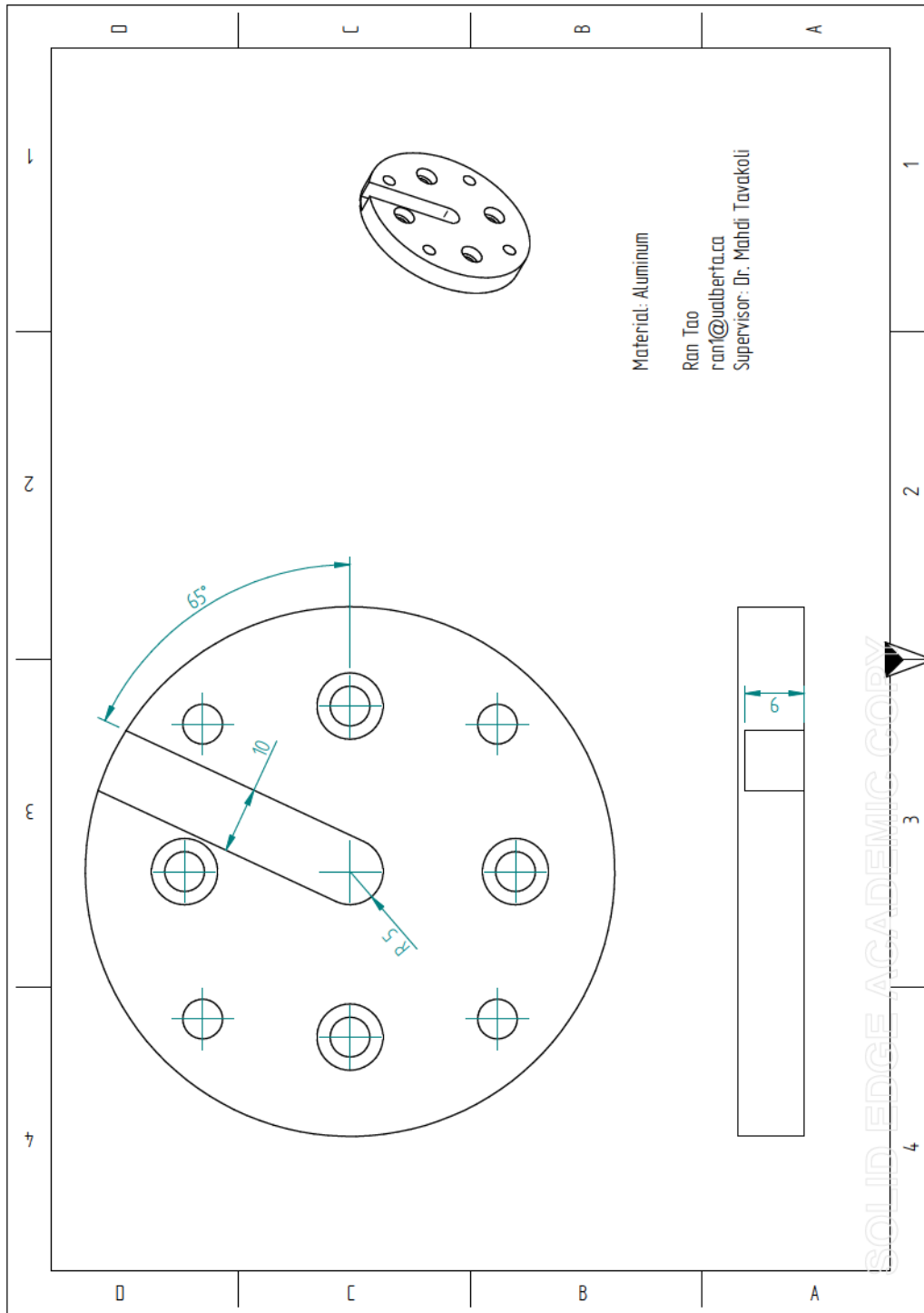Material: Aluminum

Ran Tao
ran1@ualberta.ca
Supervisor: Dr. Mahdi Tavakoli

FIGURE F.6: SIA5F end effector and hole tool interface part 1